

# PE&RS

July 2019

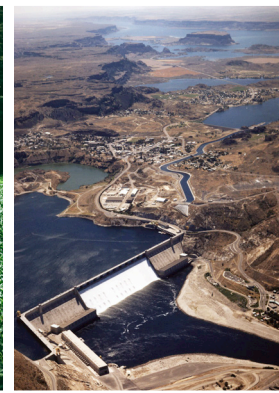
Volume 85 Number 1

PHOTOGRAMMETRIC ENGINEERING & REMOTE SENSING The official journal of the International Society of Photogrammetry and Remote Sensing



# PECORA 21 • ISRSE 38

## *Continuous Monitoring of Our Changing Planet: From Sensors to Decisions*



## *Save the Date*

**October 6-11, 2019**

Baltimore, MD • Marriott Waterfront

<https://www.asprs.org/event/pecora21-isrse38>





joint meeting of the 21st William T. Pecora Memorial Remote Sensing Symposium (Pecora 21) and the 38th International Symposium on Remote Sensing of Environment (ISRSE-38) will convene in

Baltimore, Maryland, USA from October 6 – 11, 2019. The combined conference will be hosted by NASA, NOAA and the USGS, with an overarching theme of “*Continuous Monitoring of Our Changing Planet from Sensors to Decisions*.”

## Plenary Presentations from

### Gilberto Câmara

Dr. Gilberto Câmara is a Brazilian researcher in Geoinformatics, Spatial Analysis, Land Use Change, and Nature-Society Interactions, from Brazil's National Institute for Space Research (INPE). Dr. Câmara is currently Secretariat Director for the Group on Earth Observations (GEO).

### Michael Freilich

Dr. Michael Freilich is an accomplished oceanographer, microwave remote sensing expert, educator, and science administrator who directed NASA's Earth Science Division from November 2016 through February 2019.

---

## Conference Location

### Marriot Waterfront Baltimore

Please make your hotel reservations at the Baltimore Marriott Waterfront Hotel, as soon as possible in order to take advantage of the special ASPRS room rates. While our room block does not expire until September 10, 2019, there is no guarantee that rooms will be available at that late date in the block or in the hotel. Attendees can book their reservations by calling 1-877-212-5752. A very limited number of rooms are reserved in the room block at this special rate.

## Exhibiting

Maximize the benefits of your participation by becoming a symposium sponsor. Your company can make its mark and gain visibility before, during and after the event. Choose from our list of Unique Sponsorships for the events or items that best showcase your company.

Contact Bill Spilman, Innovative Media Solutions, to discuss your companies exhibiting needs.

(877) 878-3260 toll-free • (309) 483-6467  
bill@innovativemediasolutions.com

## Special Presentation Sessions

- The Challenges of Integration for Arctic Monitoring
- Using Remotely Sensed Data to Map Forest Structure and Attributes
- Space Agencies Outlook
- Communicating Science Across the Earth Observation Life Cycle
- National Land Cover Database 2016, Offering New Change Insights Across the Conterminous United States
- Copernicus—Europe's eyes on Earth: Sustainable and Continuous Monitoring of our Environment
- Global Hyperspectral Imaging Spectral-library of Agricultural-Crops (GHISA) in Support of NASA's Surface Biology and Geology (SBG) mission
- Climate Science – Challenges and Opportunities for Fulfilling Global Multilateral Agreements
- Mapping and Monitoring Surface Change: Landslides and Subsistence
- Copernicus Serving Sustainable Development Goals
- Biodiversity and Conservation Case Studies
- Large Area Land Change Mapping and Monitoring Investigations
- Sustainable Land Imaging and the Future of Moderate-Resolution Land Observation
- Women in Remote Sensing
- Earth Observation and Remote Sensing Education Initiatives
- Toward the Assessment and Modeling of a Functional Relationship of Land Cover and Land Use A Possible New Path forward – the LCHML (Land Characterization Metal-Language) A New Proposed ISO Standard
- Open Data Cube: A New Data Technology for Enhancing the Use of Satellite Data to Address Sustainable Development Goals
- Bathymetry and Near-Shore Investigations
- How No-cost Landsat Data is Reshaping College Level Remote Sensing Courses (AmericaView Special Session)-Land Change Monitoring Assessment and Projection (LCMAP): New Land Change Science Research and Development
- New Generation of NOAA Operational Satellites to support Land, Arctic, and Coastal Waters Applications
- Advances in Soil Moisture and Condition Measurement and Monitoring
- A Conversation on the Landsat Program and its Data Policy
- Investigations in Support of Human Welfare
- Satellite Interoperability
- NASA Harvest and Other Recent Advances in Remote Sensing of Agricultural Applications and Food Security
- Collaboration in the Diverse Geospatial Workforce: How Early Career Professionals Can Bring Innovations to the Technical Community
- Case Studies in Flood Monitoring and Management
- UAS: Changing the Future of Remote Sensing
- Earth Observation and Agricultural Statistics – Agricultural and Agri-environmental Monitoring for SDG 2: Zero Hunger
- Processing Strategies for Big Data
- Remote Sensing Investigations of Wetlands and Near-Shore Issues
- New Technology and Techniques to Increase Scientific and Applications Access to Satellite Earth Observations
- Applications of Earth Observations for Disaster Assessments and Management
- Plus many more!

To have your press release published in *PE&RS*, contact Rae Kelley, [rkelly@asprs.org](mailto:rkelly@asprs.org).

## PRODUCTS

**Teledyne Technologies Incorporated** announced today that imaging hardware and software from Teledyne Optech helped enable 3D spatial data acquisition and visual effects for HBO's hit series *Game of Thrones*. A team, led by Vektra d.o.o. of Croatia, utilized Teledyne's lidar (light detection and ranging) technology to create a detailed 3D representation of the old city of Dubrovnik, the model for the fictional city of King's Landing. A promotional video can be found at the following link: <https://www.youtube.com/watch?v=PTRqjOR4awU>.

Lidar is becoming increasingly popular for creating realistic computer-generated imagery (CGI) and visual special effects. Traditionally, lidar has been used for mapping and in construction, civil engineering, mining and transportation. Lidar is now of particular interest in the film industry because of its ability to scan buildings or even entire cities in 3D, while maintaining a high level of detail and accuracy. Lidar's ability to generate exact replicas of locations reduces the time and cost for 3D modelling and helps create more realistic visual effects.

Vektra generated 3D point clouds in Dubrovnik using various lidar technologies including Teledyne Optech's Maverick mobile lidar system and Polaris fixed terrestrial scanner. The lidar point clouds were then colorized with digital camera imagery and image fusion software.

"We are most proud when our technology contributes to new scientific knowledge, such as revealing an extensive, undiscovered Maya civilization in Guatemala," said Robert Mehrabian, Executive Chairman of Teledyne. "We are equally delighted when our high-technology equipment supports art and entertainment."

Soil analysis using a full range UV/VIS/NIR **Spectral Evolution** spectroradiometer with a 350-2500nm spectral range is fast, non-destructive, affordable, and doesn't involve hazardous chemicals. With our handheld sample contact probe, soil spectra can be collected in the field from outcrops or a soil pit. Analysis with EZ-ID sample identification software running on a tablet or

laptop matches high resolution target scans against three known sample libraries – the USGS library and the optional SpecMIN and GeoSPEC libraries. A researcher is able to see the absorption features characteristic of clays.

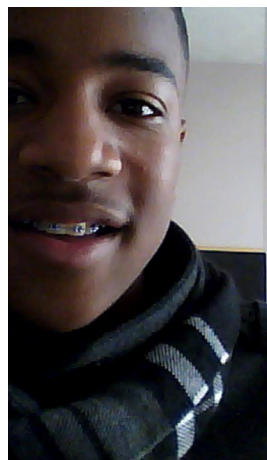
EZ-ID provides a best match based on examining the target spectra and the library spectras. A researcher can add or remove regions of interest to focus on only the prominent features in the spectra for a better identification in clay mixtures.

For more information, visit: <https://spectralevolution.com/products/hardware/field-portable-spectroradiometers-for-remote-sensing/>.

## CALENDAR

- 11-15 August, **SPIE—Imaging Spectrometry XXIII**, San Diego, California. For more information, visit [spie.org/OP423](http://spie.org/OP423).
- 17-18 September, **GIS IN THE ROCKIES**, Denver, Colorado. For more information, visit <http://gisintherockies.org>.
- 28 September – 2 October, **GIS-PRO 2019**, New Orleans, Louisiana. For more information, visit [www.urisa.org/gispro2019](http://www.urisa.org/gispro2019).
- 6-11 October, **Pecora 21/ISRSE 38**, Baltimore, Maryland. For more information, visit <http://www.asprs.org/event/pecora21-isrse38>.

<b>ASPRS Contacts</b>	425 Barlow Place, Suite 210, Bethesda, MD 20814 301-493-0290, 225-408-4422 (fax), <a href="http://www.asprs.org">www.asprs.org</a>
	<b>Membership/PE&amp;RS Subscription/Conferences</b> Priscilla Weeks — <a href="mailto:pweeks@asprs.org">pweeks@asprs.org</a>
	<b>Advertising/Exhibit Sales</b> Bill Spilman — <a href="mailto:bill@innovativemediasolutions.com">bill@innovativemediasolutions.com</a>
	<b>Calendar</b> <a href="mailto:calendar@asprs.org">calendar@asprs.org</a>



**Too young to drive the car? Perhaps!  
But not too young to be curious about geospatial sciences.**

The ASPRS Foundation was established to advance the understanding and use of spatial data for the betterment of humankind. The Foundation provides grants, scholarships, loans and other forms of aid to individuals or organizations pursuing knowledge of imaging and geospatial information science and technology, and their applications across the scientific, governmental, and commercial sectors.

**Support the Foundation, because when he is ready so will we.**

[asprsfoundation.org/donate](http://asprsfoundation.org/donate)



## FEATURES

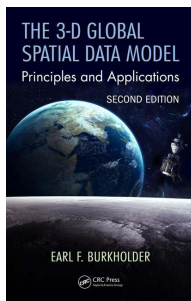


**ASPRS MEMBER PERKS!**

**25% OFF**  
ON ALL  
CRC PRESS BOOKS\*

\*Valid for online orders only and excludes eBooks.

**479** ASPRS Partners with CRC Press – Taylor and Francis



**473** Book Review—*The 3-D Global Spatial Data Model: Principles and Applications, 2<sup>nd</sup> Edition*

### COLUMNS

- 469** Mapping Matters
- 472** Signatures  
The Column of the Student Advisory Council.
- 475** Grids and Datums  
This month we look at the Democratic and Popular Republic of Algeria.

### ANNOUNCEMENTS

- 465** Pecora 21/ISRSE 38 Symposium
- 474** ASPRS Certification
- 479** Headquarters News
- 479** New ASPRS Members  
Join us in welcoming our newest members to ASPRS.

### DEPARTMENTS

- 466** Industry News
- 466** Calendar
- 471** Ad Index
- 492** ASPRS Sustaining Members

## PEER-REVIEWED ARTICLES

### **481 High-resolution Large-area Digital Orthophoto Map Generation using LROC NAC Images**

*Kaichang Di, Mengna Jia, Xin Xin, Jia Wang, Bin Liu, Jian Li, Jianfeng Xie, Zhaoqin Liu, Man Peng, Zongyu Yue, Jia Liu, Ruilin Chen, and Changlu Zhang*

This study introduces a systematic method for large-area seamless digital orthophoto map production. The result generated using over 700 Lunar Reconnaissance Orbiter Camera (LROC) Narrow Angle Camera (NAC) images has a resolution of 1.5 m and covers a large area of 20° in longitude and 4° in latitude.

### **493 Occlusion Probability in Operational Forest Inventory Field Sampling with ForeStereo**

*Fernando Montes, Álvaro Rubio-Cuadrado, Mariola Sánchez-González, Isabel Aulló-Maestro, Miguel Cabrera, and Cristina Gómez*

Proximal sensing technologies under fixed-point sampling inhibits detection of some trees. This study evaluates various approaches to eliminate problems in fixed point sampling due to tree occlusions and instrument bias estimates.

### **509 A Novel Method for Separating Woody and Herbaceous Time Series**

*Qiang Zhou, Shuguang Liu, and Michael Hill*

In this study, the authors developed a frequency decomposition method to separate woody and herbaceous vegetation components using time series for modeling inter-relationships between trees and grasses, and monitoring fuel loads and biomass for livestock. They examined the spatial and temporal patterns of the decomposed NDVI, where woody and herbaceous NDVI showed different responses to precipitation.

### **521 Examining the Effectiveness of Spectrally Transformed SMA In Urban Environments**

*Yingbin Deng and Changshan Wu*

While spectral transformation has been used to compute spectral variability, there is no study that addresses the necessity and applicability of transformed models. This paper answers two questions: 1) whether significantly different results will be generated through applying a spectral transformation, and 2) which spectral transformation performs better in urban environments.

**See the Cover Description on Page 468**



A witch's cauldron. Gastrointestinal reflux. A kale smoothie. The green swirls of this satellite image may conjure up many mental pictures—except what it actually is. On April 12, 2019, the Operational Land Imager on Landsat 8 acquired this image of Lake Khanka.

This shallow freshwater lake is located on the border of Russia and northeastern China. The green hues in the water are most likely chlorophyll-rich phytoplankton in the lake, which contains a fairly constant presence of diatoms. The phytoplankton and other suspended solids in the lake are easily mixed by wind. This mixing of material between the surface and bottom often clouds the water, which usually starts to lose clarity in less than a meter.

The microscopic particles and organisms can be seen in great detail due to a special editing technique that combines scientific expertise and an artistic touch. Like a photographer adjusting lighting and using filters, Norman Kuring of NASA's Ocean Biology group works with various software programs and color-filtering techniques to draw out the fine details in the water. The swirls in the water are all quite real; Kuring simply separates and enhances certain shades and tones in the data to make the biomass more visible. Without Kuring's processing of the subtle colors in the image, Lake Khanka can appear less compelling.

As one of the largest freshwater lakes (by area) in Far Eastern Russia and China, Lake Khanka (known as Lake Xingkai in Chinese) plays an important role in supporting biodiversity. It is a major source of freshwater for birds (particularly waterfowl) and home to some of the highest levels of bird diversity in Eurasia. Khanka is also home to many freshwater species of fish and aquatic animals, including a large population of rare Chinese soft-shelled turtles.

The lake is surrounded by open lowlands, wetlands, grassy meadows, and swamps, which also contain many rare and endangered plants. The lake has been designated as a Ramsar Convention Wetland Site, promoting conservation and sustainable use of the wetlands. The lake is also included on UNESCO's "World Biosphere Reserves" list.

For more information, visit <https://landsat.visibleearth.nasa.gov/view.php?id=145073>.

Image by Norman Kuring, NASA's Ocean Color web, and Lauren Dauphin. Story by Kasha Patel.



### JOURNAL STAFF

Publisher ASPRS

Editor-In-Chief Alper Yilmaz

Assistant Editor Jie Shan

Assistant Director — Publications Rae Kelley

Electronic Publications Manager/Graphic Artist Matthew Austin

*Photogrammetric Engineering & Remote Sensing* is the official journal of the American Society for Photogrammetry and Remote Sensing. It is devoted to the exchange of ideas and information about the applications of photogrammetry, remote sensing, and geographic information systems. The technical activities of the Society are conducted through the following Technical Divisions: Geographic Information Systems, Photogrammetric Applications, Lidar, Primary Data Acquisition, Professional Practice, and Remote Sensing Applications. Additional information on the functioning of the Technical Divisions and the Society can be found in the Yearbook issue of *PE&RS*.

Correspondence relating to all business and editorial matters pertaining to this and other Society publications should be directed to the American Society for Photogrammetry and Remote Sensing, 425 Barlow Place, Suite 210, Bethesda, Maryland 20814-2144, including inquiries, memberships, subscriptions, changes in address, manuscripts for publication, advertising, back issues, and publications. The telephone number of the Society Headquarters is 301-493-0290; the fax number is 225-408-4422; web address is [www.asprs.org](http://www.asprs.org).

**PE&RS.** *PE&RS* (ISSN0099-1112) is published monthly by the American Society for Photogrammetry and Remote Sensing, 425 Barlow Place, Suite 210, Bethesda, Maryland 20814-2144. Periodicals postage paid at Bethesda, Maryland and at additional mailing offices.

**SUBSCRIPTION.** For the 2019 subscription year, ASPRS is offering two options to our *PE&RS* subscribers — an e-Subscription and the print edition. E-subscribers can plus-up their subscriptions with printed copies for a small additional charge. Print and Electronic subscriptions are on a calendar-year basis that runs from January through December. We recommend that customers who choose both e-Subscription and print (e-Subscription + Print) renew on a calendar-year basis. The new electronic subscription includes access to ten years of digital back issues of *PE&RS* for online subscribers through the same portal at no additional charge. Please see the Frequently Asked Questions about our journal subscriptions.

The rate of the e-Subscription (digital) Site License Only for USA and Foreign: 1000.00 USD; e-Subscription (digital) Site License Only for Canada\*: 1049.00 USD; Special Offers: e-Subscription (digital) Plus Print for the USA: 1365.00 USD; e-Subscription (digital) Plus Print Canada\*: 1424.00 USD; e-Subscription (digital) Plus Print Outside of the USA: 1395.00 USD; Printed-Subscription Only for USA: 1065.00 USD; Printed-Subscription Only for Canada\*: 1124.00 USD; Printed-Subscription Only for Other Foreign: 1195.00 USD. \*Note: e-Subscription/Printed-Subscription Only/e-Subscription Plus Print for Canada include 5% of the total amount for Canada's Goods and Services Tax (GST #135123065). **PLEASE NOTE: All Subscription Agencies receive a 20.00 USD discount.**

**POSTMASTER.** Send address changes to *PE&RS*, ASPRS Headquarters, 425 Barlow Place, Suite 210, Bethesda, Maryland 20814-2144. CDN CPM #40020812

**MEMBERSHIP.** Membership is open to any person actively engaged in the practice of photogrammetry, photointerpretation, remote sensing and geographic information systems; or who by means of education or profession is interested in the application or development of these arts and sciences. Membership is for one year, with renewal based on the anniversary date of the month joined. Membership Dues include a 12-month electronic subscription to *PE&RS*. Or you can receive the print copy of *PE&RS* Journal which is available to all member types for an additional fee of 60.00 USD for shipping USA, \$65 USD for Canada, or 75.00 USD for international shipping. Dues for ASPRS Members outside of the U.S. will now be the same as for members residing in the U.S. Annual dues for Regular members (Active Member) is 150 USD; for Student members 50 USD for USA and Canada 58 USD; 60 USD for Other Foreign members. A tax of 5% for Canada's Goods and Service Tax (GST #135123065) is applied to all members residing in Canada.

**COPYRIGHT 2019.** Copyright by the American Society for Photogrammetry and Remote Sensing. Reproduction of this issue or any part thereof (except short quotations for use in preparing technical and scientific papers) may be made only after obtaining the specific approval of the Managing Editor. The Society is not responsible for any statements made or opinions expressed in technical papers, advertisements, or other portions of this publication. Printed in the United States of America.

**PERMISSION TO PHOTOCOPY.** The appearance of the code at the bottom of the first page of an article in this journal indicates the copyright owner's consent that copies of the article may be made for personal or internal use or for the personal or internal use of specific clients. This consent is given on the condition, however, that the copier pay the stated per copy fee of 3.00 USD through the Copyright Clearance Center, Inc., 222 Rosewood Drive, Danvers, Massachusetts 01923, for copying beyond that permitted by Sections 107 or 108 of the U.S. Copyright Law. This consent does not extend to other kinds of copying, such as copying for general distribution, for advertising or promotional purposes, for creating new collective works, or for resale.



# MAPPING MATTERS

## YOUR QUESTIONS ANSWERED

*The layman's perspective on technical theory and practical applications of mapping and GIS*

BY Qassim A. Abdullah, Ph.D., PLS, CP\*\*

### QUESTION:

**Question:** I am a college student working on my bachelor's degree in Spatial Science (Surveying).

I am interested in photogrammetry, and my study is on drone-based surveys. I have the following questions on the new "ASPRS Positional Accuracy Standards for Digital Geospatial Data":

1. In sections 7.7 and 7.8, when it talks about checkpoint and ground control accuracy being 1/2 RMSEmap, is RMSEmap the desired/intended accuracy class?
2. With GCPs having three times the accuracy of the geospatial data set being tested, does that mean the GCP accuracy will be three times more accurate than the desired/intended accuracy class?
3. Do you use Table D.1 to calculate all the statistics and then use the results to determine the ASPRS accuracy class? Is that the typical workflow? Is there a sample report you can supply?
4. Are there guidelines on what you should aim for regarding the additional statistics discussed on the standards, such as max, min, skew, kurtosis and mean absolute?
5. Can you clarify what it means when you can state "tested to meet" versus "produced to meet"?
6. Can you direct me to a document regarding planning and best practice guidelines?
7. Do the vegetated area ground control points simply go on the bare ground between vegetation?
8. How do you assess seamline mismatch?
9. If an orthophoto fails a column in Table B.3 (e.g. the RMSEr is OK, but the accuracy at 95% CI exceeds the limit), do you select the accuracy class in which your project meets or exceeds all standards in a single row?
10. I note that many drone-based surveys seem to have a mean error much higher than 25% of the RMSE. What does this information tell you about the quality of the project, and how can you correct it?
11. I also noticed that nearly every drone software company reports accuracy as a function of GSD, e.g. heights within three times the GSD. How are these related, and is GSD really related to accuracy in any way? I did a project with a GSD of 1 cm, but I achieved 11 mm RMSE heights and mean of 3 mm.
12. Can you direct me to where I can read more about rigorous total propagated uncertainty regarding photogrammetry?
13. For repeat surveys of the same area, if I use the software to determine the camera calibration via self or automatic calibration, is it best to save it and then use the same calibration for the repeat flights rather than having the software re-calculate the camera calibration each time?

James Wallace  
University of Southern Queensland, Australia

**Dr. Abdullah:** In the June 2019 issue, I addressed questions 1 through 6. The remaining questions are addressed below.

### PART II

**Question 7—Do the vegetated area ground control points simply go on the bare ground between vegetation?**

**Answer:** Yes, they should. Ground control points should always be surveyed on a firm ground.

**Question 8—How do you assess seamline mismatch?**

**Answer:** Evaluating seamline mismatch is usually performed visually to determine whether features in adjacent rectified images are aligned correctly. For standard

large-format metric cameras, mosaic cut lines are inserted manually. The technician selects the mosaic cut lines path to avoid buildings, trees and other elevated objects, as well as radiometrically mismatched areas. Those mosaic cut lines are usually saved in a CAD file format such as DGN, DWG or shape file. These CAD files, if they exist, are very

Photogrammetric Engineering & Remote Sensing  
Vol. 85, No. 7, July 2019, pp. 469–471.  
0099-1112/19/469–471

© 2019 American Society for Photogrammetry  
and Remote Sensing  
doi: 10.14358/PERS.85.7.469

helpful in evaluating the seamline mismatch quality of the final product, i.e. ortho mosaic. The latest image processing software, such as Pix4D, enables users to visit the mosaic cut lines and allow them to correct or re-route the mosaic cut lines in real time. Once a mismatch is found, it can be quantified and evaluated according to the “ASPRS Positional Accuracy Standards for Digital Geospatial Data,” as illustrated in the far-right column of Table 1.

Table 1: ASPRS horizontal accuracy standards and mosaic seamline mismatch.

Horizontal Accuracy Class	RMSE <sub>x</sub> and RMSE <sub>y</sub> (cm)	RMSE <sub>r</sub> (cm)	Horizontal Accuracy at 95% Confidence Level (cm)	Orthoimagery Mosaic Seamline Mismatch (cm)
X-cm	≤X	≤1.41*X	≤2.45*X	≤2*X

**“There is never a situation in which some values of statistical terms meet the given thresholds while other terms fail to meet those thresholds for a given accuracy class.”**

**Question 9—If an orthophoto fails a column in Table B.3 (of the ASPRS Standards, see below) (e.g. the RMSE<sub>r</sub> is OK, but the accuracy at 95% CI exceeds the limit), do you select the accuracy class in which your project meets or exceeds all standards in a single row?**

Table B.3 Common Horizontal Accuracy Classes According to the New Standard.

Horizontal Accuracy Class RMSE <sub>x</sub> and RMSE <sub>y</sub> (cm)	RMSE <sub>r</sub> (cm)	Orthoimage Mosaic Seamline Maximum Mismatch (cm)	Horizontal Accuracy at the 95% Confidence Level (cm)
0.63	0.9	1.3	1.5
1.25	1.8	2.5	3.1
2.50	3.5	5.0	6.1
5.00	7.1	10.0	12.2
7.50	10.6	15.0	18.4
10.00	14.1	20.0	24.5
12.50	17.7	25.0	30.6
.....	.....	.....	.....

**Answer:** There is never a situation in which some values of statistical terms meet the given thresholds while other terms fail to meet those thresholds for a given accuracy class. The derived thresholds for RMSE<sub>r</sub> and the accuracy at 95% confidence level are all derived using the accuracy class or the RMSE x or y, therefore if the verified RMSE x or y of the product is found to be outside the specified limit, then both RMSE<sub>r</sub> and the accuracy at 95% should fail to meet the project specifications. Table 2 illustrates two situations of

product accuracy verification for a product accuracy class of 10 cm. In CASE 1, the RMSE x or y of 8 cm meets the project specifications; in CASE 2, with RMSE x or y of 13 cm, it fails to meet project specifications. As you notice from the example, once the RMSE x or y value meets the threshold, all other statistical measures derived from that RMSE meet its thresholds. In the same token, once the RMSE x or y value fails the threshold, all statistical measures fail as well.

Table 2: Horizontal Accuracy Examples.

Horizontal Accuracy Class	RMSE <sub>x</sub> and RMSE <sub>y</sub> (cm)	RMSE <sub>r</sub> (cm)	Horizontal Accuracy at 95% Confidence Level (cm)
10 cm (specification)	≤10	≤14.1	≤24.5
CASE 1 (actual)	8.0 ≤10 (pass)	11.28 ≤14.1 (pass)	19.6 ≤24.5 (pass)
CASE 2 (actual)	13.0 ≥10 (fail)	18.33 ≥14.1 (fail)	31.85 ≥24.5 (fail)

**Question 10—I note that many drone-based surveys seem to have a mean error much higher than 25% of the RMSE. What does this information tell you about the quality of the project, and how can you correct it?**

**Answer:** The ASPRS standards states that the exact specification of an acceptable value for mean error may vary by project and should be negotiated between the data provider and the client. It also recommends that the mean error be less than 25% of the specified RMSE value for the project. Mean errors that are greater than 25% of the target RMSE, should be investigated to determine the cause of the errors and to determine what actions, if any, should be taken. Higher value for the mean errors in general indicates biases in the data, especially if the computed standard deviation is low. Biases in the data can be modeled and removed. Examples of such biases in the geospatial products are generated by errors, which can be caused by using the wrong vertical or horizontal datum or if the surveyor forgot to subtract the instrument height when adjusting the network during the ground control surveying or other systematic errors. If the computed standard deviation is low, you can always subtract or add the value of the mean (or average) from the biased quantities to remove the systematic errors, and this will improve the data accuracy.

**“The technician selects the mosaic cut lines path to avoid buildings, trees and other elevated objects, as well as radiometrically mismatched areas.”**

**Question 11—***I also noticed that nearly every drone software company reports accuracy as a function of GSD, e.g. heights within three times the GSD. How are these related, and is GSD really related to accuracy in any way? I did a project with a GSD of 1 cm, but I achieved 11 mm RMSE heights and mean of 3 mm.*

**Answer:** According to the new ASPRS standards, accuracy should not be associated with imagery GSD or scale because today’s digital sensors have different configurations and lens design to enable high-resolution imagery from very high altitudes. Table 3 illustrates how these four metric digital cameras can be used to acquire imagery with the same ground resolution of 7.5 cm from drastically varied flying altitudes, from 2,363 feet to 9,937 feet above ground level (AGL). One should expect that the accuracy for products derived from imagery acquired from 9,937 feet AGL should be inferior to the accuracy of products derived from imagery acquired from 2,363 feet AGL. That is why we should not use the GSD as an indicator for product accuracy.

Table 3 Digital Cameras and Flying Altitude Examples

Camera	Focal Length (mm)	Flying Altitude (ft)	Resulting GSD (cm)
ADS80	62.77	2,363	7.5
DMC IIe 230	92.00	4,042	7.5
UltraCAM Falcon Prime	100.00	4,100	7.5
UltraCAM Eagle 210	210.00	9,937	7.5

If the software company is using the GSD as a measurement of length or dimension, then there is no harm in using the GSD to quantify products accuracy because all it means is a quantity. However, if they are using it to associate GSD as indicator or discriminator of product accuracy, then we should not condone this practice.

**“There is never a situation in which some values of statistical terms meet the given thresholds while other terms fail to meet those thresholds for a given accuracy class.”**

**Question 12—***Can you direct me to where I can read more about rigorous total propagated uncertainty regarding photogrammetry?*

**Answer:** As far as I know, there is not a book published on the topic, but you can find several good published papers on the topic, among them are the following:

- C.A. Rodarmel, M.P. Lee, K.L. Brodie, N.J. Spore and B. Bruder, “Rigorous Error Modeling for sUAS Acquired Image-Derived Point Clouds,” April 2019 IEEE Transactions on Geoscience and Remote Sensing.

**“These CAD files, if they exist, are very helpful in evaluating the seamline mismatch quality of the final product, i.e. ortho mosaic.”**

- H.J. Theiss, “Covariance Propagation from Specific to Generic Model,” Proceeding the ASPRS 2010 Annual Conference, San Diego, Calif.

**Question 13—***For repeat surveys of the same area, if I use the software to determine the camera calibration via self or automatic calibration, is it best to save it and then use the same calibration for the repeat flights rather than having the software re-calculate the camera calibration each time?*

**Answer:** It is always beneficial to use accurate camera calibration values in the bundle block adjustment because it minimizes the amount of parameter optimization. That is also how we did it when we used large-format metric cameras. However, because the cameras on board unmanned aircraft systems (UAS) are consumer-grade non-metric cameras, you will always need the help of the camera self-calibration capability of the software for every project, every time you adjust a block. Such non-metric cameras do not maintain their internal calibration geometry, and you will find these internal camera parameters change from one project to another. It is always a good practice to use the adjusted camera parameters from previous projects as initial or approximate values in a new adjustment, as it makes it easier for the software to refine new values to suit your new project.

*\*\*Dr. Abdullah is S Chief Scientist and Senior Associate at Woolpert, Inc. He is ASPRS fellow and the recipient of the ASPRS Life Time Achievement Award and the Fairchild Photogrammetric Award.*

The contents of this column reflect the views of the author, who is responsible for the facts and accuracy of the data presented herein. The contents do not necessarily reflect the official views or policies of the American Society for Photogrammetry and Remote Sensing and/or Woolpert, Inc.

## Ad Index

Dewberry		www.dewberry.com		476
Geomni, Inc.		Geomni.net/psm		Cover 4

# GREETINGS FROM THE STUDENT ADVISORY COUNCIL!

**The ASPRS Student Advisory Council (SAC) is excited to have new members joining and helping us to improve the student experience in ASPRS:**

**COUNCIL CHAIR**—VICTORIA SCHOLL

**DEPUTY COUNCIL CHAIR**—BRIANA WILLIAMS

**EDUCATION AND PROFESSIONAL DEVELOPMENT COUNCILOR**—GERARDO ROJAS

**DEPUTY EDUCATION AND PROFESSIONAL DEVELOPMENT COUNCILOR**—YOUSSEF KADDOURA

**COMMUNICATIONS COUNCILOR**—GE (JEFF) PU

**DEPUTY COMMUNICATIONS COUNCILOR**—JASON MCGLAUGHLIN

**NETWORKING COUNCILOR**—SARA DURGAN

**DEPUTY NETWORKING COUNCILOR**—AUSTIN STONE

**SAC ECPC LIASON**—DAVID LUZADER

## **NEW THIS YEAR!**

SAC is planning to feature some of our fellow student members in *Signatures* and on our social media sites. We want to showcase student research, accomplishments, event participation, and related activities. If you are a student member of ASPRS, please submit your Showcase materials to Jeff Pu, SAC Communications Councilor, [gpu100@syr.edu](mailto:gpu100@syr.edu). If you are not a student but know of any outstanding student members who should be featured, please submit their name and contact information to Jeff Pu.

## **FOLLOW US ON SOCIAL MEDIA!**

**Facebook**—<https://www.facebook.com/ASPRS-Student-Advisory-Council-117943608233122/>

**Twitter**—[https://twitter.com/asprs\\_sac?lang=en](https://twitter.com/asprs_sac?lang=en)

This year SAC aims to help improve the student experience in many areas: events at ASPRS conferences, chapter outreach, and upcoming conference opportunities for students.

## **ASPRS CONFERENCES**

**Pecora 21/ISRSE 38**

October 6-11, 2019

<http://pecora.asprs.org/>

**Now ACCEPTING VOLUNTEERS!\***

The joint meeting of the 21st William T. Pecora Memorial Remote Sensing Symposium (Pecora 21) and the 38th International Symposium on Remote Sensing of Environment (ISRSE 38) will convene in Baltimore, Maryland, USA from October 6 – 11, 2019. The conference theme is Continuous Monitoring of Our Changing Planet: From Sensors to Decisions.

\*Visit <http://pecora.asprs.org/volunteer/> for information on volunteering for Pecora 21/ISRSE 38.

## **REGIONAL AND OTHER RELATED CONFERENCES**

**Earth Engine Conference**

September 16-19, 2019

<https://sites.google.com/earthoutreach.org/geoforgood19/>

This Summit will bring together the Earth Engine and Earth Outreach communities to one larger event where scientists, nonprofits and changemakers can learn from each other and potentially collaborate on projects for positive impact for our planet and its inhabitants.

### ASPRS STUDENT ADVISORY COUNCIL

VICTORIA SCHOLL  
COUNCIL CHAIR  
BRIANA WILLIAMS  
DEPUTY COUNCIL CHAIR  
GERARDO ROJAS  
EDUCATION COUNCILOR

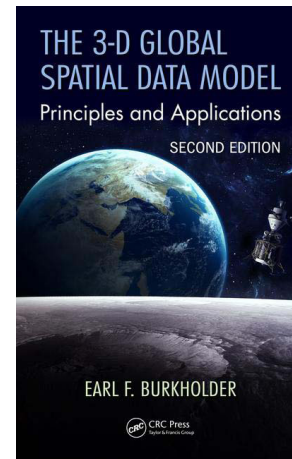
YOUSSEF KADDOURA  
DEPUTY EDUCATION COUNCILOR  
JEFF PU  
COMMUNICATIONS COUNCILOR  
JASON MCGLAUGHLIN  
DEPUTY COMMUNICATIONS COUNCILOR

SARA DURGAN  
NETWORKING COUNCILOR  
AUSTIN STONE  
DEPUTY NETWORKING COUNCILOR  
DAVID LUZADER  
SAC ECPC LIASON

Earl Burkholder is a professional land surveyor, who, until he retired in the latter 2010, held posts at Oregon Institute of Technology and New Mexico State University. During a period of self-employment between the two academic posts, he worked on projects for the Southeastern Wisconsin Regional Planning Commission. These projects confirmed the concepts he proselytized in the first edition of *The 3-D Global Spatial Data Model: Principles and Applications*, published in 2008. Burkholder argues that point information should always be held in a 3D database and located in a three-dimensional, right-handed, rectangular Cartesian coordinate system with the origin located at the center of mass of the Earth. The XY-plane lies in the equatorial plane with the X-axis through the Greenwich meridian. The Z-axis coincides “very nearly with the mean spin axis of the Earth, as defined by the Conventional Terrestrial Pole” (p. 4). Burkholder’s Global Spatial Data Model (GSDM) concept, however, also includes mathematical concepts and procedures that can be used to work with a GSDM repository and compute geospatial information such as coordinates, distances, bearings, and azimuths in the base or other coordinate systems as required. Your reviewer, until he read the book, mistakenly thought that GSDM was some sort of formal standard, but it’s the work of the author, who writes persuasively and competently.

The concepts behind GSDM are not new, but even the basic definition advanced above hints that there is some geodesy in store. After two chapters on GSDM itself, the book continues with three solid chapters that rapidly review spatial data and the science of measurement, mathematical concepts, and geometrical models for spatial data computation. There follow five tougher chapters on geodesy – overview, geometric geodesy, geodetic datums, physical geodesy, and satellite geodesy and Global Navigation Satellite System (GNSS). The foundational material necessary to understand and work with GSDM continues with a chapter on map projections and state plane coordinates and another on spatial data accuracy. The remaining three chapters are concerned with the application of GSDM: computing a linear least squares GNSS network; computing network and local accuracy; and a series of sample projects. There are five technical appendices, the most interesting of which provide short histories of the development of GSDM and the terms “network accuracy” and “local accuracy”, and a ten-page index. For many readers, the value of the book may lie in the ten review chapters: these are best construed as a whistlestop refresher, not an alternative to the major texts on surveying and geodesy that prospective specialists must peruse.

The book is well written and proceeds logically, though some of the review chapters move so fast, for example, the material on map projections, that their utility may be compromised. There are few typos and errors – and most of those are corrected on the website of the author’s company, Global



### **The 3-D Global Spatial Data Model: Principles and Applications, 2<sup>nd</sup> Edition** Earl F. Burkholder

CRC Press, Taylor & Francis Group, Boca Raton, Florida. 2018. xxxii and 492 pp, 4 color and 109 black and white illustrations, tables, index. Hardcover. ISBN 978-1-4987-2216-2. \$116.00. eBook and eBook rental are also available.

**Reviewed by** Stewart Walker, sole proprietor, photogrammetry4u, San Diego, California.

COGO, Inc. The purpose of the book, of course, is to showcase Burkholder’s GSDM, but his palpable enthusiasm results in many repetitions of arguments. Moreover, considerable space in the last three chapters is used to reproduce computer output. This shows the GSDM resources, which are cited copiously and could be of great value to readers interested in adopting the system, but is hard to justify in an expensive hardcover book. All the referenced URLs were viewed in May 2017 – let us hope they still function.

Chapter two is new to the second edition, together with historical material on GSDM and commentary on the new horizontal and vertical definitions to be introduced in 2022 by the National Geodetic Survey. This is revealed in the preface, but the preface to the first edition is reproduced verbatim: it would have been easier on readers if the two had been combined.

Decisions on datums and coordinate systems are more like-

---

Photogrammetric Engineering & Remote Sensing  
Vol. 85, No. 7, July 2019, pp. 473–474.  
0099-1112/19/473–474

© 2019 American Society for Photogrammetry  
and Remote Sensing  
doi: 10.14358/PERS.85.7.473

ly to be taken by surveyors and geodesists in agencies at many levels from national downwards, than by photogrammetrists, remote sensors, or GIS specialists. Nevertheless, this book deserves a wide readership, not only to spur the debate on the value of GSDM, but to provide a succinct overview of modern surveying and geodesy, with an emphasis on computations of points and other quantities from surveying and GNSS data and on transformations between coordinate systems, including the important state plane ones encountered by many readers of this journal.

**ASPRS is proud to partner with CRC Press, Taylor & Francis Group.** We are excited to feature *The 3-D Global Spatial Data Model: Principles and Applications* and other essential books in GIS and Mapping for a discount price to ASPRS members. Visit the ASPRS Bookstore at [www.asprs.org](http://www.asprs.org). Don't forget to apply code **ASP25** to **SAVE 25% on entire purchase\* + FREE Shipping**. Can't find what you're looking for? Visit [crcpress.com](http://crcpress.com) to shop and save on all of their books.

\*Valid for online orders only and excludes eBooks.

## STAND OUT FROM THE REST

### EARN ASPRS CERTIFICATION

ASPRS congratulates these recently Certified and Re-certified individuals:

#### **RECERTIFIED PHOTOGRAMMETRISTS**

**Wallace Scott Dunham, Certification #R1400**

Effective April 19, 2019, expires April 19, 2024

**John Erickson, Certification #R1234**

Effective March 18, 2019, expires March 18, 2024

**L. Bradley Foltz, Certification #R557**

Effective February 7, 2019, expires February 7, 2024

**Angela Livingston, Certification #R1383**

Effective December 8, 2018, expires December 8, 2023

**David K. Nale, Certification #R503**

Effective April 7, 2019, expires April 7, 2024

**Cornell Rowan, Certification #R1055**

Effective March 20, 2019, expires March 20, 2024

**John Schmitt, Certification #R1389**

Effective January 27, 2019, expires January 27, 2024

#### **CERTIFIED MAPPING SCIENTISTS LIDAR**

**Kristian Damkjer, Certification #L042**

Effective May 10, 2019, expires May 10, 2024

**Nima Ekhtari, Certification #L041**

Effective May 14, 2019, expires May 14, 2024

#### **CERTIFIED LIDAR TECHNOLOGIST**

**Matthew J. Doty, Certification #043LT**

Effective May 13, 2019, expires May 13, 2022

#### **CERTIFIED MAPPING SCIENTIST UAS**

**Frank J. Tokar, Jr., Certification #UAS028**

Effective March 21, 2019, expires March 21, 2024

ASPRS Certification validates your professional practice and experience. It differentiates you from others in the profession.

For more information on the ASPRS Certification program: contact [certification@asprs.org](mailto:certification@asprs.org), visit <https://www.asprs.org/general/asprs-certification-program.html>

**asprs** THE IMAGING & GEOSPATIAL INFORMATION SOCIETY





# & GRIDS & DATUMS

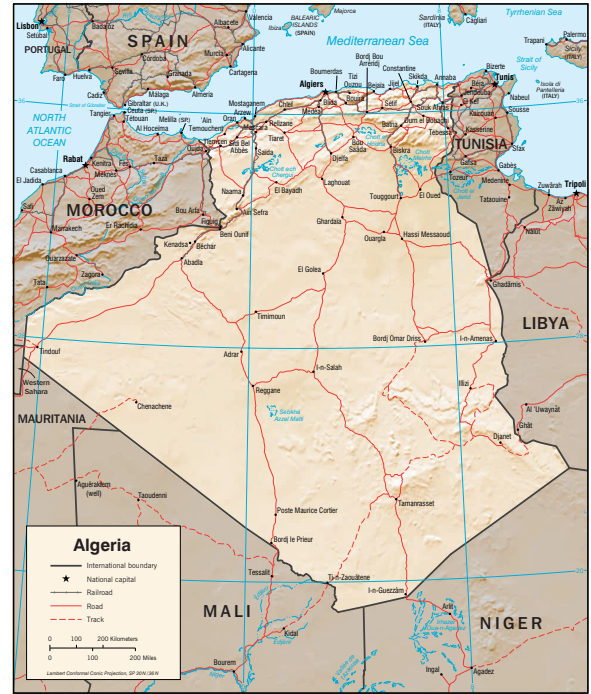
## DEMOCRATIC AND POPULAR REPUBLIC OF ALGERIA

BY Clifford J. Mugnier, CP, CMS, FASPRS

The Grids & Datums column has completed an exploration of every country on the Earth. For those who did not get to enjoy this world tour the first time, *PE&RS* is reprinting prior articles from the column. This month's article on the Democratic and Popular Republic of Algeria was originally printed in 2001 but contains updates to their coordinate system since then.

The area of Northern Africa currently known as Algeria was brought under Roman rule during the Second Punic War (218 – 201 B.C.). It was known to the Romans as Numidia. It was conquered by the Arabs in the 8th century and was mainly under the rule of the Ottoman Empire until 1705, then it was occupied by the French in 1830. Algeria gained independence from France following a referendum of 01 July, 1962. Algeria is the second largest country in Africa after the Sudan, with its coastline on the Mediterranean Sea extending for 998 km. Algeria is bounded by Tunisia and Libya on the east, by Niger and Mali on the south, and on the west by Mauritania, the former Western Sahara, and Morocco. The highest point is Tahat at 3,003 m, and the lowest point is Chott Melrhir at –40 m. Algeria is mostly high plateau and desert; the Atlas and Saharan Atlas Mountains are in the north along with narrow discontinuous coastal plains.

The triangulation of Algeria was carried out by the Dépôt Général de la Guerre from 1854 to 1887. After 1887, the Société Géographique de l'Armée, headquartered in Paris, continued the work. The first-order net of triangulation consists essentially of two parallel chains and three meridional chains. The parallel chains are the coastal chain from the Moroccan to the Tunisian borders (1860-1868) and the chain Ain Sefra-Laghouat-Biskra-Gabes (in Tunisia) (1889-1895). There are also two shorter parallel chains: the Guerara tie chain (1909-1910) and the Southern El Oued tie chain (1909-1910). The meridional chains are the Biskra chain (1872-73, 1899-1902), the Laghouat chain (1886, 1899-1902), and the Saïdia chain (1896-97). Fill nets of first-order complementary, second-order, and third-order triangulations were surveyed from 1864, following the pattern of planned mapping. The survey



work was executed and adjusted in 94 *cartonnés* (books of sections), which progressed south-ward from the coastal areas according to military requirements. These *cartonnés* were numbered in *chronological* sequence of completion. Note that, in the English-language literature of North African Geodesy, one will likely find “carton,” the derivative of *cartonné*.

This original work comprised the Colonne Voirol Datum of 1875, commonly termed Voirol 75. The fundamental point is at the geodetic pillar of the Colonne Voirol Observatory, and the astronomical coordinates are  $\Phi_0 = 36^\circ 45' 07.9''\text{N}$  ( $40^{\text{G}}8357.8''$ ) and  $\Lambda_0 = 3^\circ 02' 49.45''$  East of Greenwich ( $0^{\text{G}}7887.3''$  East of Paris). The reference azimuth from south to Melab el Kora is  $\alpha_0 = 322^\circ 16' 52.7''$  and the ellipsoid of reference is the Clarke 1880 (IGN) where  $a = 6,378,249.2$  m, and  $1/f = 293.4660208$ .

Photogrammetric Engineering & Remote Sensing  
Vol. 85, No. 7, July 2019, pp. 475–478.  
0099-1112/19/475–478

© 2019 American Society for Photogrammetry  
and Remote Sensing  
doi: 10.14358/PERS.85.7.475

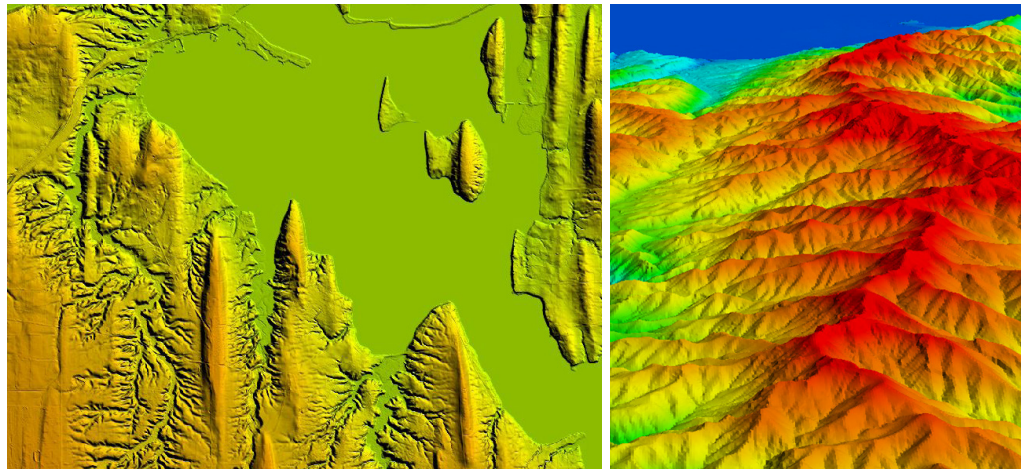
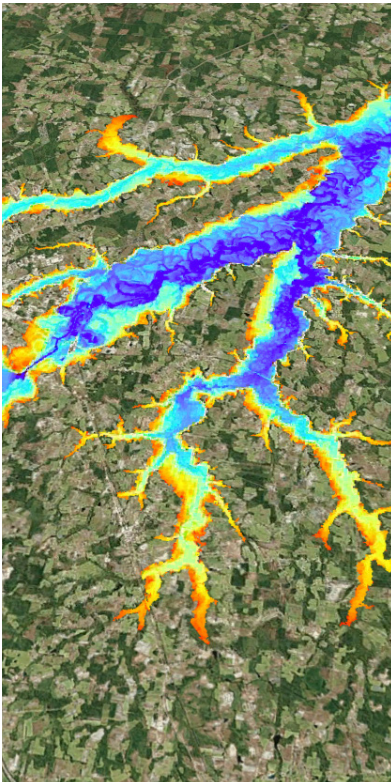
The baselines measured for the Algerian triangulation, with dates of execution, are Blida (1854, 1912), Bône (Annaba) (1866, 1885), Oran (1885, 1910), Laghouat (1914), Ouargla (1920), Mercheria (1932), Biskra (1932), and Navarin (1949). The original mapping was cast on the ellipsoidal Bonne projection – the ubiquitous projection *du jour* for the Europeans of the time. The North African (ellipsoidal) Bonne Grid Latitude of Origin ( $\phi_0$ ) = 35° 06' N (39<sup>G</sup>00 N), the Central Meridian ( $\lambda_0$ ) = 2° 20' 13.95" East of Greenwich, and, some time before WWII, the False Easting and False Northing were changed from zero to 100 km for each. Interestingly, this old Bonne Grid still influences current mapping in that grid limits of the Lambert Conic Grids are still defined by Bonne Grid values. The sheet boundaries of the new Lambert Grids are commonly computed by a reversion of the late Prof. Karl Rinner's Bonne power series formulae published in *Zeitschrift für Vermessungswesen* during the 1930s. That reversion allows cartographers to compute the intersection of a constant Bonne Grid value with a chosen arc of the parallel or of the meridian. Those intersections then were used to define the limits with the graticule of the Lambert Conic Grids computed by John W. Hager of the Defense Mapping Agency (*ex Army Map Service*) in 1974.

Based on original triangulations of the French Army, a local (temporary) Astro station was established in the port city of Oran by Capitaine Faure during 1905-1906. Station

Tafaraoui coordinates are  $\Phi_0 = 39^G 3778.26''$  N and  $\Lambda_0 = 3^G 1532.06''$  East of Paris. The reference azimuth to Tessala is  $\alpha_0 = 62^\circ 09' 57.73''$  and the ellipsoid of reference is the Clarke 1880 (IGN). The observations were later adjusted and used in the 1930 hydrographic survey of that portion of the coast of Algeria and the port of Oran. The Lambert Conic Grid was used by the French Navy for the hydrographic survey.

The reader will notice that I have left off the word “conformal” when describing the Lambert Conic Grids of Algeria. That is because the original systems that succeeded the ellipsoidal Bonne Grid in 1906 were not fully conformal. There are two original zones: for Nord Algerie, the Latitude of Origin ( $\phi_0$ ) = 36° North (40<sup>G</sup>), the Central Meridian ( $\lambda_0$ ) = 2° 42' (3<sup>G</sup>) East of Greenwich, and the Scale Factor at Origin ( $m_0$ ) = 0.999625544. For Zone Algerie Sud, the Latitude of Origin ( $\phi_0$ ) = 33° 18' North (37<sup>G</sup>), the Central Meridian ( $\lambda_0$ ) = 2° 42' (3<sup>G</sup>) East of Greenwich also, and the Scale Factor at Origin ( $m_0$ ) = 0.999625769. The False Origin is 500 kilometers for Eastings and 300 kilometers for Northings for both zones, and the same convention as used in the adjacent Kingdom of Morocco (*PE&RS*, June 1999). The complete replacement of the Bonne Grid for original topographic mapping in Algeria did not happen until 1942.

During the 19<sup>th</sup> century, projection table computations were performed by hand, and all formulae were commonly truncated past the cubic term to ignore infinite series terms consid-



Our geospatial, remote sensing, and GIS professionals are committed to delivering excellence.

**Join our team!**



**Open positions** at [dewberry.com/careers](https://dewberry.com/careers), keyword “geospatial”

Geospatial Resource Lead with lidar production experience, **Fairfax**  
Senior Geospatial Analysts in **Tampa, Denver, Fairfax**

[www.dewberry.com](https://www.dewberry.com)

ered at the time, too small to warrant the extra effort. For instance, the Lambert Conformal Conic projection was used only to the cubic term in the formulae for the tables of the developed meridional distances. This resulted in French Army projection tables that have become part of the arcane lore of computational cartography.

Furthermore, another idiosyncrasy of the French Army formulae is that the Lambert (fully) Conformal Conic projection normally utilizes one of the principal radii of the ellipsoid called the Radius of Curvature in the Plane of the Meridian ( $\rho_0$ ). The French Army instead substituted the Length of the Ellipsoid Normal Terminated by the Semi-Minor Axis ( $v_0$ ) at the Latitude of Origin ( $\lambda_0$ ). Although not strictly conformal, this is the system that was commonly used by the French in all colonies (before WWII) that utilized the Lambert Conic projection (including Syria; *PE&RS*, September 2001).

Standard Lambert formulae will not work for Algeria under certain conditions, and the improper use of the fully conformal projection will yield computational errors that can exceed 15 meters! As an example, consider a test point where  $\phi = 33^\circ$  N and  $\lambda = 3^\circ$  E. For Nord Algerie on the French Army Truncated Cubic Lambert Conic Grid,  $X = 528,064.182$  m and  $Y = -32,764.881$  m; for the same test point on the *Nord Algerie* Lambert fully Conformal Conic Grid,  $X = 528,074.691$  m and  $Y = -32,776.731$  m. The computational difference of the two formulae at the same test point is  $\Delta X = -10.509$  m and  $\Delta Y = +11.850$  m, for a total error of 15.839 meters! Mathematical elegance is not what matters in a country's coordinate transformations; what matters is computational conformity to local legal standards. The certain condition when a fully conformal Lambert Conic will work in Algeria is based on *when* a particular Algerian map was compiled. That is, when the Algerian triangulation was recomputed for the European Datum of 1950, the French dropped usage of the Truncated Cubic version on the old Voirel 75. In summary, for surveys and maps before 1948, one must use the French Army Truncated Cubic Lambert Conic. After 1948, one must use the Lambert fully Conformal Conic. The parameters of the two Lambert zones did not change for the Colonne Voirel Datum of 1875; only the formulae changed. Things soon got more complex.

In 1953-1954 the first-order coastal parallel chain was reobserved by the French. In 1959, the Institut Géographique National (IGN), Paris, readjusted the entire first-order and first-order complementary triangulation to the European Datum 1950 (ED50), incorporating the results of all previous surveys and adjustments. The rule of thumb for this Datum Shift is to increase both Latitude and Longitude from the Colonne Voirel Datum of 1875 to the European Datum 1950. The UTM Grid was used for this purpose, as were all Datums that were transformed to ED50. Like most countries, the ED50 UTM Grid was reserved for military topographic mapping, and local native systems continued in use. That tradition has resulted in some convoluted transformations being perpetuated in Algeria.

The North Sahara Datum of 1959 was obtained (in 1957-1958) by recomputing the results of the first-order nets and

the first-order complimentary nets adjusted to the ED50, but referenced to the Clarke 1880 (modified) ellipsoid where  $a = 6,378,249.145$  m and  $1/f = 293.465$ . The adjustment on the Clarke 1880 (modified) ellipsoid was performed such that it optimized the fit of the shape of the geoid in North Africa, i.e., by reducing to a minimum the sum of the squares of the relative deflections of the vertical in the areas involved. This principle was intended to minimize the mean discrepancies between the geodetic net used in the northern part of Algeria and the astronomic net used primarily in the southern part of Algeria. Some maps were stereocompiled on the North Sahara Datum of 1959 with the UTM Grid at 1:200,000 scale. However, many maps were not cast on the UTM Grid.

The Lambert North Sahara Auxiliary Grid was directly applied to the geodetic coordinates in accordance with the definition of the *Nord Algerie* Zone with the fully conformal formulae. However, it was never used in any publication or in mapping because of the large discrepancies found between the rectangular coordinates of any given point on the Colonne Voirel Datum of 1875 (Voirel 75) or the North Sahara Datum of 1959. This computational experiment is the reason for the development and subsequent adoption of the Lambert Voirel 60 Grid System. This curious system adds 135 meters exactly to the X coordinates and adds 90 meters exactly to the Y coordinates of the original *Nord Algerie* Zone parameters. In other words, the Lambert Voirel 60 Grid has a False Easting = 500,135 m and a False Northing = 300,090 m. According to the French Army in June of 1970, "Under these conditions, when we compare the LAMBERT - VOIROL 75 with the LAMBERT VOIROL 60 coordinates, the shift between the two is always less than 50 m in absolute value. This value does not represent a mathematical relation, but rather the result of comparing the two sets of coordinates. It shows up the inaccuracies in the initial VOIROL 75 system. The maps made with the LAMBERT VOIROL 60 rectangular coordinates are all referenced to the geographic coordinates of the NORTH SAHARA geodetic system." The current parlance for this in English is the "Voirel Unified 1960 Grid" on the "North Sahara Datum of 1959." Note that there is no classical origin for this Datum due to the fact that it is derived from the ED50.

In 1966, the Army Map Service (AMS) developed a series of conversions on a Carton-by-Carton basis for transforming from Voirel 75 to ED50 with UTM coordinates. As an example of the transformation series for Algeria, the following is for coordinates in UTM Zone 31 whose eastings are greater than 355,000 m: Carton 59:  $N = 0.9998873966 n - 0.10000869984 e + 691.561$  m and  $E = 0.9999391272 e + 0.0000869984 n - 416.633$ . The stated RMSE for this Carton is  $\pm 0.200$  m. The adjacent Carton 60, when used with the appropriate coefficients, has a stated RMSE of  $\pm 2.759$  m!

In recent years, the IGN derived a seven-parameter transformation from ED50 to WGS84 for North Africa. The quoted accuracy is  $\pm 2$  m in X, Y, and Z, and, when applying this transformation, the resulting heights are approximately 30 m higher than expected for Algeria. The parameters are  $\Delta X =$

-130.95 m,  $\Delta Y = -94.49$  m,  $\Delta Z = -139.08$  m,  $\Delta s = +6.957$  ppm,  $R_x = +0.4405''$ ,  $R_y = +0.4565''$ , and  $R_z = -0.2244''$ . The U.S. National Imagery and Mapping Agency (NIMA) does not list a three-parameter transformation in TR 8350.2 for transforming from ED50 to WGS84 in Algeria. However, the non-satellite-derived NIMA parameters from the Colonne Voirol Datum of 1875 to WGS84 are  $\Delta X = -73$  m,  $\Delta Y = -247$  m, and  $\Delta Z = +227$  m, with no stated accuracy. NIMA states that, from the Colonne Voirol Unified Datum of 1960 to WGS84, the parameters are  $\Delta X = -123$  m,  $\Delta Y = -206$  m, and  $\Delta Z = +219$  m, and each parameter is stated accurate to  $\pm 25$  m. NIMA further states that, from the North Sahara Datum of 1959 to WGS84, the parameters are  $\Delta X = -86$  m,  $\Delta Y = -93$  m, and  $\Delta Z = +310$  m, and each parameter is stated accurate to  $\pm 25$  m.

Using a  $1^\circ$  by  $1^\circ 30'$  mesh of ED50 coordinates over northern Algeria, a set of 54 North Sahara Datum of 1959 and WGS84 coordinates were derived by others using the transformation developed by IGN. I solved for the three-parameter transformation from the North Sahara Datum of 1959 to WGS84 using the WGS84 Geoid such that  $\Delta X = -131.798$  m,  $\Delta Y = -75.442$  m, and  $\Delta Z = +329.895$  m. The geodetic residual RMS expressed as meters for  $\Delta\phi = \pm 1.74$  m, for  $\Delta\lambda = \pm 1.04$  m, and for  $\Delta h = \pm 4.52$  m. For comparison, I then solved for the North Sahara Datum of 1959 to WGS84 transformation using the EGM96 Geoid such that  $\Delta X = -59.156$  m,  $\Delta Y = -77.366$  m, and  $\Delta Z = +311.265$  m. The geodetic residual RMS expressed as meters for  $\Delta\phi = \pm 2.12$  m, for  $\Delta\lambda = \pm 2.51$  m, and for  $\Delta h = \pm 4.35$  m. In conclusion, because the IGM seven-parameter solution cannot be fully evaluated, the preferred transformation from the North Sahara Datum of 1959 to the WGS84 Datum in the format given in TR 8350.2 is, then,  $\Delta X = -159$  m,  $\Delta Y = -77$  m,  $\Delta Z = +311$  m,  $\Delta\alpha = -112.145$ , and  $\Delta f \times 10^4 = -0.54750714$ .



**ASPRS**  
*Rising Star*  
**PROGRAM**

*Meet Our Rising Stars!*

**Chris Stayte**  
*Sponsored by Woolpert, Inc.*

**Corey Ochsman**  
*Sponsored by Woolpert, Inc.*

**Collin Hutcheson**  
*Sponsored by Merrick & Company*

**Charles Krugger**  
*Sponsored by Stahl Sheaffer Engineering, LLC*

**Kristine Taniguchi-Quan, Ph. D.**  
*Sponsored by Pacific Southwest Region of ASPRS*

The Rising Star program is focused on mentorship of tomorrow's leaders within ASPRS and the geospatial and remote sensing community. Geospatial companies, agencies, and ASPRS regions can all benefit by participation in the program through the advancement and professional development of their employees or associates through the process of sponsorship.

For more information go to [www.asprs.org/rising-star-program](http://www.asprs.org/rising-star-program).

## UPDATE

A significant amount of geodetic research has been performed since the first column on the Grids and Datums of Algeria was published. However, the primary areas of research have been devoted to observations of gravity and of crustal motion in the Atlas Mountain range.

"The REGAT ("REseau Géodésique de l'ATlas") geodetic network is composed of 53 continuously-recording GPS stations distributed in the Algerian Atlas. It spans the whole width of the Algerian coast and reaches 300 km inland, with inter-sites distance of about 100 km. One additional site is located in Tamanrasset in the southernmost part of the country. The network, whose oldest stations started operating in 2007, encompasses the main active tectonic features of the most seismically active segment of the Nubia-Eurasia plate boundary in the Western Mediterranean." (Heliyon, Volume 5, Issue 4, April 2019, e01435)

"The comparisons based on different GPS campaigns provide, after fitting by using the four-parameter transformation, an RMS differences  $\pm 11$ cm especially for the north part of the country over distances of 1 to 1000 km and proves that a good fit between the new quasi-geoid and GPS/levelling data has been reached." (A NEW QUASI-GEOID COMPUTATION FROM GRAVITY AND GPS DATA IN ALGERIA S. A. Benahmed Daho, J. D. Fairhead)

[www.isgeoid.polimi.it/Newton/...2/Benahmed-A%20new%20quasigeoid-revised.pdf](http://www.isgeoid.polimi.it/Newton/...2/Benahmed-A%20new%20quasigeoid-revised.pdf)

The contents of this column reflect the views of the author, who is responsible for the facts and accuracy of the data presented herein. The contents do not necessarily reflect the official views or policies of the American Society for Photogrammetry and Remote Sensing and/or the Louisiana State University Center for GeoInformatics (C<sup>4</sup>G).

This column was previously published in *PE&RS*.

## JOURNAL STAFF

### Editor-In-Chief

Alper Yilmaz, Ph.D., PERSEditor@asprs.org

### Associate Editors

Rongjun Qin, Ph.D., qin.324@osu.edu  
 Michael Yang, Ph.D., michael.yang@utwente.nl  
 Petra Helmholz, Ph.D., Petra.Helmholz@curtin.edu.au  
 Bo Wu, Ph.D., bo.wu@polyu.edu.hk  
 Clement Mallet, Ph.D., clemallet@gmail.com  
 Vasit Sagan, Ph.D., Vasit.Sagan@slu.edu  
 Jose M. Pena, Ph.D., jmpena@ica.csic.es  
 Xin Huang, Ph.D., huang\_who@163.com  
 Prasad Thenkabil, Ph.D., pthenkabil@usgs.gov  
 Ruisheng Wang, Ph.D., ruishwang@ucalgary.ca  
 Desheng Liu, Ph.D., liu.738@osu.edu  
 Valérie Gouet-Brunet, Ph.D., valerie.gouet@ign.fr  
 Yury Vizilter, Ph.D., viz@gosniias.ru  
 Dorota Iwaszczuk, Ph.D., dorota.iwaszczuk@tum.de  
 Qunming Wang, Ph.D., wqm11111@126.com  
 Filiz Sunar, Ph.D., fsunar@itu.edu.tr  
 Norbert Pfeifer, Ph.D., np@ipf.tuwien.ac.at  
 Jan Dirk Wegner, Ph.D., jan.wegner@geod.baug.ethz.ch  
 Hongyan Zhang, Ph.D., zhanghongyan@whu.edu.cn  
 Zhenfeng Shao, Ph.D., shaozhenfeng@whu.edu.cn

### Assistant Editor

Jie Shan, Ph.D., jshan@ecn.purdue.edu

### Contributing Editors

#### Grids & Datums Column

Clifford J. Mugnier, C.P., C.M.S., cjmce@isu.edu

#### Book Reviews

Sagar Deshpande, Ph.D., bookreview@asprs.org

#### Mapping Matters Column

Qassim Abdullah, Ph.D., Mapping\_Matters@asprs.org

#### Sector Insight

Lucia Lovison-Golob, Ph.D., lucia.lovison@sat-drones.com

#### Project Management Column

Raquel Charrois, PMP, CP, CMS, PMP@asprs.org

### ASPRS Staff

#### Assistant Director — Publications

Rae Kelley, rkelley@asprs.org

#### Electronic Publications Manager/Graphic Artist

Matthew Austin, maustin@asprs.org

#### Circulation Manager

Priscilla Weeks, pweeks@asprs.org

#### Advertising Sales Representative

Bill Spilman, bill@innovativemediasolutions.com

## ASPRS IS PARTNERING WITH CRC PRESS – TAYLOR AND FRANCIS

**A**SPRS announces its partnership with CRC Press – Taylor and Francis to offer ASPRS members exclusive discounts on CRC Press titles.

We are excited to feature essential books in GIS and Mapping including *Working with Map Projections: A Guide to their Selection* by Kessler and Battersby, *Topographic Laser Ranging and Scanning: Principles and Processing, 2<sup>nd</sup> Ed.* by Shan and Toth, and many more. For the complete list and to purchase these titles, log into your member account on the ASPRS Bookstore and select the link to CRC Press.

CRC Press is a premier publisher of scientific, technology and medical resources, reaching around the globe to collect essential reference material and the latest advances and making them available to researchers, academics, professionals and students in a variety of accessible formats. CRC Press is a member of Taylor & Francis Group, an informa business. For more information, visit [www.crcpress.com](http://www.crcpress.com).

“We are very pleased to offer this valuable member benefit to ASPRS members” said Priscilla Weeks, Membership Manager—ASPRS.

## ASPRS MEMBERSHIP

ASPRS would like to welcome the following new members!

### At Large

Kevin Blair  
 Robert Blank  
 Lance C. Foster  
 Elisabeth G. Turner  
 Matthew Warren  
 Michael Stephen Weber

### Columbia Riviver

Trevor King

### Florida

Derek Bendell  
 Paul Buchanan  
 Christine Leigh Carlson  
 Luke W. Kratky  
 Jared Phillips  
 Corey Reed Puzzo  
 Morgan LaReine Ridler  
 Robert Yao-Kumah

### Mid-South

Jibrael Ahmad  
 David Barron  
 Aaron Burns

### Potomac

Timothy S. Stryker  
 Brian L. Tolley, CP

### Rocky Mountain

Neal Carter  
 Timothy Nagle-McNaughton  
 Ryan Shields

### Western Great Lakes

Cadan Cummings

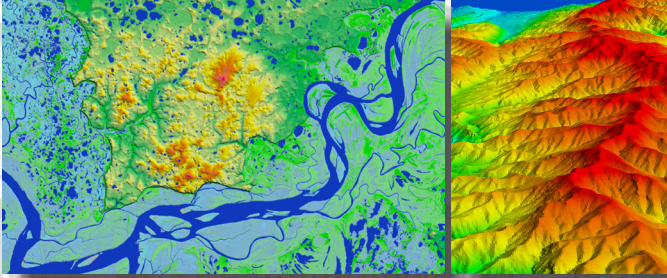
FOR MORE INFORMATION ON ASPRS MEMBERSHIP, VISIT

[HTTP://WWW.ASPRS.ORG/JOIN-NOW](http://WWW.ASPRS.ORG/JOIN-NOW)

*Your path to success in the geospatial community*

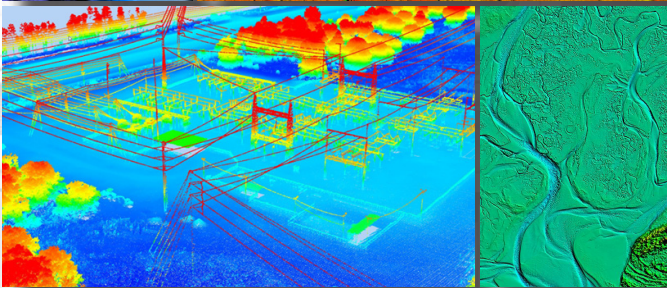
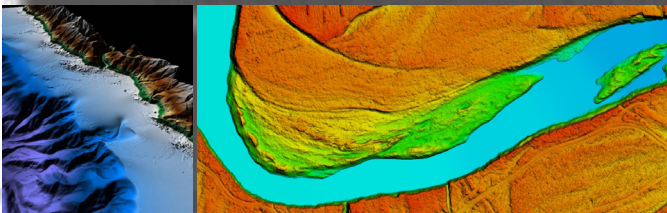
NEW FROM ASPRS AND DEWBERRY

# DEM Users Manual, 3<sup>rd</sup> Edition



## Digital Elevation Model Technologies and Applications: The DEM Users Manual, 3<sup>rd</sup> Edition

Edited by David F. Maune, PhD, CP  
and Amar Nayegandhi, CP, CMS



The 3<sup>rd</sup> edition of the DEM Users Manual includes 15 chapters and three appendices. References in the eBook version are hyperlinked.

Chapter and appendix titles include:

1. Introduction to DEMs
2. Vertical Datums
3. Standards, Guidelines & Specifications
4. The National Elevation Dataset (NED)
5. The 3D Elevation Program (3DEP)
6. Photogrammetry
7. IfSAR
8. Airborne Topographic Lidar
9. Lidar Data Processing
10. Airborne Lidar Bathymetry
11. Sonar
12. Enabling Technologies
13. DEM User Applications
14. DEM User Requirements & Benefits
15. Quality Assessment of Elevation Data
  - A. Acronyms
  - B. Definitions
  - C. Sample Datasets

This book is your guide to 3D elevation technologies, products and applications. It will guide you through the inception and implementation of the U.S. Geological Survey's (USGS) 3D Elevation Program (3DEP) to provide not just bare earth DEMs, but a full suite of 3D elevation products using Quality Levels (QLs) that are standardized and consistent across the U.S. and territories. The 3DEP is based on the National Enhanced Elevation Assessment (NEEA) which evaluated 602 different mission-critical requirements for and benefits from enhanced elevation data of various QLs for 34 Federal agencies, all 50 states (with local and Tribal input), and 13 non-governmental organizations. The NEEA documented the highest Return on Investment from QL2 lidar for the conterminous states, Hawaii and U.S. territories, and QL5 IfSAR for Alaska.

Chapters 1, 3, 5, 8, 9, 13, 14, and 15 are "must-read" chapters for users and providers of topographic lidar data. Chapter 8 addresses linear mode, single photon and Geiger mode lidar technologies, and Chapter 10 addresses the latest in topobathymetric lidar. The remaining chapters are either relevant to all DEM technologies or address alternative technologies including photogrammetry, IfSAR, and sonar.

As demonstrated by the figures selected for the front cover of this manual, readers will recognize the editors' vision for the future – a 3D Nation that seamlessly merges topographic and bathymetric data from the tops of the mountains, beneath rivers and lakes, to the depths of the sea.

Co-Editors

David F. Maune, PhD, CP and Amar Nayegandhi, CP, CMS

DEM Users Manual, 3<sup>rd</sup> Ed.  
Hardback. 2018, ISBN 1-57083-102-5  
Stock # 4959

Hardcopy

List Price \$100

ASPRS Member \$80

Student \$50

\*Plus shipping/handling

<sup>1</sup>Amazon.com

eBook<sup>1</sup>

List Price

\$85

ORDER ONLINE

[HTTPS://WWW.ASPRS.ORG](https://www.asprs.org)



# High-Resolution Large-Area Digital Orthophoto Map Generation Using LROC NAC Images

Kaichang Di, Mengna Jia, Xin Xin, Jia Wang, Bin Liu, Jian Li, Jianfeng Xie, Zhaoqin Liu, Man Peng, Zongyu Yue, Jia Liu, Ruilin Chen, and Changlu Zhang

## Abstract

The Chang'e-5 mission of China is planned to be launched in 2019 to the landing area near Mons Rümker located in Oceanus Procellarum. Aiming to generate a high-resolution and high-quality digital orthophoto map (DOM) of the planned landing area for supporting the mission and various scientific analyses, this study developed a systematic and effective method for large-area seamless DOM production. The mapping results of the Chang'e-5 landing area using over 700 Lunar Reconnaissance Orbiter Camera (LROC) Narrow Angle Camera (NAC) images are presented. The resultant seamless DOM has a resolution of 1.5 m, covers a large area of 20° in longitude and 4° in latitude, and is tied to SLDDEM2015. The results demonstrate that the proposed method can reduce the geometric inconsistencies among the LROC NAC images to the subpixel level and the positional errors with respect to the reference digital elevation model to about one grid cell size.

## Introduction

Mapping of the lunar surface using orbital imagery is one of the fundamental tasks of almost every lunar orbiter mission. Among the common mapping products, digital orthophoto maps (DOMs) are essential for measuring and characterizing lunar surface features. Thus, they are usually used as the base map for morphological and geological analysis (Wu *et al.* 2014; Zhang *et al.* 2016; Yue *et al.* 2017). High-resolution and high-precision DOMs are particularly important for supporting lander and rover missions in terms of landing site analysis, safe landing, and surface operations.

China started the Lunar Exploration Program in 2004, which consists of orbital, soft lander/rover, and sample return missions (Ouyang *et al.* 2004). The first two phases were achieved by the Chang'e-1, Chang'e-2, and Chang'e-3 missions, and the third phase (i.e., sample return mission) will be realized by the Chang'e-5 mission in 2019. The Chang'e-5 mission aims to return about 2 kg of lunar soil and rock samples. Its target area is near Mons Rümker located in Oceanus Procellarum, which is a large area of lunar mare on the northwest region of the Moon (Gbtimes 2017). High-resolution and high-precision mapping of the landing area is critical to support overall mission planning and detailed analysis of

potential sampling sites (Haase *et al.* 2012; Wu *et al.* 2014; Kokhanov *et al.* 2017).

So far, there are a number of lunar global orbital image mosaic maps available, such as Clementine global mosaic (100 m/pixel) (Robinson *et al.* 1999), Lunar Reconnaissance Orbiter Camera (LROC) Wide Angle Camera (WAC) globe mosaic (100 m/pixel) (Arizona State University [ASU] 2011; National Aeronautics and Space Administration [NASA] 2011; Wagner *et al.* 2015), Chang'e-1 CCD camera global mosaic (120 m/pixel) (Li *et al.* 2010), and Chang'e-2 CCD camera global mosaic (7 m/pixel) (Data Publishing and Information Service System of China Lunar Exploration Project 2018; Li *et al.* 2015). However, these products are not sufficient for detailed landing site analysis due to their low resolutions.

The highest-resolution lunar orbital imagery is achieved by the LROC Narrow Angle Camera (NAC), and the images covered nearly the entire lunar surface at a resolution of 0.5–2.0 m. However, there are only a limited number of high-resolution featured mosaics (Klem *et al.* 2014) and digital elevation model (DEM) products (Tran *et al.* 2010; Burns *et al.* 2012) that have been released by the LROC team. The number of images used in most featured mosaics is from two to tens of NAC images. The largest LROC NAC mosaic at present is the LROC Northern Polar Mosaic (<http://lroc.sese.asu.edu/images/gigapan>; NASA/Goddard Space Flight Center/ASU 2014; Wagner *et al.* 2015, 2016), which contains 10 581 NAC images, covering an area from 60°N to the north pole at a resolution of 2 m. However, apparent geometric inconsistencies of up to ~7 pixels were observed due to problems of the designed procedure (Archinal *et al.* 2015). Nevertheless, this product does not cover the Chang'e-5 planned landing area. The spatial coverage of publicly available high-resolution DOMs is very limited. Overall, it is highly desirable to develop effective techniques for large-area high-precision seamless DOM generation.

Photogrammetric processing of high-resolution orbital images for lunar surface mapping has been performed using different software systems or methods, such as the US Geological Survey (USGS) Integrated System for Imagers and Spectrometers (ISIS), SOCET SET, NASA Ames Stereo Pipeline (Moratto *et al.* 2010), and in-house-developed methods. Tran *et al.* (2010) and Burns *et al.* (2012) generated digital terrain models (DTMs) by LROC NAC stereo images with the SOCET SET software. The resultant DTMs have a typical spatial sampling of 2 m and a vertical precision of 1–2 m (Burns *et al.* 2012); the root mean square (RMS) residuals are typically ~0.25 pixels for a pair of NAC stereo images and less than 1 pixel for multiple sets of stereo images (Tran *et al.* 2010). Klem *et al.* (2014) produced a controlled mosaic for LROC NAC images using the USGS ISIS software, and the seam precision for the mosaics was generally within 7–8 pixels. Lee *et al.* (2012) and

---

Kaichang Di, Bin Liu, Zhaoqin Liu, Man Peng, Zongyu Yue, Ruilin Chen, and Changlu Zhang are with the State Key Laboratory of Remote Sensing Science, Institute of Remote Sensing and Digital Earth, Chinese Academy of Sciences, Beijing 100101, China (liubin@radi.ac.cn).

Mengna Jia, Xin Xin, and Jia Liu are with the State Key Laboratory of Remote Sensing Science, Institute of Remote Sensing and Digital Earth, Chinese Academy of Sciences, Beijing 100101, China; and the University of Chinese Academy of Sciences, Beijing 100049, China.

Jia Wang, Jian Li, and Jianfeng Xie are with the Beijing Aerospace Control Center, Beijing, 100094, China.

Photogrammetric Engineering & Remote Sensing  
Vol. 85, No. 7, July 2019, pp. 481–491.  
0099-1112/19/481–491

© 2019 American Society for Photogrammetry  
and Remote Sensing  
doi: 10.14358/PERS.85.7.481

Archinal *et al.* (2015) used USGS ISIS to generate controlled polar mosaics from LROC NAC images. The residuals were within 1 pixel with a maximal error of  $\sim 7$  pixels, and the horizontal accuracy of the mosaics was within 100 m with respect to the Lunar Orbiter Laser Altimeter (LOLA) data (Lee *et al.* 2012).

Wu *et al.* (2014) developed a combined block adjustment method to process Chang'e-2 stereo imagery and LOLA data of the Chang'e-3 landing area. The resultant DTM has an average elevation difference of 15.19 m and a standard deviation of 17.08 m compared to that of the LOLA DEM. Di *et al.* (2014) developed a self-calibration bundle adjustment method for Chang'e-2 stereo images to reduce the georeferencing inconsistencies among the images of adjacent orbits from up to 20 pixels to a subpixel level. Kokhanov *et al.* (2017) used a self-developed photogrammetric method to obtain cartographic products of potential landing sites for the "Luna-25" mission from 11 LROC NAC stereo pairs. The bundle adjustment results had precisions of 0.3 m and 1.0 m in the planar direction and 3.5 m in the vertical direction. Haase *et al.* (2012, 2014) produced a DTM and ortho-mosaic for the Apollo-17 landing site using LROC NAC stereo images. The LROC-adapted German Aerospace Center photogrammetric processing chain was used for stereo image processing, and the resultant DTM had a standard deviation of 40 cm in elevational difference with the LOLA profiles.

As previously described, existing lunar mapping research is generally based on stereo images. However, the LROC NACs can only acquire stereo images from adjacent orbits using off-nadir slew in limited interested locations, and most of the time, the captured NAC images have nadir orientation. There are only a few NAC stereo pairs in the Chang'e-5 planning landing area because the nadir NAC images cannot be used to generate a high-resolution DOM mosaic using stereo photogrammetric methods. Furthermore, most of the existing studies have been focused on photogrammetric processing involving several or tens of images. For large-area mapping, the geometric and radiometric inconsistencies are more severe and complicated. Therefore, it is necessary to develop a more effective method to produce high-precision DOM mosaics for large areas using nonstereo NAC images and a lunar control source of limited resolution.

This research aimed to develop a systematic and effective method for generating a seamless DOM for the planned Chang'e-5 landing area. In this work, we used a two-step strategy. First, the study area was divided into several overlapped subareas, and a planar block adjustment with control points was applied to each subarea to lower the geometric deviations among the NAC images to the subpixel level at the same time of tying the NAC images to the reference SLDEM2015. Then a seamless DOM mosaic of each subarea was generated. Second, the thin plate spline (TPS) model (Wahba 1990) was applied to the subarea DOMs to remove the positional inconsistencies between the adjacent subarea DOMs and guarantee seamless DOM mosaicking throughout the whole research area. Using the proposed two-step method, a controlled seamless mosaic of the Chang'e-5 landing area was created with high geometric precision and with a resolution of 1.5 m.

## Data

The planned landing area of Chang'e-5 mission was chosen to verify the proposed large-area DOM generation method. It locates near Mons Rümker within Oceanus Procellarum and covers an area of approximately  $20^\circ$  longitude  $\times$   $4^\circ$  latitude, or approximately  $413.8 \text{ km} \times 121.4 \text{ km}$  (Di *et al.* 2018). LROC NAC images were the data source used in this research. SLDEM2015, a combined product of LOLA laser altimetry and DEMs generated from the Japanese Selenological and Engineering Explorer (SELENE) terrain camera images (Barker *et al.* 2016), was used as reference DEM for ortho-rectification. Figure 1 shows the planned landing area of Chang'e-5 on the LROC WAC mosaic.

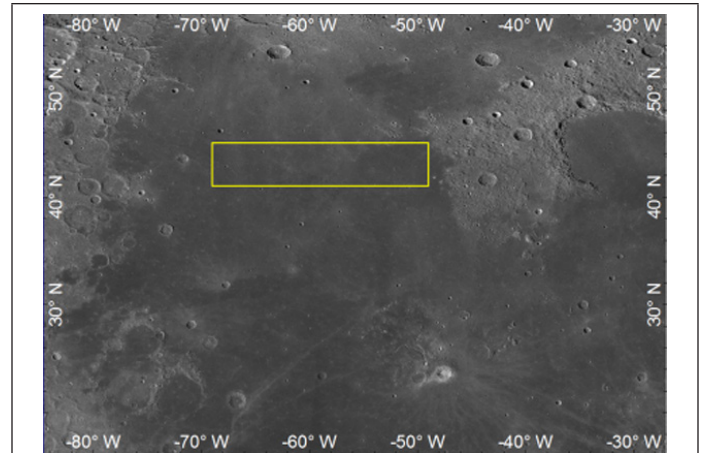


Figure 1. Planned landing area of Chang'e-5 marked as a rectangle on the LROC WAC mosaic.

## LROC NAC Images

The LROC is a system of three cameras onboard the Lunar Reconnaissance Orbiter (LRO) that captures high-resolution monochromatic images and moderate-resolution multispectral images of the lunar surface. It consists of two NACs that are designed to provide 0.5–2.0 m/pixel monochromatic narrow-angle line scan images and a WAC that provides images at a scale of 100 m/pixel in seven color bands over a 60-km swath (Robinson *et al.* 2010).

NAC Experimental Data Record images were downloaded from the NASA Planetary Data System (PDS) and preprocessed using the USGS ISIS software. SPICE kernels (NAIF 2014) were attached to each image using the "spiceinit" command, and radiometric corrections and removal of echo effects were realized by the "Ironaccal" command and the "Ironacecho" command, respectively (PDS 2014; Henriksen *et al.* 2016). Until December 2017, the planned Chang'e-5 landing area is covered by about 2299 LROC NAC images. Considering the illumination conditions, most of the chosen images have similar solar azimuth angles that are higher than  $180^\circ$  (afternoon images) and incidence angles between  $40^\circ$  and  $80^\circ$ . The planned landing area could not be completely covered with afternoon images, so small gaps were filled with one or two morning images. A total of 765 NAC images were involved in this research with a ground sample distance of mainly 1.5 m.

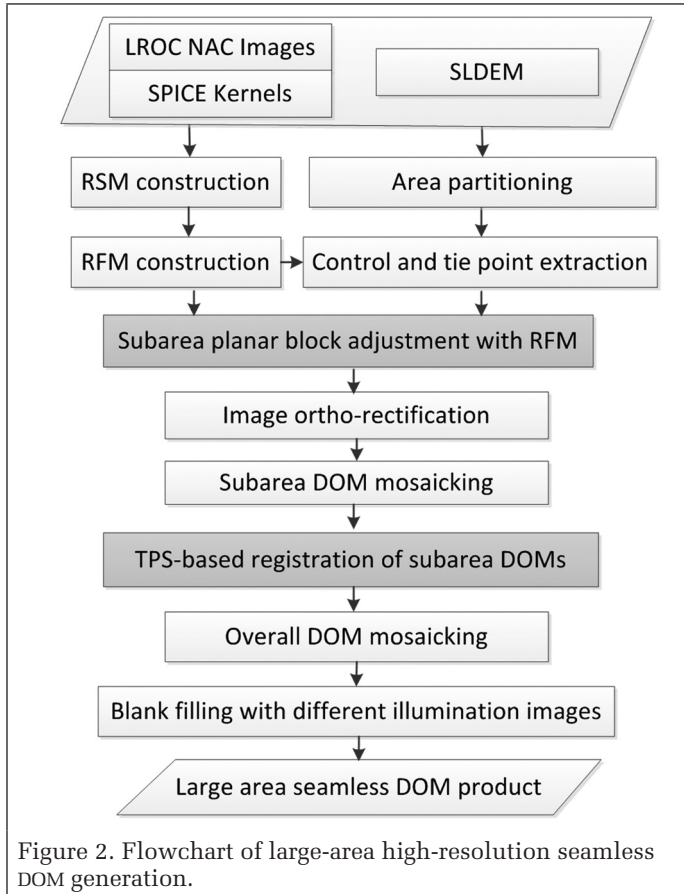
## Control Source

SLDEM2015 was used as the control source for providing three-dimensional control points in the block adjustment stage as well as providing topographic correction during DOM generation. This product is a lunar shape model generated by a combination of LOLA and SELENE data. This includes 43 200 stereo-derived DEMs from SELENE Terrain Camera images and 4.5 billion surface heights from LOLA (Barker *et al.* 2016). The resultant near-global lunar DEM has an effective resolution of approximately 60 m at the equator and a typical vertical accuracy of approximately 3–4 m. In addition, the LROC WAC mosaic (NASA 2011; Wagner *et al.* 2015) was used as a reference for grayscale balancing in the image mosaicking process.

## Method for Large-Area Controlled DOM Generation

In this research, a two-stage method was used to generate a large-area controlled seamless DOM. Figure 2 is the flowchart showing the generation process of large-area seamless DOM. To guarantee both the processing efficiency and mapping precision, the large landing area was partitioned into 10 subareas and processed in parallel. Dividing the whole mapping area into some subareas is a common strategy when dealing with

large-area or global mapping, especially in the planetary mapping field (Gwinner *et al.* 2010, 2016; Preusker *et al.* 2017). Mapping with partitions is an engineering method for parallel processing and dealing with huge amounts of data. It is also a feasible way to improve the processing precision when the data are of different quality in different regions, which is very common with the planetary orbital images (Gwinner *et al.* 2016).



A planar block adjustment with control points was used in each subarea to ensure the relative consistency among the LROC NAC images and the absolute accuracy to the control source. The rational function model (RFM) of the image was refined during the block adjustment. Via the block adjustment, geometric inconsistencies between adjacent LROC NAC images within each subarea can be effectively reduced. Subsequently, the DOM of each image was automatically generated, and the DOMs within each subarea were mosaicked together. Because of the resolution limitation of the reference source, some positional inconsistencies between the DOM mosaics of neighboring subareas remained. Therefore, a TPS model-based image registration was applied to the generated subarea DOM mosaics. To maintain the grayscale and contrast homogeneity, a histogram matching-based grayscale balancing method was applied to all the DOMs. Finally, a seamless DOM product of the entire planned landing area was generated via mosaicking.

It is worth mentioning that the contrast of the WAC mosaic is lower than most NAC images, which causes the NAC mosaic to appear a little grayish. Nevertheless, the WAC mosaic provides a very consistent source in a larger scale so that the produced mosaic has a good radiometric consistency, which can satisfy most of the applications at present. Color balancing for large-area mapping deserves future research.

## Geometric Models of Orbital Imagery

The geometric model of the imagery is the mathematical basis for block adjustment as well as the image ortho-rectification. It builds the relationship between object-space coordinates and image-space coordinates.

The rigorous sensor model (RSM) of an image represents the imaging process by collinearity equations with interior orientation (IO) parameters and exterior orientation (EO) parameters (Di *et al.* 2014; Henriksen *et al.* 2016; Liu *et al.* 2017). The generic geometric model of an image fits the relationship between the image and ground coordinates via mathematical functions, the parameters of which have no physical meaning related to the imaging process. The most commonly used generic geometric model is the RFM. The RFM has the advantages of high fitting precision, simple and uniform form, high calculation speed, and imaging sensor independence. It has already been widely accepted that the RFM can approximate the RSM at a precision of 1/100 pixel in image space (Liu *et al.* 2016, 2017) such that it can be used to replace RSM without a loss of accuracy.

The RSM of the NAC imagery was constructed using the IO and EO parameters recorded in SPICE kernels (NAIF 2014). It can be generally described (Di *et al.* 2014) as

$$\begin{bmatrix} X - X_s \\ Y - Y_s \\ Z - Z_s \end{bmatrix} = \lambda R_{ol} R_{bo} R_{ib} \begin{bmatrix} x \\ y \\ -f \end{bmatrix} = \lambda R \begin{bmatrix} x \\ y \\ -f \end{bmatrix} \quad (1)$$

where  $(x, y)$  are the focal plane image coordinates;  $f$  is the focal length;  $(X, Y, Z)$  and  $(X_s, Y_s, Z_s)$  represent the lunar-surface-point coordinates and the position of optical center in the lunar body-fixed coordinate system (LBF), respectively;  $\lambda$  is a scale factor;  $R_{ib}$  is the rotational matrix from the image space coordinate system to the spacecraft body coordinate system (BCS);  $R_{bo}$  is the rotational matrix from the BCS to the orbit coordinate system (OCS);  $R_{ol}$  is the rotational matrix from the OCS to the LBF; and  $R$  is the combination of these three rotation matrices and can be constructed using the three EO angle parameters  $(\omega, \phi, \kappa)$  (Liu *et al.* 2017).

In principle, for linear array push-broom images, each line has a different set of EO parameters. Because the time interval of the orbit measurement is much longer than that of the line scanning, only a small portion of the image lines have EO parameters from direct measurements. To obtain the EO parameters of all image lines via interpolation, the EO parameters are usually interpolated with respect to the scan time  $t$  (Di *et al.* 2014). There are many methods for EO parameter interpolation. The polynomial representation is a feasible choice and widely used. The third-order polynomial is chosen to model the EO parameters as shown in Equation 2:

$$\begin{aligned} X_s(t) &= a_0 + a_1 t + a_2 t^2 + a_3 t^3 \\ Y_s(t) &= b_0 + b_1 t + b_2 t^2 + b_3 t^3 \\ Z_s(t) &= c_0 + c_1 t + c_2 t^2 + c_3 t^3 \\ \phi(t) &= d_0 + d_1 t + d_2 t^2 + d_3 t^3 \\ \omega(t) &= e_0 + e_1 t + e_2 t^2 + e_3 t^3 \\ \kappa(t) &= f_0 + f_1 t + f_2 t^2 + f_3 t^3 \end{aligned} \quad (2)$$

where  $a_0, a_1, \dots, f_3$  are the polynomial coefficients of the six EO parameters  $(X_s, Y_s, Z_s, \omega, \phi, \kappa)$ .

The focal plane image coordinates  $(x, y)$  can be obtained by transforming from the image coordinates (*row, sample*) using IO parameters as follows:

$$x_d = (\text{sample} - \text{BORESIGHT\_SAMPLE}) \cdot \text{PIXEL\_PITCH} \quad (3)$$

$$r = x_d \quad (4)$$

$$x = x_d / (1 + k_1 \cdot r^2) \quad (5)$$

where *PIXEL\_PITCH* is the pixel size of the image, *BORESIGHT\_SAMPLE* is the principal point coordinate,  $x_d$  is the distorted position (the measured position),  $r$  is the distance between the optical center and image point,  $k_1$  is the distortion coefficient, and  $x$  is the corrected focal plane position in millimeters (mm). The IO parameters of the left and right cameras (NAC-L and NAC-R) can be found in the SPICE kernels of the LRO mission. The NAC cameras are line scanners (single-line CCD);  $y_d$  is unmeasured and probably unimportant, and thus  $y$  is assumed to be zero according to the LROC Instrument Kernel file (NAIF 2014; Liu *et al.* 2017).

The RFM is represented as the ratio of the polynomials shown in Equation 6 as follows:

$$\begin{aligned} r_n &= \frac{P_1(X_n, Y_n, Z_n)}{P_2(X_n, Y_n, Z_n)} \\ c_n &= \frac{P_3(X_n, Y_n, Z_n)}{P_4(X_n, Y_n, Z_n)} \end{aligned} \quad (6)$$

where  $(r_n, c_n)$  and  $(X_n, Y_n, Z_n)$  are the normalized image coordinates and ground coordinates, respectively. The third-order polynomial  $P_i$  ( $i = 1, 2, 3,$  and  $4$ ) has a general form as follows:

$$\begin{aligned} P_i(X_n, Y_n, Z_n) &= a_1 + a_2 X_n + a_3 Y_n + a_4 Z_n + a_5 X_n Y_n + a_6 X_n Z_n + a_7 Y_n Z_n + a_8 X_n^2 \\ &+ a_9 Y_n^2 + a_{10} Z_n^2 + a_{11} X_n Y_n Z_n + a_{12} X_n^3 + a_{13} X_n Y_n^2 + a_{14} X_n Z_n^2 + a_{15} X_n^2 Y_n + a_{16} Y_n^3 \\ &+ a_{17} Y_n Z_n^2 + a_{18} X_n^2 Z_n + a_{19} Y_n^2 Z_n + a_{20} Z_n^3 \end{aligned} \quad (7)$$

where  $a_1, a_2 \dots$  to  $a_{20}$  are the coefficients of the polynomial function  $P_i$ , named rational polynomial coefficients (RPCs).

The RFM of the LROC NAC imagery was established by least-squares fitting with a large number of virtual control points generated by RSM of the image (Di *et al.* 2018). A series of grid points in a certain interval were created first in every image as the virtual control points in image space, after which the elevation in the object space was divided into several layers and the planar ground coordinates of the virtual control points in every layer were calculated using the RSM. Finally, the RPCs were derived using these virtual control points via least-squares fitting (Liu *et al.* 2017).

### Subarea Planar Block Adjustment

The accuracy of the constructed RSM of LROC NAC imagery depends on the accuracy of the orbit and attitude of the LRO. Consequently, the fitted RFM also contains errors at the same level as that of the RSM. Benefiting from lunar gravity field data of the Gravity Recovery and Interior Laboratory mission, the LRO orbit determination obtained an accuracy of ~20 m. The accuracy was further improved to ~14 m after incorporating crossovers of LOLA data (Mazarico *et al.* 2012). The errors of the RSMs and RFMs of the images cause positional deviations of adjacent rectified images that should be reduced to a subpixel level to better support engineering and science applications.

Photogrammetric block adjustment is an effective means to improve the geopositioning accuracy of a geometric model (Gwinner *et al.* 2010; Wu and Liu 2017). Traditionally, three-dimensional ground coordinates of the tie points are solved using stereo block adjustment. However, if the stereo convergence angle is very small (e.g., <10°), the normal equations of the block adjustment will be ill-conditioned, and as a result, the calculated ground height will be abnormal. This is widespread in our experiments because of the lack of coverage of stereo LROC NAC pairs.

The traditional DOM registration is also a widely used method to remove the geometric deviations between images with low convergence angles. This is usually accomplished with the help of high-precision control data. However, the lack of high-precision control data of the lunar surface limits the registration precision. It is hard to make the NAC DOMs geometric seamless by using the traditional registration method with control points from presently available DOM mosaics or DEMs.

To resolve the problem, a DEM-aided planar block adjustment was developed to refine the RFMs of the LROC NAC images. In order to ortho-rectify the LROC NAC images and support collaborative analysis of produced DOM mosaic and existing DEM in various science applications, the geometric models of the images should be corresponded to the reference DEM. Thus, in each subarea block adjustment, a few control points were manually selected using SLDEM2015 as the reference. The control points are mostly centers of small craters and are evenly distributed in the research area. The extracted feature points in every NAC image are matched automatically to obtain tie points. After that, the distribution of tie points is checked carefully to ensure that every overlapping area has evenly distributed points. If such a condition is not satisfied, manually selected tie points will be used. Most of the NAC images (750 out of 765 images used) were taken in the afternoon and have similar illumination conditions, and they can be automatically matched for tie point selection. A very small number of images (15) were taken in the morning and have severe illumination differences with neighboring images taken in the afternoon, and manual selection is necessary to obtain tie points in these images. Image matching under different illumination condition is still a challenging issue. Recently, Wu *et al.* (2018) have done some related work in automatic matching of planetary images using illumination-invariant feature points. The issue is worth of further study to make the adjustment process more efficient.

The error equations of the block adjustment are shown in Equation 8. Compared to stereo block adjustment, planar block adjustment is a method that calculates only the tie point ground plane coordinates, while the elevation coordinates can be interpolated from a DEM. In the block adjustment, the affine transformation model in image space (Equation 8) is used to compensate the systematic errors rather than recalculating the RPCs:

$$\begin{aligned} F_x &= e_0 + e_1 \cdot \text{sample} + e_2 \cdot \text{line} - x \\ F_y &= f_0 + f_1 \cdot \text{sample} + f_2 \cdot \text{line} - y \end{aligned} \quad (8)$$

where the image coordinates acquired by back-projecting the ground coordinates with the RFM (as shown in Equation 6) are represented by *sample* and *line*, while the measured image coordinates are shown as  $x$  and  $y$ ;  $e_0, e_1, e_2$  are the affine transformation parameters in the sample direction, and  $f_0, f_1, f_2$  are the affine transformation parameters in the line direction.

Because the error equations of planar block adjustment are nonlinear relative to the ground coordinates, a Taylor series expansion is used to linearize the error equations as shown in Equation 9. The unknowns to be solved include the tie point ground planar coordinates ( $lat, lon$ ) and the affine transformation model parameters as shown in Equation 9. The elevation coordinates are interpolated from a DEM iteratively:

$$\begin{aligned} v_x &= \frac{\partial F_x}{\partial e_0} \cdot \Delta e_0 + \frac{\partial F_x}{\partial e_1} \cdot \Delta e_1 + \frac{\partial F_x}{\partial e_2} \cdot \Delta e_2 + \frac{\partial F_x}{\partial lat} \cdot \Delta lat + \frac{\partial F_x}{\partial lon} \cdot \Delta lon - l_x \\ v_y &= \frac{\partial F_y}{\partial f_0} \cdot \Delta f_0 + \frac{\partial F_y}{\partial f_1} \cdot \Delta f_1 + \frac{\partial F_y}{\partial f_2} \cdot \Delta f_2 + \frac{\partial F_y}{\partial lat} \cdot \Delta lat + \frac{\partial F_y}{\partial lon} \cdot \Delta lon - l_y \end{aligned} \quad (9)$$

The error equations for control points are shown in Equation 10, and only the affine transformation parameters need to be calculated for control points:

$$\begin{aligned} v_x &= \frac{\partial F_x}{\partial e_0} \cdot \Delta e_0 + \frac{\partial F_x}{\partial e_1} \cdot \Delta e_1 + \frac{\partial F_x}{\partial e_2} \cdot \Delta e_2 - I_x \\ v_y &= \frac{\partial F_y}{\partial f_0} \cdot \Delta f_0 + \frac{\partial F_y}{\partial f_1} \cdot \Delta f_1 + \frac{\partial F_y}{\partial f_2} \cdot \Delta f_2 - I_y \end{aligned} \quad (10)$$

The error equations of each control point and tie point can be constructed using Equations 9 and 10. The unknown parameters can be calculated iteratively using the least-squares algorithm until the termination condition of iteration is satisfied.

In this research, the planar block adjustment was conducted in each subarea independently. Using the RPCs and the calculated affine transformation parameters, the NAC images were ortho-rectified with respect to SLDEM2015, through which the image distortions caused by topographic relief and the imprecision of the original EO parameters were simultaneously corrected. Finally, the subarea seamless DOM mosaic was produced using the individual DOMs within the subarea.

### TPS-Based Large-Area Image Registration

The planar block adjustment can remove the geometric deviations among images within each subarea, but inconsistencies remain among the subarea DOM mosaics because of the limited control precision. Therefore, registration between subarea mosaics is needed to eliminate the residual geometric inconsistencies. We propose a novel method of TPS model-based large-area image registration to seamlessly register the subarea DOMs while simultaneously maintaining mapping accuracy.

The TPS model is an effective technique for data interpolation and smoothing and has been widely used in image alignment, shape matching, image warping, spatial data interpolation, and other circumstances that require the modeling of nonrigid deformation. As shown in Equation 11, the TPS model consists of an affine transformation model and a distance-related quantity that indicates that the impact of the control point on the interpolation point depends on the distance between them:

$$f(x, y) = \alpha_0 + \alpha_1 x + \alpha_2 y + \sum_{(j=1)}^m \delta_j \psi(r_j) \quad (11)$$

where the quantity of control points are represented by  $m$  and  $r_j$  is the Euclidean distance from the  $j$ th control point  $(x_j, y_j)$  to an arbitrary image point  $(x, y)$  as follows:

$$r_j = \sqrt{(x - x_j)^2 + (y - y_j)^2} \quad (12)$$

where  $\psi$  is the radial-basis-function kernel

$$\psi(r) = \begin{cases} r^2 \log(r), & r \neq 0 \\ 0, & r = 0 \end{cases} \quad (13)$$

and  $\alpha_0, \alpha_1, \alpha_2$ , and  $\delta_j$  in Equation 12 are the coefficients that should be calculated by minimizing the weighted sum of the error measure  $E(f)$  (Equation 15) and roughness measure  $R(f)$  (Equation 16) (Di *et al.* 2018) as follows:

$$\min(E(f) + \lambda R(f)) \quad (14)$$

$$E(f) = \sum_{(j=1)}^m \|z_j - f(x_i, y_j)\|^2 \quad (15)$$

$$R(f) = \iint \left( \left( \frac{\partial^2 f}{\partial^2 x^2} \right)^2 + 2 \left( \frac{\partial^2 f}{\partial x \partial y} \right)^2 + \left( \frac{\partial^2 f}{\partial^2 y^2} \right)^2 \right) dx dy \quad (16)$$

where  $\lambda$  represents a smoothing parameter that is required to be nonnegative. If  $\lambda = 0$ , there will be no smoothness constraint, and all the control points are exactly passed through when fitting the TPS model. Otherwise, if  $\lambda = +\infty$ , the coefficient  $\delta$  becomes a zero vector, and the TPS model will turn into an affine transformation model (Shen *et al.* 2017). The variable  $\lambda$  was set to be zero in our experiment so that the registration precision can reach as high a level as possible for the control point pairs and the surrounding area. It is also a guarantee for the subsequent registration process to be implemented simultaneously.

When registering the subarea DOMs with the TPS model, a subarea DOM in the central part of the whole area was used as the reference for neighboring DOMs. Then the registered DOMs become new references for subsequent subarea mosaics until all the subarea DOMs are registered.

For DOM registration, the TPS coefficients are calculated by the matched reference control points and auxiliary control points. The reference control points are the matched points between the target DOM and the reference DOM, while the auxiliary control points are on the opposite-side margin of the target DOM, which are introduced to constrain the geometric error in the local area and avoid overcorrection of the DOM. For example, in Figure 3, the subarea DOM labeled “Left DOM” needs to be registered to the “Reference DOM,” so the reference control points were on the right margin of the “Left DOM,” shown as circles, while the auxiliary control points were marked as crosses and distributed on the left margin of the “Left DOM.” Consequently, when solving TPS coefficients, the reference control point coordinates of the target DOM were corrected with respect to the reference DOM. The coordinates

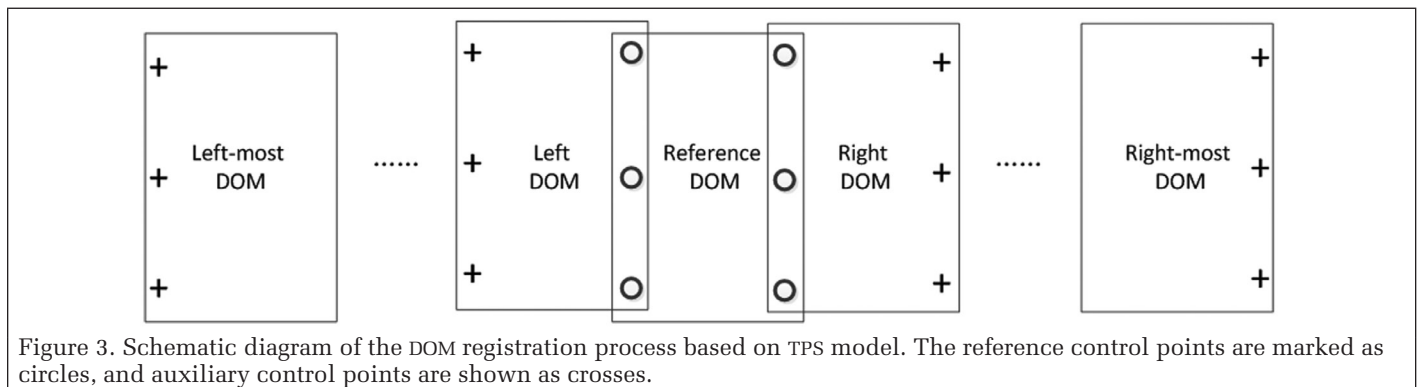


Figure 3. Schematic diagram of the DOM registration process based on TPS model. The reference control points are marked as circles, and auxiliary control points are shown as crosses.

of the auxiliary control point remain unchanged. Other coordinates in the target DOM were smoothly transformed using the calculated TPS coefficients.

The whole registration process can be implemented simultaneously with all the control points matched in advance. To be specific, the homologous points between every two subarea DOMs are obtained first as reference or auxiliary control points. These control points will be unchanged during the whole registration process. Then the TPS model for every target DOM is established in parallel with the achieved control points. Thus, the registration of every target DOM can be implemented independently and simultaneously. Finally, the DOM mosaic of the entire landing area was generated in high geometric consistency.

## Results and Analyses

### Planar Block Adjustment Results

The whole planned Chang'e-5 landing area was partitioned into 10 subareas in longitude. The subareas covered approximately 3° in longitudinal direction with an overlap of 1°. The 10 subareas from left to the right were named Parts 1 to 10. The quantity of LROC NAC images in every subarea is displayed in Table 1

together with the control point and tie point numbers for the planar block adjustment. The borders of each subarea overlapping on the selected NAC images are depicted in Figure 4.

The planar block adjustment was performed on the 10 subareas separately, and the results are shown in Table 2. The unit of all the precision assessment results is one NAC image pixel, which is set to be 1.5 m in this research. The control point precision was evaluated in image space by the RMS errors between the back-projected coordinates and the measured-image coordinates. As shown in Table 2, the RMS errors for the control points are approximately 27 NAC image pixels on average, which is about one grid cell size of the SLDEM2015 in the research area, with the maximum error no more than two grid cell size, reflecting that the subarea DOMs are connected well to the SLDEM2015. As for the tie points, the RMS errors were also measured by the difference between the matched image coordinates and the back-projected image coordinates. The RMS errors of tie points, as shown in Tables 1 and 2, are approximately one-half of an NAC image pixel in every part, which indicates that the geometric consistencies of NAC images in the subareas were effectively improved after planar block adjustment.

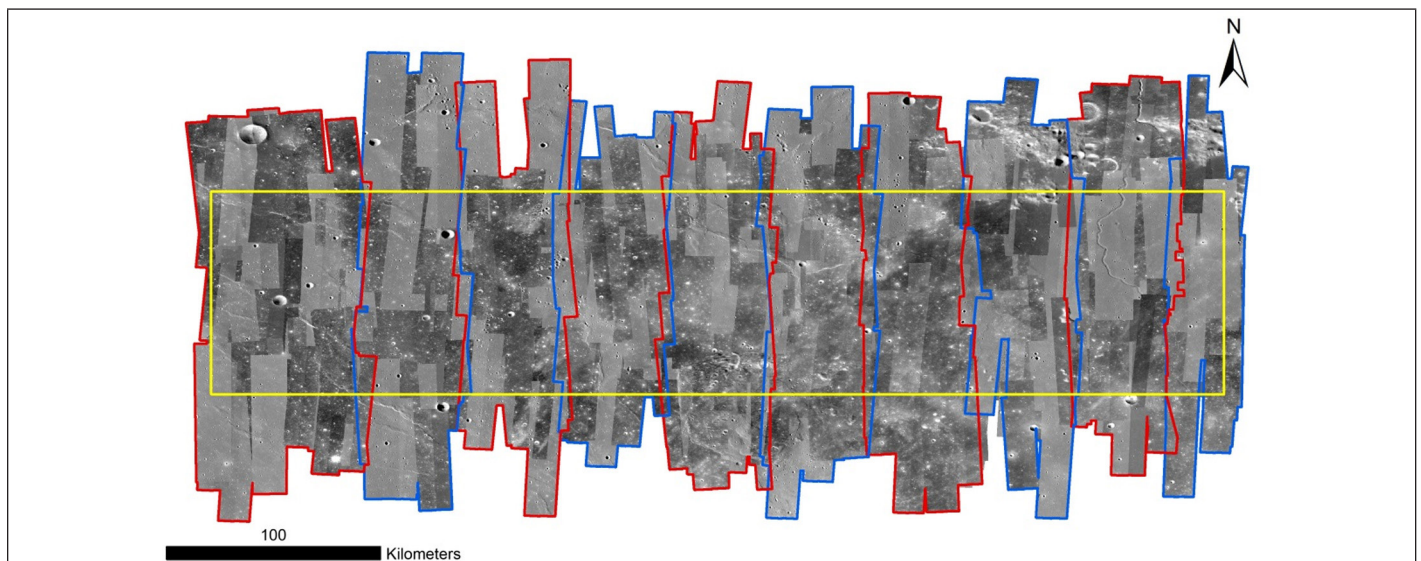


Figure 4. Footprints of all the selected LROC NAC images and the borders of the 10 subareas. Red and blue colors are used alternately for distinguishing the subarea borders. The yellow rectangle represents the planned landing area of Chang'e-5.

Table 1. Image numbers, control point, and tie point numbers in the ten subareas.

Subarea ID	Part 1	Part 2	Part 3	Part 4	Part 5	Part 6	Part 7	Part 8	Part 9	Part 10
Image number	111	71	73	56	93	84	74	54	85	49
Control point number	8	10	11	10	9	11	11	8	9	8
Tie point number	46 386	39 279	49 005	47 174	48 243	48 253	51 425	35 485	41 601	31 148

Table 2. Control point and tie point precisions of the planar block adjustment in ten subareas. The unit is an NAC image pixel assumed to be 1.5 m.

Subarea ID	RMS Errors of Control Points (Pixel)			Maximum Errors of Control Points (Pixel)			RMS Errors of Tie Point (Pixel)			Maximum Errors of Tie Point (Pixel)		
	x	y	xy	x	y	xy	x	y	xy	x	y	xy
Part 1	13.10	19.41	23.42	1.71	38.42	38.46	0.33	0.48	0.58	0.33	-3.31	3.33
Part 2	19.18	21.75	29.00	27.49	-25.76	37.68	0.37	0.45	0.58	0.75	-2.84	2.93
Part 3	17.75	19.81	26.60	21.92	37.94	43.82	0.46	0.62	0.77	0.11	-2.83	2.83
Part 4	17.70	13.23	22.10	34.60	9.24	35.81	0.17	0.30	0.34	-0.33	1.43	1.47
Part 5	18.71	13.71	23.20	32.50	3.14	32.65	0.16	0.18	0.24	2.80	0.24	2.81
Part 6	17.08	13.04	21.49	17.07	-21.94	27.80	0.23	0.36	0.43	2.53	-0.26	2.54
Part 7	23.44	15.52	28.11	40.90	11.76	42.56	0.26	0.38	0.46	-1.85	1.10	2.15
Part 8	32.13	19.30	37.48	43.67	-35.92	56.54	0.41	0.43	0.59	-3.40	1.50	3.72
Part 9	36.41	8.10	37.30	40.78	-11.34	42.33	0.26	0.21	0.33	2.45	0.50	2.50
Part 10	19.37	15.39	24.74	36.83	-13.60	39.26	0.25	0.51	0.57	0.50	-2.75	2.80

After planar block adjustment, the DOMs of the NAC images were automatically generated via ortho-rectification. The block adjustment results can also be assessed by the geometric deviations between these DOMs. Figure 5 displays three examples of the positional deviations of two neighboring NAC DOMs before and after block adjustment. The upper three subfigures show parts of the DOMs rectified using the original RFMs, while the lower three are the DOMs produced from the same images but with the block adjustment–refined RFMs. The three groups of examples come from Part 1 ((a) and (d)), Part 5 ((b) and (e)), and Part 10 ((c) and (f)), respectively. It can be seen that in subfigures (a), (b), and (c) that there exist up to 100-m geometric deviations that are almost completely removed by the block adjustment as depicted in subfigures (e), (f), and (g).

Figure 6 compares the positional differences between NAC DOMs and SLDEM2015 before (subfigures (a), (b), and (c)) and after (subfigures (d), (e), and (f)) the planar block adjustment. The NAC DOMs in subfigures (a) and (d) are part of m1221740903r in Part 1, (b) and (e) are part of m1175809506l in Part 5, and (c) and (f) are part of m1145135367l in Part 10. It can be seen that the geometric differences before block adjustment are about two grid sizes of the SLDEM. After block adjustment processing, these deviations are almost completely corrected with the manually selected control points.

Seamless DOM mosaics were generated for each subarea via the process of planar block adjustment, image ortho-rectification, grayscale balancing, and final DOM mosaicking. The LROC WAC mosaic product was chosen as the reference for histogram matching–based grayscale balancing. Most of the time, the seam lines were automatically extracted. However,

if two adjacent images had obvious illumination difference, the seam lines would need some manual editing to guarantee natural transition of the grayscale.

### Overall Block Adjustment Evaluation

Although mapping with partitions is widely used when dealing with a large amount of data or large-area mapping, there is little research on the evaluation of the attainable accuracy between the overall block adjustment and the subareas block adjustment. In this article, we gave a specific analysis on this issue using LROC NAC images in our study area.

The block adjustment using the same control points and tie points of the subarea blocks was performed with all the images involved in the subarea block adjustment, the results of which are shown in Table 3. It demonstrates that the RMS errors of tie points can achieve subpixel-level accuracy in both subarea and overall block adjustment in our study case. But the maximum error of the tie points from the overall adjustment is almost twice the maximum errors from the subarea block adjustment. This indicates that a partition can improve the quality of DOM and mosaicking products. Both RMS and maximum errors show that the precision at control points decreased remarkably. This may be partially due to the insufficient precision of control points selected from a lower-resolution reference. To rectify the orbital images to the reference DEM for synergetic analysis of different data sets in further applications, the orbital images should be well coregistered to the reference DEM. In this perspective, the partition strategy for planar block adjustment is meaningful and effective.

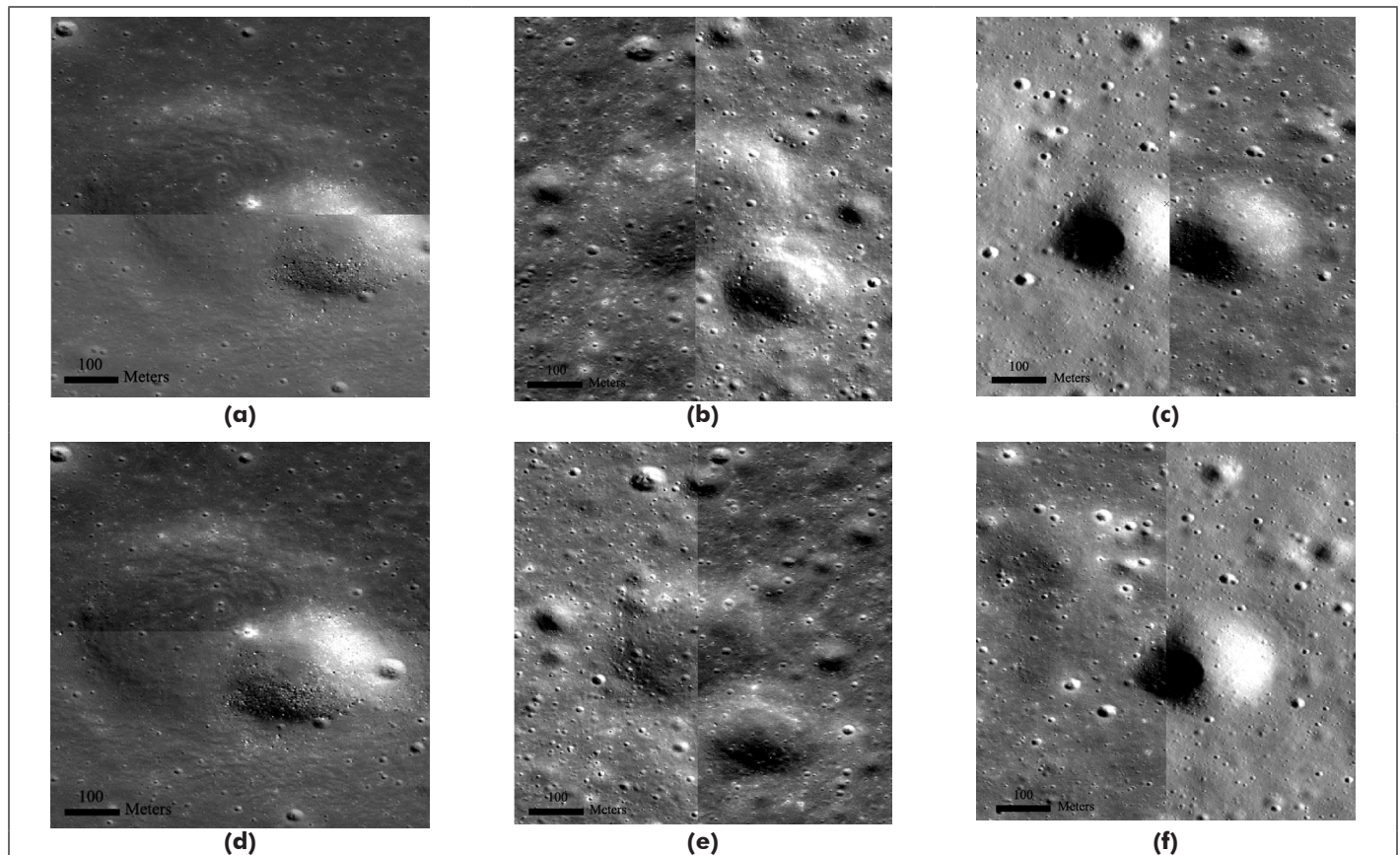


Figure 5. The geometric consistency comparisons between two neighboring DOMs. The upper three subfigures are the DOMs generated using original RFMs, and the lower three are the DOMs rectified by the planar block adjustment refined RFMs. Subfigures (a) and (d) are part of m1221740903r and m1191136940l in Part 1, (b) and (e) are part of m1208769920r and m1175809506l in Part 5, and (c) and (f) are part of m181502892le and m1145135367l in Part 10.

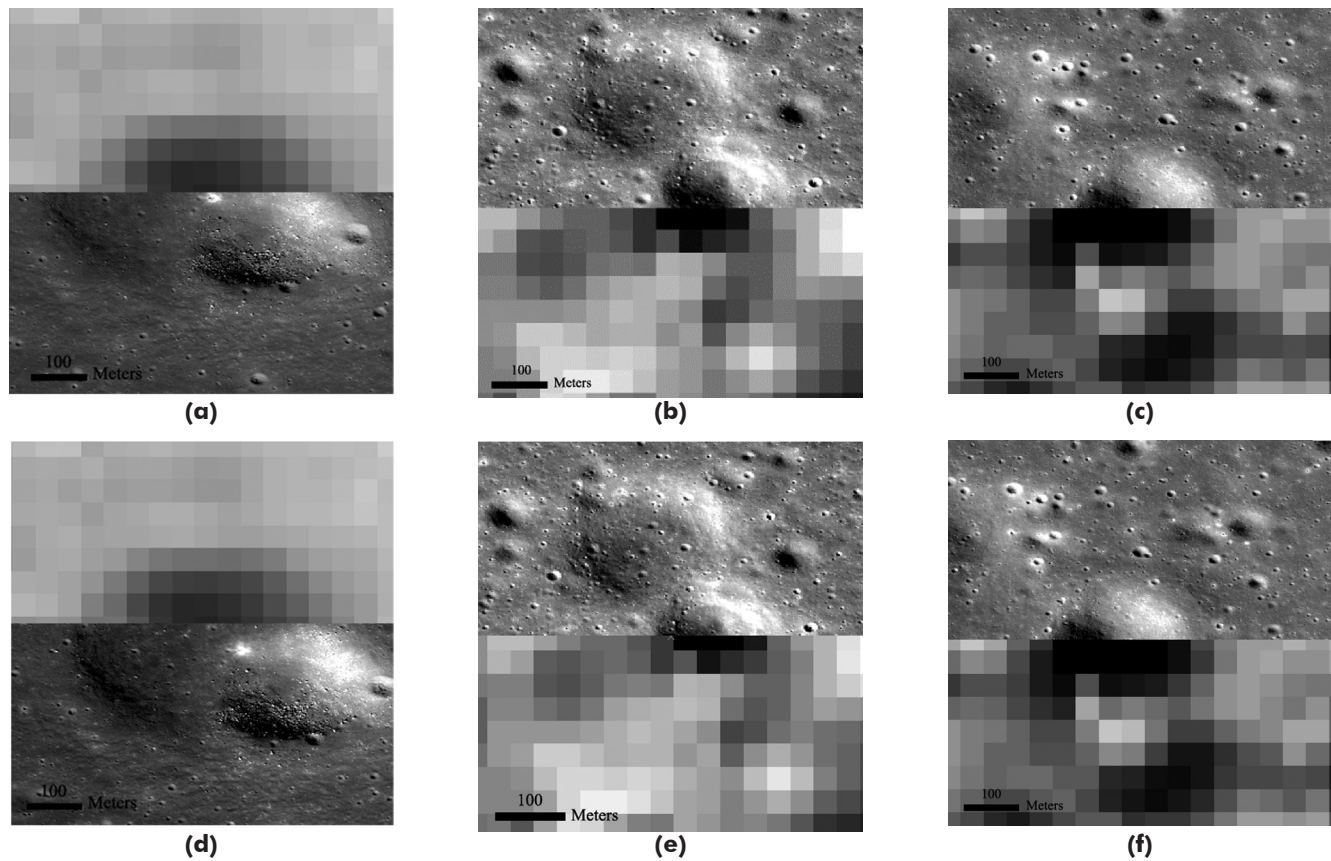


Figure 6. The geometric differences between NAC DOMs and SLDEM2015 before (upper three) and after (lower three) the planar block adjustment. The NAC DOMs in subfigures (a) and (d) are part of m1221740903r in Part 1, (b) and (e) are part of m1175809506l in Part 5, and (c) and (f) are part of m1145135367l in Part 10.

Table 3. Image numbers, control point, and tie point numbers and control point and tie point precisions of the overall block adjustment using all the selected NAC images involved in the subarea block adjustment. The unit for precision assessment is an NAC image pixel assumed to be 1.5 m.

Image Number	Control Point number	Tie Point Number	RMS Errors of Control Points (Pixel)			Maximum Errors of Control Points (Pixel)			RMS Errors of Tie Point (Pixel)			Maximum Errors of Tie Point (Pixel)		
			x	y	xy	x	y	xy	x	y	xy	x	y	xy
750	95	437 999	23.69	26.13	35.27	49.87	78.93	93.37	0.27	0.37	0.46	0.94	5.62	5.7

### TPS-Based DOM Registration Results

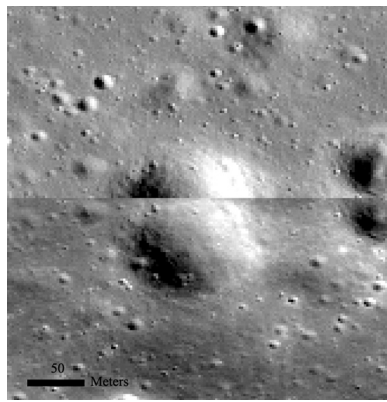
Due to the limited resolution of the SLDEM2015 compared with the LROC NAC images, geometric inconsistencies still exist between the seamlessly mosaicked adjacent subarea DOMs. The upper two subfigures in Figure 7 show examples of the geometric inconsistencies between Part 1 and 2 as well as Part 9 and 10 mosaicked DOMs, which were effectively reduced by the image registration process based on the TPS model as indicated in subfigures (c) and (d) in Figure 7. The registration was conducted subarea by subarea using the procedure detailed in the section “TPS-Based Large-Area Image Registration.” A quantitative evaluation of the registration results can also be realized by measuring the differences of the check point pair coordinates between any two overlapping subarea DOM mosaics. Parts 1 and 2 are taken as examples. Evenly distributed check point pairs were automatically matched in the overlapping region, as shown in Figure 8.

The deviations of the check point coordinates in the latitudinal and longitudinal directions are listed in Table 4. After the TPS-based registration, the planar deviations are reduced to about 1 pixel, and the largest difference is 2.69 m, which is no more than 2 pixels of the output DOM, reflecting a high-precision registration.

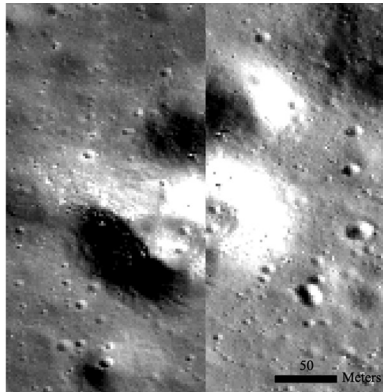
### Landing Area DOM and Potential Applications

After subarea planar block adjustment and TPS-based image registration of the subarea DOMs, a seamless DOM mosaic of the entire Chang’e-5 planned landing area was produced. The generated radiometrically homogeneous and geometrically seamless DOM mosaic is shown in Figure 9 (zoomed-out view). This final DOM mosaic has the image size of 224 721 columns and 44 945 rows with a ground sample distance of 1.5 m.

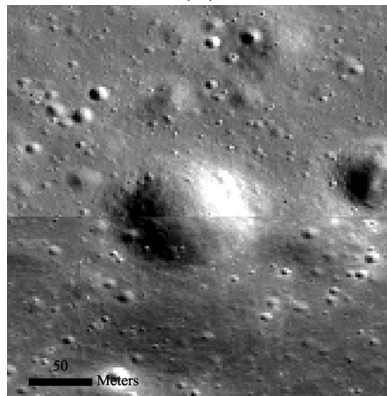
This high-resolution 10-gigapixel DOM has many potential applications for detailed morphological and geological studies. For example, using the high-resolution map, craters can be precisely measured to determine the age of surface units (Michael and Neukum 2010); small, particularly fresh craters (e.g., flat-bottomed, central-mound, and concentric craters) can be used to estimate the depth of the lunar regolith (Bart *et al.* 2011; Di *et al.* 2016); rocks/boulders on the ejecta of a crater can be identified and the spatial density used to estimate the formation time of the crater (Li *et al.* 2017); and so on. More important, distribution pattern analyses of crater rays, crater chains, and boulders are significant in helping identify source locations of the exposed features (e.g., rock and soil samples to be collected by the lander), which will directly contribute to the major scientific objective of the sample return mission.



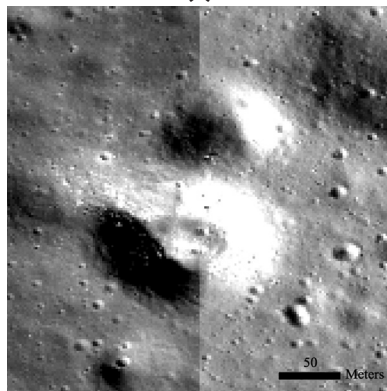
(a)



(b)



(c)



(d)

Figure 7. The positional difference comparisons between two neighboring subarea DOMs before (upper two) and after (lower two) the image registration process based on the TPS model. Subfigures (a) and (c) are from the overlapping area of Parts 1 and 2, and (b) and (d) are from the overlapping area of Parts 9 and 10.

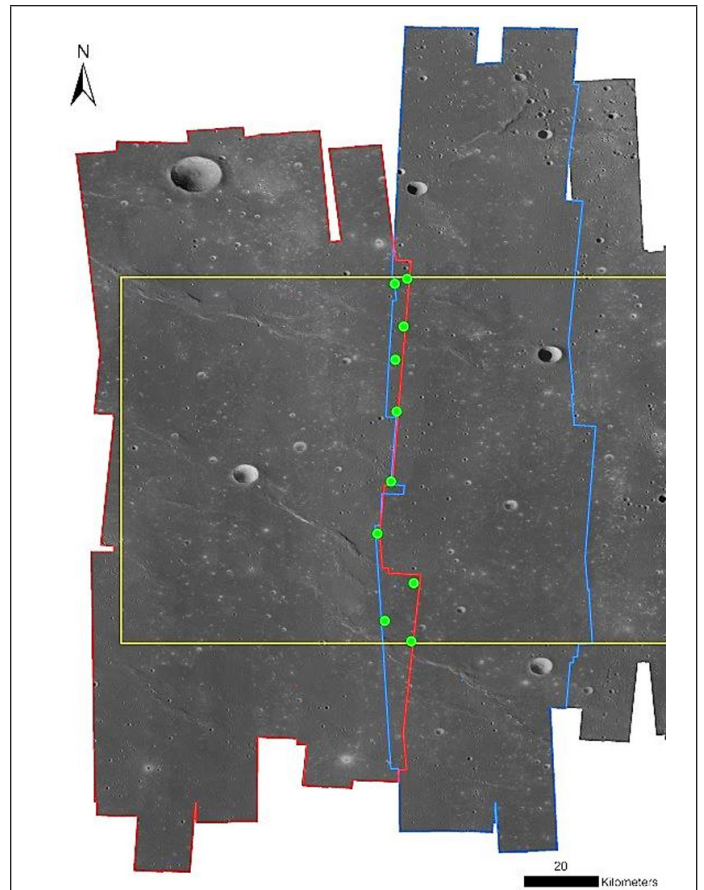


Figure 8. Check points (green circles) between Parts 1 and 2 subarea DOM mosaics for precision evaluation of the TPS-based image registration. The red polygon is the border of Part 1, the blue polygon is the border of Part 2, and the yellow rectangle shows part of the planned landing area of Chang'e-5.

Table 4. TPS-based DOM registration precision between Part 1 and Part 2 subarea DOM mosaics (1.5 m/pixel). “Lat Diff” and “Long Diff” represent the coordinate differences in latitude and longitude directions, respectively; “chk” represents check point.

Chk ID	Before DOM Registration (m)			After DOM Registration (m)		
	Long Diff	Lat Diff	Planar Diff	Long Diff	Lat Diff	Planar Diff
chk1	4.69	-14.30	15.05	1.62	-1.26	2.05
chk2	15.72	-15.87	22.34	0.42	-0.61	0.74
chk3	-11.05	-21.96	24.58	0.96	-0.56	1.11
chk4	11.68	-16.57	20.27	-1.58	-2.17	2.69
chk5	-4.29	17.76	18.27	1.13	0.79	1.38
chk6	4.56	24.05	24.48	0.00	-1.20	1.20
chk7	-10.15	29.91	31.58	0.22	0.39	0.45
chk8	6.08	32.38	32.94	0.66	0.37	0.75
chk9	15.63	10.85	19.02	-0.37	1.26	1.32
chk10	6.08	-9.95	11.66	-0.78	0.42	0.88

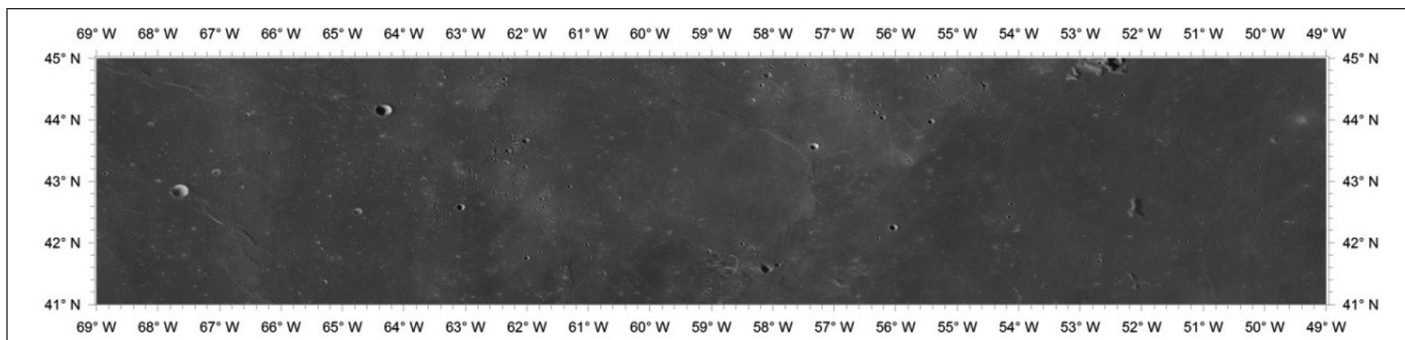


Figure 9. Produced seamless DOM mosaic of the Chang'e-5 planned landing area.

## Conclusions

To solve the problems of large-area controlled seamless DOM production using LROC NAC images, a systematic method consisting of two stages of data processing is developed in this study. First, the RFM-based planar block adjustment is used to improve the relative positional consistencies of the LROC NAC images to the subpixel level and at the same time tie the NAC images to the control source (SLDEM2015). Second, a TPS-based image registration is used to reduce the geometric inconsistencies between two neighboring subarea DOM mosaics and ensures final DOM being seamlessly mosaicked throughout the entire area.

A high-resolution seamless DOM mosaic is produced with the proposed two-stage method for the Chang'e-5 planned landing area using 765 NAC images. Consequently, the tie point RMS errors are all approximately one-half pixel, showing satisfactory geometric consistencies among NAC images. The control point RMS errors were approximately one grid cell size of SLDEM2015, which means that the produced DOM has been registered to SLDEM2015 with high precision. After DOM registration with the TPS model, the planar precision is mostly smaller than one pixel in the output DOM. The resultant DOM mosaic, covering 49°–69° west longitude and 41°–45° north latitude, has an image size of 224 721 columns  $\times$  44 945 rows with a ground sample distance of 1.5 m. This high-resolution DOM is of great importance for detailed morphological and geological analysis of the Chang'e-5 landing area. The developed method is applicable to high-resolution mapping of other large areas on the lunar surface using LROC NAC images.

## Acknowledgments

This work was supported by the Key Research Program of the Chinese Academy of Sciences (grant no. XDPB11) and the National Natural Science Foundation of China (grant nos. 41671458, 41590851, and 41771490). We thank all those who worked on the Planetary Data System archive to make the LRO imagery and SLDEM2015 publicly available.

## References

Archinal B. A., E. Lee, L. Weller, J. Richie, K. Edmundson, M. Robinson, E. Speyerer, A. K. Boyd, E. Bowman-Cisneros, R. Wagner and A. V. Nefian. 2015. Status of geodetically controlled high-resolution LROC polar mosaics. Page 1571 in *Proceedings of 46th Lunar and Planetary Science Conference*, held in The Woodlands, Tex., 16–20 March 2015.

Arizona State University. 2011. WAC Global Morphologic Map. <[http://wms.lroc.asu.edu/lroc/view\\_rdr/WAC\\_GLOBAL](http://wms.lroc.asu.edu/lroc/view_rdr/WAC_GLOBAL)> Accessed 10 April 2018.

Barker, M. K., E. Mazarico, G. A. Neumann, M. T. Zuber, J. Haruyama and D. E. Smith. 2016. A new lunar digital elevation model from the Lunar Orbiter Laser Altimeter and SELENE Terrain Camera. *Icarus* 273:346–355.

Bart, G. D., R. D. Nickerson, M. T. Lawder and J. Melosh. 2011. Global survey of lunar regolith thickness from LROC images. *Icarus* 215(2):485–490.

Burns, K. N., E. J. Speyerer, M. S. Robinson, T. Tran, M. R. Rosiek, B. A. Archinal and E. Howington-Kraus. 2012. Digital elevation models and derived products from LROC NAC stereo observations. Pages 483–488 in *Proceedings of 22nd Congress of International Archives of the Photogrammetry, Remote Sensing and Spatial Information Sciences—ISPRS Archives*, held in Melbourne, Australia, 25 August–1 September 2012.

Data Publishing and Information Service System of China' Lunar Exploration Project. 2018. <[http://moon.bao.ac.cn/searchOrder\\_dataSearch.search](http://moon.bao.ac.cn/searchOrder_dataSearch.search)> Accessed 2 July 2018.

Di, K., M. Jia, X. Xin, B. Liu, Z. Liu, M. Peng and Z. Yue. 2018. High resolution seamless DOM generation over Chang'e-5 landing area using LROC NAC images. Pages 271–276 in *Proceedings of 2018 ISPRS TC III Mid-term Symposium "Developments, Technologies and Applications in Remote Sensing,"* held in Beijing, China, 7–10 May.

Di, K., Y. Liu, B. Liu, M. Peng and W. Hu. 2014. A self-calibration bundle adjustment method for photogrammetric processing of Chang'e-2 stereo lunar imagery. *IEEE Transactions on Geoscience and Remote Sensing* 52(9):5432–5442.

Di, K., S. Sun, Z. Yue and B. Liu. 2016. Lunar regolith thickness determination from 3D morphology of small fresh craters. *Icarus* 267:12–23.

Gbtimes. 2017. China confirms landing site for Chang'e-5 Moon sample return. <<https://gbtimes.com/china-confirms-landing-site-change-5-moon-sample-return>> Accessed 10 April 2018.

Gwinner, K., R. Jaumann, E. Hauber, H. Hoffman, C. Heipke, J. Oberst, G. Neukum, V. Ansan, J. Bostelmann, A. Dumke, S. Elgner, G. Erkeling, F. Fueten, H. Hiesinger, N. M. Hoekzema, E. Kersten, D. Loizeau, K.-D. Matz, P. C. McGuire, V. Mertens, G. Michael, A. Pasewaldt, P. Pinet, F. Preusker, D. Reiss, T. Roatsch, R. Schmidt, F. Scholten, M. Spiegel, R. Stesky, D. Tirsh, S. van Gasselt, S. Walter, M. Wählisch and K. Willner. 2016. The high resolution stereo camera (HRSC) of Mars Express and its approach to science analysis and mapping for Mars and its satellites. *Planetary and Space Science* 126:93–138.

Gwinner, K., F. Scholten, F. Preusker, S. Elgner, T. Roatsch, M. Spiegel, R. Schmidt, J. Oberst, R. Jaumann and C. Heipke. 2010. Topography of Mars from global mapping by HRSC high-resolution digital terrain models and orthoimages: Characteristics and performance. *Earth and Planetary Science Letters* 294(3):506–519.

Haase, I., J. Oberst, F. Scholten, M. Wählisch, P. Gläser, I. Karachevtseva and M. S. Robinson. 2012. Mapping the Apollo 17 landing site area based on Lunar Reconnaissance Orbiter Camera images and Apollo surface photography. *Journal of Geophysical Research: Planets* 117(E00H20):1–8.

Haase, I., M. Wählisch, P. Gläser, J. Oberst and M. S. Robinson. 2014. Apollo 17 landing site: A cartographic investigation of the Taurus-Littrow Valley based on LROC NAC imagery. Pages 1–12 in *Proceedings of European Planetary Science Congress*, held in Cascais, Portugal 7–12 September 2014.

- Henriksen, M. R., M. R. Manheim, K. N. Burns, P. Seymour, E. J. Speyerer, A. Deran, A. K. Boyd, E. Howington-Kraus, M. R. Rosiek, B. A. Archinal and M. S. Robinson. 2016. Extracting accurate and precise topography from LROC narrow angle camera stereo observations. *Icarus* 283:122–137.
- Klem, S. M., M. R. Henriksen, J. Stopar, A. Boyd and M. S. Robinson. 2014. Controlled LROC narrow angle camera high resolution mosaics. Page 2885 in *Proceedings of 45th Lunar and Planetary Science Conference*, held in The Woodlands, Tex., 17–21 March 2014.
- Kokhanov, A. A., I. P. Karachevtseva, A. E. Zubarev, V. Patraty, Z. F. Rodionova and J. Oberst. 2017. Mapping of potential lunar landing areas using LRO and SELENE data. *Planetary and Space Science*, in press. <<https://doi.org/10.1016/j.pss.2017.08.002>>
- Lee, E. M., L. A. Weller, J. O. Richie, B. L. Redding, J. R. Shinaman, K. Edmundson, B. A. Archinal, T. M. Hare and R. L. Fergason. 2012. Controlled polar mosaics of the Moon for LMMP by USGS. Page 2507 in *Proceedings of 43rd Lunar and Planetary Science Conference*, held in The Woodlands, Tex., 19–23 March 2012.
- Li, C. L., J. J. Liu, X. Ren, L. L. Mous, Y. L. Zou, H. B. Zhang, C. Lü, J. Z. Liu, W. Zuo, Y. Su, W. B. Wen, W. Bian, B. C. Zhao, J. F. Yang, X. D. Zou, M. Wang, C. Xu, D. Q. Kong, X. Q. Wang, F. Wang, L. Geng, Z. B. Zhang, L. Zheng, X. Y. Zhu, J. D. Li and Z. Y. Ouyang. 2010. The global image of the Moon obtained by the Chang' E-1: Data processing and lunar cartography. *Science China: Earth Science*. 53(8):1091–1102.
- Li, C., X. Ren, J. Liu, F. Wang, W. Wang, W. Yan and G. Zhang. 2015. A new global and high resolution topographic map product of the Moon from Chang'e-2 image data. Page 1638 in *Proceedings of 46th Lunar and Planetary Science Conference*, held in The Woodlands, Tex., 16–20 March 2015.
- Li, Y., A. T. Basilevsky, M. Xie and W.-H. Ip. 2017. Correlations between ejecta boulder spatial density of small lunar craters and the crater age. *Planetary and Space Science*, in press. <<https://doi.org/10.1016/j.pss.2017.08.007>>
- Liu, B., M. Jia, K. Di, J. Oberst, B. Xu and W. Wan. 2017. Geopositioning precision analysis of multiple image triangulation using LROC NAC lunar images. *Planetary and Space Science*, in press. <<https://doi.org/10.1016/j.pss.2017.07.016>>
- Liu, B., B. Xu, K. C. Di and M. N. Jia. 2016. A solution to low fitting precision of planetary orbiter images caused by exposure time changing. Pages 441–448 in *Proceedings of 23rd ISPRS Congress, Commission IV*, held in Prague, Czech Republic, 12–19 July 2016.
- Michael, G. G. and G. Neukum. 2010. Planetary surface dating from crater size–frequency distribution measurements: Partial resurfacing events and statistical age uncertainty. *Earth and Planetary Science Letters* 294(3–4):223–229.
- Mazarico, E., D. D. Rowlands, G. A. Neumann, D. E. Smith, M. H. Torrence, F. G. Lemoine and M. T. Zuber. 2012. Orbit determination of the Lunar Reconnaissance Orbiter. *Journal of Geodesy* 86 (3):193–207.
- Moratto, Z. M., M. J. Broxton, R. A. Beyer, M. Lundy and K. Husmann. 2010. Ames Stereo Pipeline, NASA's open source automated stereogrammetry software. Page 2364 in *Proceedings of 41st Lunar and Planetary Science Conference*, held in The Woodlands, Tex., 1–5 March 2010.
- NAIF. 2014. Lunar Reconnaissance Orbiter Camera (LROC) Instrument Kernel v18. <[http://naif.jpl.nasa.gov/pub/naif/pds/data/lro-l-spice-6-v1.0/lrosp\\_1000](http://naif.jpl.nasa.gov/pub/naif/pds/data/lro-l-spice-6-v1.0/lrosp_1000)>. Accessed 10 April 2018.
- National Aeronautics and Space Administration. 2011. LRO Camera Team Release High Resolution Global Topographic Map of Moon. <[http://www.nasa.gov/mission\\_pages/LRO/news/lro-topo.html](http://www.nasa.gov/mission_pages/LRO/news/lro-topo.html)>. Accessed 10 April 2018.
- National Aeronautics and Space Administration, Goddard Space Flight Center, and Arizona State University. 2014. 681 Gigapixels. <<http://lroc.sese.asu.edu/posts/738>>. Accessed 10 April 2018.
- Ouyang, Z., Y. Zou and C. Li. 2004. The scientific objectives of Chinese First Lunar Exploration Project. *Science and Technology*. 1–2.
- Planetary Data System. 2014. Processing of Lunar Reconnaissance Orbiter Camera Narrow Angle Camera Image Frames with ISIS 3. <[https://pds-imaging.jpl.nasa.gov/documentation/LROC\\_NAC\\_CreateCDRs\\_w\\_ISIS\\_Feb14.pdf](https://pds-imaging.jpl.nasa.gov/documentation/LROC_NAC_CreateCDRs_w_ISIS_Feb14.pdf)>. Accessed 10 April 2018.
- Preusker, F., A. Stark, J. Oberst, K.-D. Matz, K. Gwinner, T. Roatsch and T. R. Watters. 2017. Toward high-resolution global topography of Mercury from MESSENGER orbital stereo imaging: A prototype model for the H6 (Kuiper) Quadrangle. *Planetary and Space Science*. 142:26–37.
- Robinson, M. S., S. M. Brylow, M. Tschimmel. 2010. Lunar Reconnaissance Orbiter Camera (LROC) instrument overview. *Space Science Review* 150(1–4):81–124.
- Robinson, M. S., A. S. McEwen, E. Eliason, E. M. Lee, E. Malaret and P. G. Lucey. 1999. Clementine UVVIS global mosaic: A new tool for understanding the lunar crust. Page 1931 in *Proceedings of 30th Lunar and Planetary Science Conference*, held in The Woodlands, Tex., 14–19 March 1999.
- Shen, X., B. Liu and Q. Q. Li. 2017. Correcting bias in the rational polynomial coefficients of satellite imagery using thin-plate smoothing splines. *ISPRS Journal of Photogrammetry and Remote Sensing* 125:125–131.
- Tran, T., M. R. Rosiek, R. A. Beyer, S. Mattson, E. Howington-Kraus, M. Robinson, B. A. Archinal, K. Edmundson, D. Harbour and E. Anderson. 2010. Generating digital terrain models using LROC NAC images. Pages 1-7 in *Proceedings of ASPRS/CaGIS 2010 Fall Specialty Conference*, held in Orlando, Fla., 15–19 November 2010.
- Wagner, R. V., M. S. Robinson and LROC Team. 2016. Design and processing of the Lunar North Pole Mosaic. Page 1582 in *Proceedings of 47th Lunar and Planetary Science Conference*, held in The Woodlands, Tex., 21–25 March 2016.
- Wagner, R. V., E. J. Speyerer, M. S. Robinson and LROC Team. 2015. New mosaicked data products from the LROC team. Page 1473 in *Proceedings of 46th Lunar and Planetary Science Conference*, held in The Woodlands, Tex., 16–20 March 2015.
- Wahba, G. 1990. *Spline Models for Observational Data*. Philadelphia: Society for Industrial and Applied Mathematics.
- Wu, B., F. Li, L. Ye, S. Qiao, J. Huang, X. Wu and H. Zhang. 2014. Topographic modeling and analysis of the landing site of Chang'e-3 on the Moon. *Earth and Planetary Science Letters* 405:257–273.
- Wu, B. and W. C. Liu. 2017. Calibration of boresight offset of LROC NAC imagery for precision lunar topographic mapping. *ISPRS Journal of Photogrammetry and Remote Sensing* 128:372–387.
- Wu B., H. Zeng and H. Hu. 2018. Illumination invariant feature point matching for high-resolution planetary remote sensing images. *Planetary and Space Science* 152:45–54.
- Yue, Z., G. G. Michael, K. Di and J. Liu. 2017. Global survey of lunar wrinkle ridge formation times. *Earth and Planetary Science Letters* 477:14–20.
- Zhang, F., M. H. Zhu and Y. L. Zou. 2016. Late stage Imbrium volcanism on the Moon: Evidence for two source regions and implications for the thermal history of Mare Imbrium. *Earth and Planetary Science Letters* 445:13–27.

# SUSTAINING MEMBERS

## **ACI USA Inc.**

Weston, Florida  
acicorporation.com  
Member Since: 1/2018

## **Airbus Defense and Space**

Chantilly, Virginia  
www.intelligence-airbusds.com  
Member Since: 6/2016

## **Axis GeoSpatial, LLC**

Easton, Maryland  
www.axisgeospatial.com  
Member Since: 10/2002

## **Ayres Associates, Inc.**

Madison, Wisconsin  
www.AyresAssociates.com  
Member Since: 1/1953

## **Bohannon Huston, Inc.**

Albuquerque, New Mexico  
www.bhinc.com  
Member Since: 11/1992

## **Cardinal Systems, LLC**

Flagler Beach, Florida  
www.cardinalsystems.net  
Member Since: 1/2001

## **CompassData, Inc.**

Centennial, Colorado  
www.compassdatainc.com  
Member Since: 1/2012

## **DAT/EM Systems International**

Anchorage, Alaska  
www.datem.com  
Member Since: 1/1974

## **Dewberry**

Fairfax, Virginia  
www.dewberry.com  
Member Since: 1/1985

## **DigitalGlobe, Inc.**

Longmont, Colorado  
www.digitalglobe.com  
Member Since: 6/1996

## **Environmental Research Incorporated**

Linden, Virginia  
www.eri.us.com  
Member Since: 8/2008

## **Esri**

Redlands, California  
www.esri.com  
Member Since: 1/1987

## **GeoBC**

Victoria, Canada  
www.geobc.gov.bc.ca  
Member Since: 12/2008

## **GeoCue Group**

Madison, Alabama  
info@geocue.com  
Member Since: 10/2003

## **Geojano**

Pleasanton, California  
https://geojango.com/  
Member Since: 05-2019

## **Geomni, Inc.**

Lehi, Utah  
Geomni.net/psm  
Member Since: 03/2018

## **GeoWing Mapping Inc.**

Oakland, California  
www.geowingmapping.com  
Member Since: 1/2017

## **Global Science & Technology, Inc.**

Greenbelt, Maryland  
www.gst.com  
Member Since: 10/2010

## **GPI Geospatial Inc.**

formerly Aerial Cartographics of America, Inc. (ACA)  
Orlando, Florida  
www.aca-net.com  
Member Since: 10/1994

## **Harris Corporation**

Broomfield, Colorado  
www.harris.com  
Member Since: 6/2008

## **Keystone Aerial Surveys, Inc.**

Philadelphia, Pennsylvania  
www.keystoneaerialsurveys.com  
Member Since: 1/1985

## **Kucera International**

Willoughby, Ohio  
www.kucerainternational.com  
Member Since: 1/1992

## **Lead'Air, Inc.**

Kissimmee, Florida  
www.trackair.com  
Member Since: 5/2001

## **Martinez Geospatial, Inc. (MTZ)**

Eagan, Minnesota  
www.mtzgeo.com  
Member Since: 1/1979

## **MDA Information Systems LLC**

Gaithersburg, Maryland  
www.mdaus.com  
Member Since: 1/1983

## **Merrick & Company**

Greenwood Village, Colorado  
www.merrick.com/gis  
Member Since: 4/1995

## **Observera, Inc.**

Chantilly, Virginia  
www.observera.com  
Member Since: 8/2002

## **PCI Geomatics**

Richmond Hill, Ontario, Canada  
www.pcigeomatics.com  
Member Since: 1/1989

## **Pickett and Associates, Inc.**

Bartow, Florida  
www.pickettusa.com  
Member Since: 4/2007

## **PixElement**

Columbus, Ohio  
www.pixelement.com  
Member Since: 1/2017

## **Quantum Spatial, Inc.**

Sheboygan Falls, Wisconsin  
www.quantumspatial.com  
Member Since 1/1974

## **Riegl USA, Inc.**

Orlando, Florida  
www.rieglusa.com  
Member Since: 11/2004

## **Robinson Aerial Survey, Inc. (RAS)**

Hackettstown, New Jersey  
www.robinsonaerial.com  
Member Since: 1/1954

## **Routescene, Inc.**

Durango, Colorado  
www.routescene.com/  
Member Since: 12/2007

## **Sanborn Map Company**

Colorado Springs, Colorado  
www.sanborn.com  
Member Since: 10/1984

## **Teledyne Optech**

Toronto, Canada  
www.teledyneoptech.com  
Member Since: 1/1999

## **Terra Remote Sensing (USA) Inc.**

Bellevue, Washington  
www.terrareMOTE.com  
Member Since: 10/2016

## **The Airborne Sensing Corporation**

Toronto, Canada  
www.airsensing.com  
Member Since: 7/2003

## **Towill, Inc.**

San Francisco, California  
www.towill.com  
Member Since: 1/1952

## **University of Twente/Faculty ITC**

Enschede, Netherlands  
www.itc.nl  
Member Since: 1/1992

## **U.S. Geological Survey**

Reston, Virginia  
www.usgs.gov  
Member Since: 4/2002

## **Woolpert LLP**

Dayton, Ohio  
www.woolpert.com  
Member Since: 1/1985

# Occlusion Probability in Operational Forest Inventory Field Sampling with ForeStereo

F. Montes, A. Rubio-Cuadrado, M. Sánchez-González, I. Aulló-Maestro, M. Cabrera, and C. Gómez

## Abstract

Field data in forest inventories are increasingly obtained using proximal sensing technologies, often under fixed-point sampling. Under fixed-point sampling some trees are not detected due to instrument bias and occlusions, hence involving an underestimation of the number of trees per hectare ( $N$ ). The aim here is to evaluate various approaches to correct tree occlusions and instrument bias estimates calculated with data from ForeStereo (proximal sensor based on stereoscopic hemispherical images) under a fixed-point sampling strategy. Distance-sampling and the new hemispherical photogrammetric correction (HPC), which combines image segmentation-based correction for instrument bias with a novel approach for estimating the proportion of shadowed sampling area in stereoscopic hemispherical images, best estimated  $N$  and basal area (BA). Distance-sampling slightly overestimated  $N$  (11% bias, 0.60 Pearson coefficient with the reference measures) and BA (4%, 0.82). HPC provided less biased  $N$  estimates (-6%, 0.61) but underestimated BA (-8%, 0.83). HPC most accurately retrieved the diameter distribution.

## Introduction

Understanding forests dynamics is necessary for sustainable forest management. Forest inventories supported by data measured on the ground and data acquired remotely via aerial or satellite platforms enable the monitoring of forest structure, growth, change in composition, responses to silvicultural traits, and decline originated by climatic or biotic factors. Continuous development of technology for data acquisition, processing, and analysis contributes to improving the quality of forest inventories. Remote sensing provides information on forest variables such as cover (Morsdorf *et al.* 2006), structure (Gómez *et al.* 2011), volume (Vauhkonen *et al.* 2011), or biomass (Næsset and Gobakken 2008), with complete spatial coverage. A wide range of sensors with different spatial resolutions (from hundreds to less than 1 m) are suitable for forest applications (White *et al.* 2016). Satellite imagery and aerial Light Detection and Ranging (LiDAR) data support mapping and updating National Forest Inventory estimations (e.g. in Finland, (Tomppo *et al.* 2008) or in Canada (Hilker *et al.* 2008)). Changes in land cover and forest variables like biomass are mapped and monitored with optical and radar satellite sensors (White *et al.* 2017; Matasci *et al.* 2018; Santoro *et al.* 2018). For height retrieval and assessment of vertical structure, Synthetic Aperture Radar may be employed by itself (e.g. Garestier *et al.* 2008; Tebaldini and Rocca 2012) and its

Fernando Montes, Mariola Sánchez-González, Isabel Aulló-Maestro, and Cristina Gómez are with INIA-CIFOR, Ctra. de la Coruña km 7.5, 28040 Madrid, Spain (fmontes@inia.es).

Álvaro Rubio-Cuadrado is with the Departamento de Sistemas y Recursos Naturales, Escuela Técnica Superior de Ingeniería de Montes, Forestal y del Medio Natural, Universidad Politécnica de Madrid, Ciudad Universitaria, 28040, Madrid, Spain.

Miguel Cabrera is with Aranzada Gestión Forestal, C/Alonso Heredia 31, 28028, Madrid, Spain.

combination with LiDAR data is expected to provide improved resolution and accuracy for large scale assessments (Qi *et al.* 2019). For estimation of forest inventory variables at regional scale LiDAR is the most precise technology (Wulder *et al.* 2013) enabling structural characterization (Valbuena *et al.* 2013; Bottalico *et al.* 2017) and measurement of individual tree attributes (Hauglin *et al.* 2014). LiDAR provides precise digital elevation models and metrics for characterization of height distribution (Lindberg *et al.* 2012) and is increasingly being used to generalize the sampling plot data to the whole area through area-based models (Næsset 2002; Bouvier *et al.* 2015). Research is ongoing to overcome LiDAR limitations in the estimation of tree diameter distribution (Magnussen *et al.* 2013) or species composition (Maltamo *et al.* 2009), which may benefit from the combination with other sensors (Holmgren *et al.* 2008; Puttonen *et al.* 2010; Zhao *et al.* 2018). Forest canopy surface height can also be estimated comparing image-based point clouds derived from digital aerial photography and terrain elevation models of high spatial resolution generated with LiDAR (Leberl *et al.* 2010). Digital aerial photography is less costly than LiDAR (White *et al.* 2013) and provide spectral information to support species classification (St-Onge *et al.* 2015); however, image-based point clouds do not penetrate through tree crowns in dense stands (White *et al.* 2013) being LiDAR more informative for forest inventory applications. Equipped with optical sensors unmanned aerial vehicles (UAVs) can retrieve photogrammetric surface models at local scale with very high spatial resolution, and spectral vegetation indices to support species classification (Tuominen *et al.* 2018). To date, practical concerns in the use of UAVs include data processing, power autonomy, payload weight, and local regulations (Gómez and Green, 2017; Manfreda *et al.* 2018).

Although the contribution of remotely sensed data to forest inventories is constantly increasing, field data is needed to calibrate and validate the models (Brososke *et al.* 2014). Field data is expensive to acquire, therefore, a sampling survey approach is generally used (Mandallaz and Ye 1999). Proximal Sensing (PS) techniques, which refer to the acquisition of data with a sensor from a relatively short distance, may provide information on variables which are complex to measure manually, such as spatial arrangement and dimensions of trees (Rodríguez-García *et al.* 2014), canopy features (Seidel *et al.* 2012), stand volume (Astrup *et al.* 2014), or forest fuel (Pimont *et al.* 2015), complementing the field measurement and enhancing performance (Dassot *et al.* 2011). The combination of remote sensing and proximal sensing may improve estimations and reduce the cost of inventories (Lindberg *et al.* 2012).

The development of point sampling PS technologies—based on laser distance or photogrammetry—to measure tree dimensions and to estimate forest parameters at plot or stand level began in the early 2000s (Clark *et al.* 2000; Lovell *et al.*

Photogrammetric Engineering & Remote Sensing  
Vol. 85, No. 7, July 2019, pp. 493–508.  
0099-1112/19/493–508

© 2019 American Society for Photogrammetry  
and Remote Sensing  
doi: 10.14358/PERS.85.7.493

2003). Some PS technologies have been optimized for forestry, such as ForeStereo (a camera system with fish-eye lenses (Montes *et al.* 2009)) and Terrestrial Laser Scanning (TLS) (Liang *et al.* 2016; Newnham *et al.* 2015).

ForeStereo is a passive optical sensor composed of two hemispherical cameras capturing the visible radiation reflected by the surface of surrounding objects (e.g. trees) in a single shot. The stereoscopic hemispherical images were firstly used for measurement of tree diameter, height, and volume by Rodríguez-García *et al.* (2014). ForeStereo technology has been incorporated into the Spanish National Forest Inventory (Sánchez González *et al.* 2016) and National Parks forest monitoring in Spain (Sangüesa-Barreda *et al.* 2015; Rubio-Cuadrado *et al.* 2018a; Rubio-Cuadrado *et al.* 2018b). ForeStereo is widely used as part of the field survey in natural forests and plantations of different species in Spain and it is being tested in Brazil and Chile. Computer vision techniques have been developed for the segmentation of ForeStereo images to identify trees (Sánchez-González *et al.* 2016) and a methodology has been proposed for the three-dimensional (3D) reconstruction of stem profiles from the angular disparity between the matched stem sections in both stereoscopic images and epipolarity restrictions (Rodríguez-García *et al.* 2014). ForeStereo has been specifically developed for forestry and employs software designed specifically to estimate stand variables such as basal area (BA) or number of trees per hectare (N) (Sánchez-González *et al.* 2016). Applications for vertical distribution of forest fuel assessment (Marino *et al.* 2018) or species classification (Gea-Izquierdo *et al.* 2015) have also been developed.

Terrestrial Laser Scanner used in forest inventories provides a dense point cloud that enables the 3D structural reconstruction (Strahler *et al.* 2008; Yao *et al.* 2011) and estimation of forest inventory variables such as N, BA, volume or biomass (Lovell *et al.* 2011; Astrup *et al.* 2014; Liang *et al.* 2016). TLS provides detailed data of below-canopy forest structure that can be used for precise biomass estimations and development of allometric equations, as well as crown shape and tree morphology modelling (Côte *et al.* 2012; Raunonen *et al.* 2013; Hauglin *et al.* 2013). However, the big amount of beam returns generated by TLS requires complex data processing to select returns from stems, foliage or shrubs and to fit geometrical models for diameter and volume estimation (Newnham *et al.* 2015). In addition, TLS devices are expensive and its use for the field stage in large scale forest inventories usually is not justified (White *et al.* 2016). Modern TLS devices reduce weight, and two-dimensional (2D) laser scanner offers an easy to handle solution, but data is limited to the sensors plane (Ringdahl *et al.* 2013; Brunner and Gizachew 2014). Compared with TLS, photogrammetric PS techniques (including ForeStereo) have better battery performance and reduced device weight, and faster image processing through computer vision techniques (Herrera *et al.* 2009; Herrera *et al.* 2011). Photogrammetric PS technologies employing conventional lenses require multiple image acquisitions (Clark *et al.* 2000; Varjo *et al.* 2006; Forsman *et al.* 2012), and processing becomes complicated. ForeStereo employs fisheye lenses with 180° field of view, so all features above the horizontal plane passing through the lens are projected in the image, enabling the 3D forest structural reconstruction around the sampling point from a single pair of images.

Large-scale operational forest inventories require a large number of sampling points covering the target area, therefore single scan plots are an economically advantageous option (Ducey *et al.* 2014). In order to become functional, a PS instrument for use in operational forest inventories should provide repeatable measures of the forest variables in a fast and economic manner, as well as a measure of the accuracy and reliability of the acquired data. For estimation of stand level

variables like BA or N, the fixed-point techniques are based on the angle count sampling method, which is the basis of the Relaskop (Bitterlich 1947). In the angle count sampling method, those stems projected in the visor which are wider than a reference threshold are sampled, so the maximum distance of detection depends on the size of each tree. Fixed point sampling typically underestimates the number of trees for two main reasons: (1) the instrument bias derived from a limited range of detection, which depends on the resolution of the scan or image and the diameter of trees (Seidel and Ammer 2014) and (2) the process of tree retrieval from a single scan or image: some trees actually present in the plot are occluded by others, hence reducing the tree detection rate (Lovell *et al.* 2011). The underestimation issue becomes more important in very dense forests and has been analyzed in recent studies (Yang *et al.* 2013; Brunner and Gizachew 2014). Three main methods have been proposed to correct the effects of tree occlusion on the estimation of plot and stand level variables, leading to less biased estimations:

- i) Attenuation model (Strahler *et al.* 2008). This method assumes that the gap probability—where a gap is the area between trees that allows clear visibility to more distant trees—decreases exponentially as a function of the distance to the sensor and an effective diameter of trees, following a Poisson model. The effective diameter includes branches, foliage, shrubs, and any other intercepting elements. This method has been used for counting stems and for estimation of biomass from TLS data (Yao *et al.* 2011).
- ii) Modelling a detection function based on distance-sampling (Ducey *et al.* 2013). In this case, the probability of detecting a tree depends on its distance from the sensor. The function to model probabilities is fitted to the distribution of distances of trees that are actually detected (apparent trees). Distance-sampling methods are widely used in ecology, where the mathematical framework for population summary statistics and variance estimation has been established (Buckland *et al.* 2001). Astrup *et al.* (2014) employed two functions to model the probability of tree detection, namely Half-Normal and Hazard-Rate, and estimated volumes with data from TLS.
- iii) Estimation of the proportion of sampling area shadowed by the apparent trees (Seidel and Ammer 2014). The plot area shadowed by trees can be calculated from the diameter and the actual distance from the sensor of all retrieved trees. This method was adapted by Sánchez-González *et al.* (2016) for ForeStereo.

These methods have been tested with TLS data mainly focused on plantations of even-aged stands managed for timber production, but comparative works using ForeStereo data are lacking. The first two methods depend on parameters linked to the stand conditions (density, beam interception by foliage or shrubs, and other features hampering the detection of trees) and may show limitations in natural heterogeneous forests, where the method proposed by Seidel and Ammer (2014) seems more suitable. Under the last method the apparent trees generate a shadowed angular sector behind them. The shadowed area is then subtracted from the sampling plot area. However, this method may underestimate the number of trees of smaller Diameter at Breast Height (DBH) classes for which the probability of nondetection is greater (Sánchez-González *et al.* 2016). Moreover, the method proposed by Seidel and Ammer (2014) must be adapted for use with ForeStereo because in the case of stereoscopic hemispherical images, mensuration requires correspondence between the projection of the tree in both images of the stereoscopic pair, so occlusion in either of the two images hampers tree detection.

The incorporation of PS technologies in operational forest inventories requires information on the accuracy of methods implemented in end-user tools. The accuracy of individual tree diameter at 1.3 m height (DBH) estimation using ForeStereo has been demonstrated in previous studies: Rodríguez-García *et al.* (2014) reported a root mean square error of 0.015 m for DBH in 8 m radius plots, whereas Sánchez-González *et al.* (2016) obtained a Pearson coefficient between DBH field measurement and ForeStereo estimates of 0.86. Sánchez-González *et al.* (2016) also analyzed stand level estimation of N, BA, and mean DBH from ForeStereo data, reporting high agreement between field measurements and ForeStereo estimates in the case of BA but a notable underestimation of N, especially for smaller DBH classes. We present a comparative work in which a ForeStereo dataset is used to estimate plot level variables (N, BA, and DBH distribution) with the aforementioned inference methods, and compared with the noncorrected estimates. We adapt the method proposed by Seidel and Ammer (2014) for estimating the proportion of the sampling area shadowed in the case of stereoscopic hemispherical images acquired with ForeStereo.

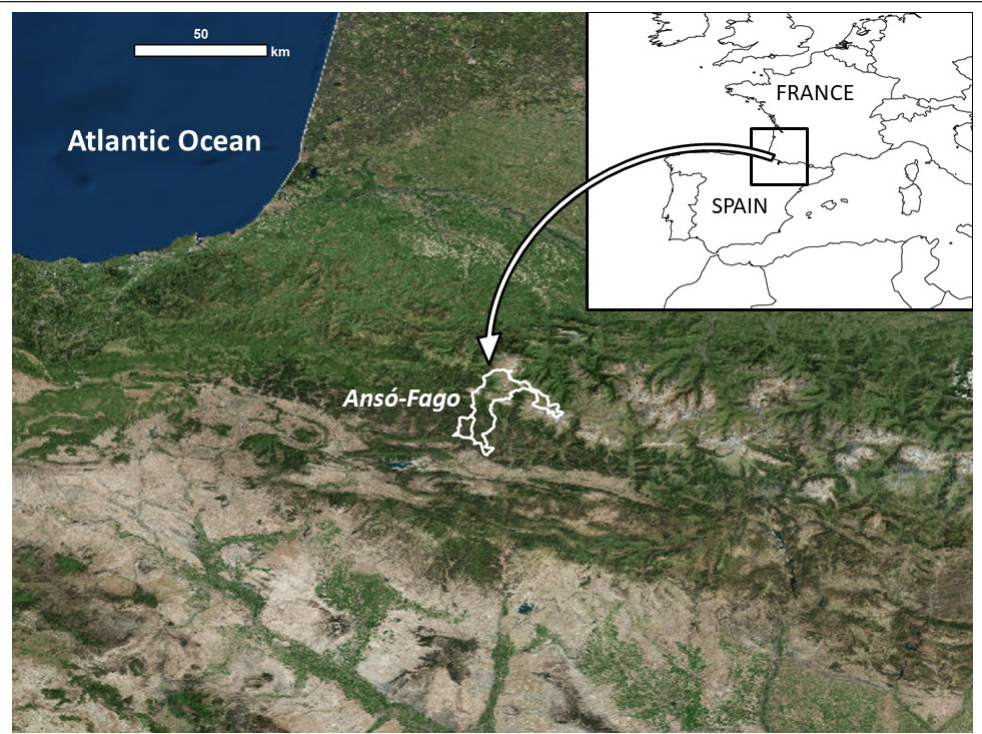


Figure 1. Study area map.

## Material and Methods

### Data Set

Data from mixed stands of *Pinus sylvestris* L. and *Fagus sylvatica* L. were used in this work. Stereo-pairs of hemispherical photos were captured using ForeStereo from the centre of 44 plots randomly selected from a management inventory in a public forest at Ansó, located in the Spanish Pyrenees (Figure 1), and covering a broad range of stand densities and light conditions. The stand originates from natural regeneration and timber is the main production, although it also contains protected areas. The ForeStereo device was located in the plot centre, displacing the center if necessary just to ensure that the nearest tree was at least 0.5 m distant. In addition to the pair of hemispherical photos, the field crew measured the DBH with a calliper and the distance from the plot centre of all trees with DBH > 0.075 m was also measured using a Vertex IV (©Haglöf Sweden 2016). These values were used to calculate basal area and number of trees in fixed radius circular plots of 8 m and 9.8 m, to serve as ground truth reference. The mean N was 1167 trees/ha (SD = 681) and the mean BA was 41 m<sup>2</sup>/ha (SD = 18).

The ForeStereo device used for measurement is a prototype of the MU2005-01738. It is composed of two Fujinon FE185C057HA-1 fish-eye lenses and two Hitachi Kokusai Electric Inc. KP-FD500GV cameras with 5 Mp, a 2/3' charge-coupled device sensor wired to a laptop through Gigabit Ethernet interface (Figure 2). The two cameras are 0.5 m apart and mounted on a light framework. The optical axes of the lenses are parallel and should be vertically aligned when shooting. The image acquisition software was developed using GENICAM™ with a shooting sequence that automatically acquires four pairs of stereoscopic hemispherical photos at 1/9 s, 1/60 s, 1/200 s and 1/1000 s exposures, as proposed by Pueschel (2012) for gap fraction retrieval from hemispherical photos.



Figure 2. ForeStereo prototype used in this study.

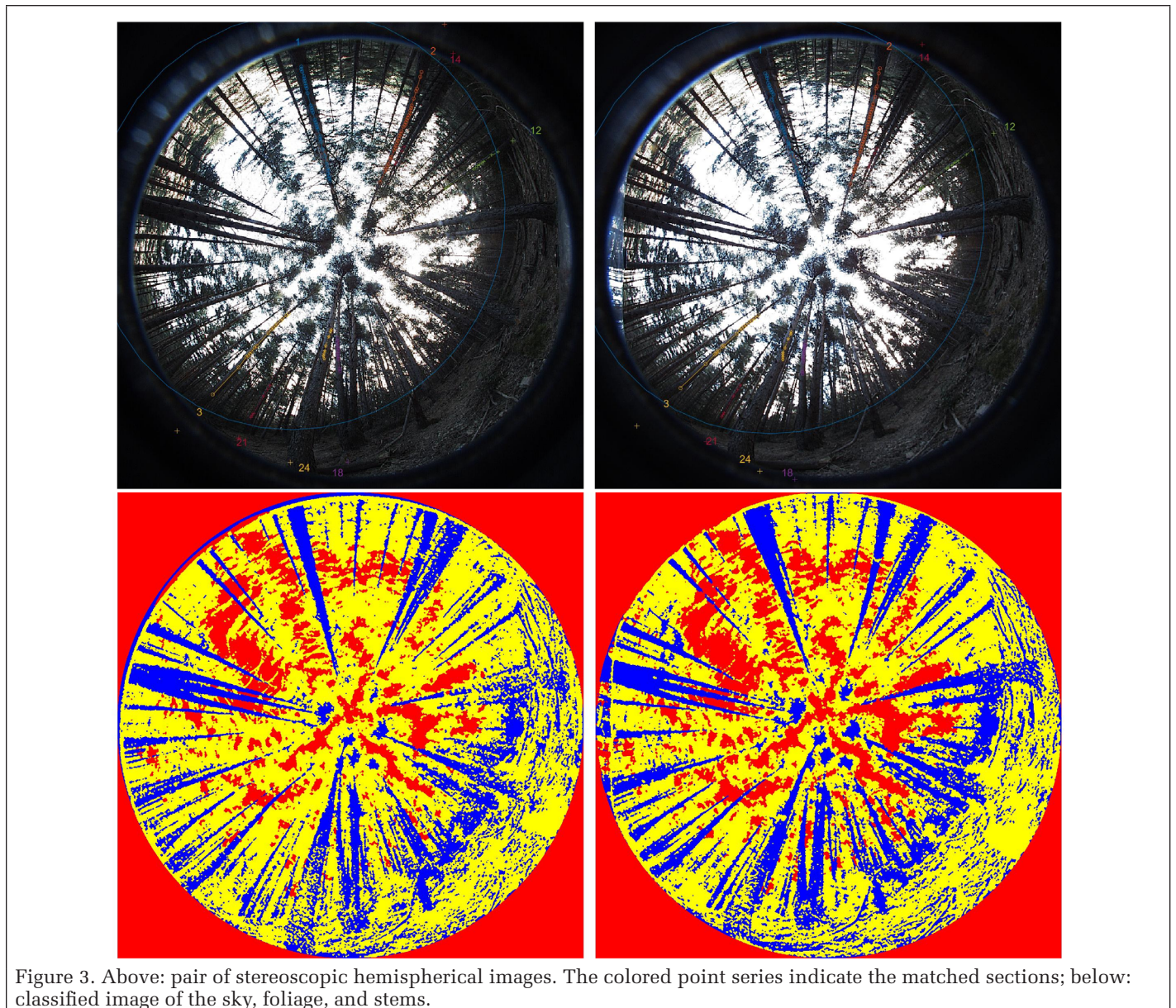
Of the four pairs captured by default, the light conditions at the time of data acquisition determine the most suitable pair of hemispherical photos for identification of trees in the sampling plot. To identify the apparent trees (those viewed in the hemispherical photos) and to estimate the stand variables, an automatic process, fully described in Sánchez-González *et al.* (2016) is implemented in a Matlab® software package developed for the purpose. Basically, the image is segmented into basic components: sky, tree stems, and foliage (Figure 3). During the image segmentation process tree stems are identified in each image through a pixel-based dichotomous hierarchical classification followed by a region-growing process for individual tree labeling. The pixel-based classification establishes four criteria: *intensity* to discriminate the sky, *ratio* between green intensity, and the sum of red, green, blue (RGB) intensities to separate the foliage from the stems, and *local color variance* in the radial and tangential directions to identify homogeneity of texture along the stem and stem boundaries, respectively. The computation of these criteria requires a minimum window size of  $7 \times 7$  pixels, which in turn determines the minimum size of projected stems identifiable during segmentation. Cross-sectional slices are extracted from

the classified image, connected under geometrical constraints, and labeled as individual stems in the region-growing process.

The correspondence process, that is, the matching of a tree identified in both images of a pair, establishes the correspondence between the homologous cross-sectional slices of the segmented stem requiring identification of at least three sections of the tree (Figure 3). The correspondence between sections in both images is determined under restrictions of *epipolarity* (homologous points lie over the epipolar line in the other image), *ordering* (height order of sections is maintained), *similarity* (diameter disparity is minimized), and *uniqueness* (points have a single match) (Herrera *et al.* 2009). A user-guided matching method was used for identification of apparent trees missed by the automatic matching process (Sánchez-González *et al.* 2016).

The distance from the left camera ( $d_1$ ) is calculated with the equations developed by Rodríguez-García *et al.* (2014):

$$d_1 = d_b / \left( \frac{\sin(\alpha_1)}{\sin(\alpha_2)} \cos(\alpha_2) - \cos(\alpha_1) \right) \quad (1)$$



where  $d_b$  is the distance between the optical axes of the cameras, and  $\alpha_1$  and  $\alpha_2$  are the azimuth angles between the base-line and the visual to the target point in the images 1 and 2, respectively. The diameter ( $D_i$ ) of each stem section is then calculated through the covering angle of the stem section in the left image  $\varepsilon_1$  (Figure 4).

$$D_i = 2 * d_1 * \sin(\varepsilon_1 / 2) \quad (2)$$

The accuracy of the distance calculation is limited in the proximity of the base line, where  $\alpha_1$  and  $\alpha_2$  form a very acute angle. For this reason, the alignment of trees with the base line was avoided during image acquisition.

Due to the equidistant projection of fish-eye lenses and the verticality of the lens optical axis, the zenith direction ( $\theta_1$  and  $\theta_2$  in the left and right images respectively) is proportional to the projected radius. The height of the stem section with respect to the lens plane can be determined as:

$$h = d_1 * \cos(\theta_1) / \sin(\theta_1) \quad (3)$$

For each matched section, the correspondence process provides the azimuth direction, horizontal distance, height referred to the lens plane, and diameter. To determine each section height (i.e. the distance to the base of the stem,  $H$ ), a terrain plane is defined using information self-contained in the images by fitting the projected horizon line. Species specific linear taper equations are fitted to the diameter ( $D$ ) and height ( $h$ ) of the sections obtained in the matching process as follows:

$$D = a_i + b_s H \quad (4)$$

where  $D$  is the stem diameter at height  $H$  from the base of tree  $i$  of species  $s$ ,  $a_i$  is the intercept parameter and  $b_s$  is the regression coefficient, which is unique for all trees of the same species measured in the plot. We are interested in the diameter at 1.30 m height (DBH), necessary for estimation of

BA. To calculate the DBH of each tree  $i$  we obtain  $D$  at  $H = 1.30$  m through Equation 4.

#### Estimation of Plot Level Variables

To characterize the forest stand structure,  $N$  and BA were used. These variables are calculated for a circular sample plot of radius  $R$  as:

$$N = n * 10\,000 / (\pi R^2) \quad (5)$$

$$AB = \sum_{i=1}^n \pi (DBH_i / 2)^2 * 10\,000 / (\pi R^2)$$

Diameter classes of 50 mm intervals were considered, with the smaller trees accounted for (7.5-12.5 cm) belonging to the 10 cm class. The number of trees in each diameter class is calculated analogously to  $N$ .

These variables are estimated from the trees identified in the ForeStereo images. During measurements, the sensor resolution limits the maximum range of detection and, as a consequence, the sampling area, particularly for the smaller diameter classes. This effect is known as instrument bias. Furthermore, occlusions by nearby stems hamper the detection of other trees, so shaded sectors should be discounted from the sampling area (Appendix 1). In this work, plot estimates calculated according to three methods that treat occlusions and instrument bias differently have been compared: Relaskop-based estimation to deal with instrument bias combined with the Poisson attenuation model to correct the effect of occlusions; distance-sampling based correction of instrument bias and occlusions; and a new method termed hemispherical photogrammetric correction (HPC), that combines the segmentation based correction for instrument bias proposed by Sánchez-González *et al.* (2016) with a new approach for estimation of occlusion probability which adapts the method proposed by Seidel and Ammer (2014) to the case of stereoscopic hemispherical images.

During the image segmentation and correspondence processes some error from classification of pixels and their correspondence may occur. Missing identification of matching trees leads to some underestimation of  $N$ , whereas pixel classification errors and erroneous matching lead to stem diameter measurement errors and affect the estimation of DBH and BA through the fitting of taper equations. In addition, since DBH is not directly measured at 1.3 m height in the hemispherical images (it is estimated through the linear taper equations) and the height to the measured sections is derived from the fitted terrain model (assumed to be plane for the sampling area), this may contribute to the estimation error in DBH and BA estimations. The quality of  $N$  and BA estimates was evaluated comparing the outcomes with reference data measured in the field, through values of the Pearson correlation coefficient ( $r$ ) and bias, calculated as the mean of differences between estimated minus field values as a percentage of the mean value measured in field (ME). The histograms of diameter distribution were

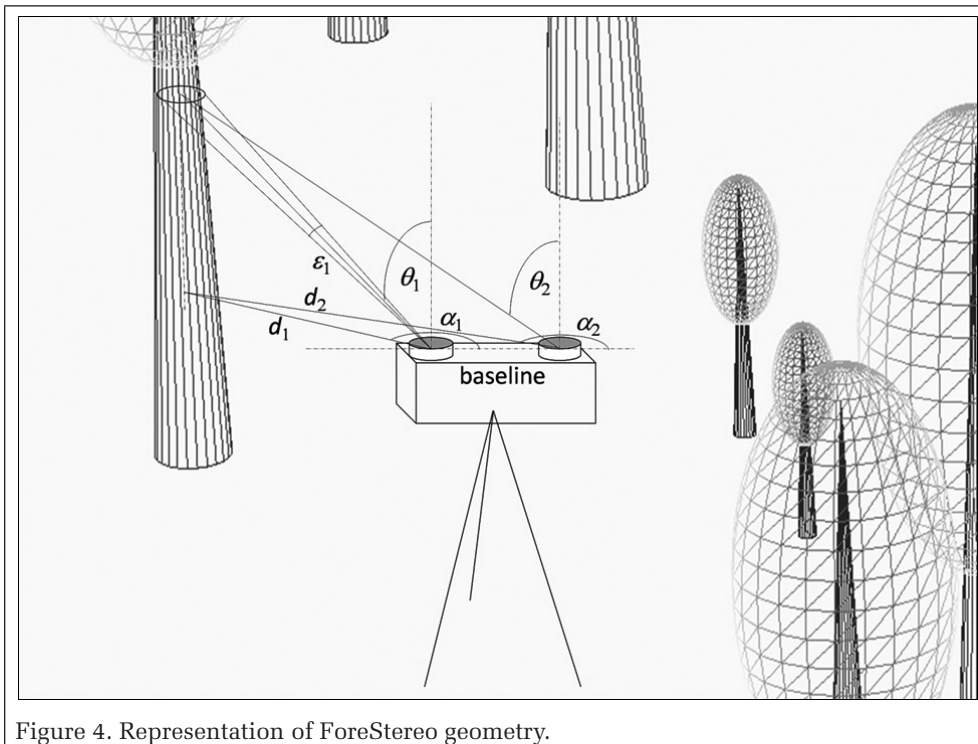


Figure 4. Representation of ForeStereo geometry.

obtained from ForeStereo data with each of the three methods as well as with the caliper measurements, establishing a bin interval of 0.05 m and a minimum value of DBH = 0.075 m. The histograms derived from ForeStereo data and from caliper measurements were compared through the *quadratic-form distance* (Equation 6), proposed by Hafner *et al.* (1995) to assess the similarity between histogram distributions.

$$d(\mathbf{H}_{GroundTruth}, \mathbf{H}_F) = \sqrt{(\mathbf{H}_{GroundTruth} - \mathbf{H}_F)^T \mathbf{A} (\mathbf{H}_{GroundTruth} - \mathbf{H}_F)} \quad (6)$$

where  $(\mathbf{H}_{GroundTruth})$  is the matrix of histogram bin values as derived from caliper measurements and  $(\mathbf{H}_F)$  the matrix of histogram bin values derived from ForeStereo data.  $\mathbf{A}$  is a similarity matrix with  $[a_{ij}]$  denoting the similarity between histogram bins  $i$  and  $j$ , calculated as  $a_{ij} = 1 - |i - j| / \max(|i - j|)$ . Lower values of the quadratic-form distance indicate higher similarity between histogram distributions.

#### Relaskop-Based Estimation Combined with Correction of Occlusion Effect Based on Poisson Attenuation Model

The Relaskop-based approach for estimation of plot or stand level variables is based on the angle-count sampling and has frequently been used in TLS measurement to reduce the instrument bias (e.g., Strahler *et al.* 2008, Lovell *et al.* 2011). Only trees with DBH apparently wider than an angular span  $\kappa$  (which depends on a predefined *basal area factor* (BAF)) are included in the sample. The BAF is typically (and for convenience) set as 0.0002 m<sup>2</sup>/m<sup>2</sup>. With our dataset, the number of trees per m<sup>2</sup> ( $\lambda$ ) was calculated from the  $n$  trees included in the sample as (Equation 7):

$$\lambda = \sum_{i=1}^n \frac{BAF}{\pi * (DBH_i / 2)^2} \quad (7)$$

where

$$BAF = \sin^2(\kappa / 2) \quad (8)$$

The gap probability decreases exponentially with distance  $r$  following a Poisson model of the form  $P_{gap} = \exp(-\lambda D_E r)$ . The number of trees  $n_{corr}$  expected to actually exist in an area of radius  $r_{max}$  (including detected and occluded trees), is expressed as a product of the number of trees actually measured  $n$  and a factor of attenuation  $F(t)$ :

$$n_{corr} = n * F(t) \quad (9)$$

$F(t)$  depends on  $\lambda$ , the effective diameter calculated for all the trees of the plot ( $D_E$ ) and the distance  $r_{max}$ :

$$F(t) = \frac{2}{t^2} (1 - \exp(-t)(1 + t)) \quad (10)$$

$$t = \lambda D_E r_{max}$$

The effective diameter takes into account the occlusive effect of stems, low branches, and understory. Strahler *et al.* (2008) proposed considering a  $D_E$  which depends on the average diameter of the trees actually measured and their variability (Equation 11, where  $C_v$  is a coefficient of variation):

$$D_E = \overline{DBH} (1 + C_v^2)^2 \quad (11)$$

$(n_{corr})_i$  is then estimated for each detected tree and summarized to estimate  $N$ :

$$N = \sum_{i=1}^n (n_{corr})_i * 10\,000 / (\pi r_{max}^2)_i \quad (12)$$

#### Distance-Sampling Based Correction of Instrument Bias and Occlusion Effect

In this approach, the probability of detecting trees in the plot is modeled through the *detection function*  $g(r, \theta)$ . As in Astrup *et al.* (2014), we employed the Half-Normal function:

$$g(r, \theta) = \exp(-r^2 / (2\sigma^2)) \quad (13)$$

and the Hazard-Rate function:

$$g(r, \theta) = 1 - \exp(-(r / \sigma)^{-b}) \quad (14)$$

In  $g(r, \theta)$  the parameter  $\theta$  comprises both the scale ( $\sigma$ ) (in the Half-Normal and the Hazard-Rate functions) and shape ( $b$ ) (only in the Hazard-Rate function) parameters. The inclusion of DBH as a covariate was explored in both models, as in Ducey *et al.* (2014), expanding the scale parameter  $\sigma = \alpha_0 \cdot \exp(\alpha_1 \cdot DBH)$ .

The parameters  $\hat{\theta}$  are obtained by maximum likelihood (Marques and Buckland 2003; Miller and Thomas 2015; Clark 2016). The probability of detection for tree  $i$  in a plot of radius  $R$  is given by Equation 15. Our sampling was truncated at 8 m, 9.8 m, and 15 m to analyze the effect of different  $R$  values on estimates:

$$P_i = \frac{2}{R^2} \int_0^R r * g(r, \hat{\theta}) \quad (15)$$

Finally,  $N$  is estimated as in Equation 16. Note that  $P_i$  is identical for all  $i$  in models without covariate:

$$N = \sum_{i=1}^n 10\,000 / (P_i * \pi R^2) \quad (16)$$

#### Hemispherical Photogrammetric Correction (HPC)

Here we propose a new approach for estimating forest variables at plot and stand level from data obtained using ForeStereo. This approach combines the segmentation-based correction for instrument bias described with detail in Sánchez-González *et al.* (2016), and a new method for estimating the probability of occlusions which adapts the method proposed by Seidel and Ammer (2014) to the case of stereoscopic hemispherical images.

In the equation for instrument bias correction proposed by Sánchez-González *et al.* (2016) the range of detection depends on the stem diameter and the inclination angle of the viewing direction. Stem sections thinner than the minimum window size, defined in pixels as  $p_{sel}$ , are not detected (as mentioned in the segmentation process description). Assuming there are no occlusions, each tree sampling area  $A_i$  is calculated integrating a circular area of radius defined by the user ( $R$ ) or by the maximum horizontal distance  $r_{max}$  at which the section of the tree wider than  $p_{sel}$  is projected on the images (Sánchez-González *et al.* 2016) (Equation 17):

$$A_i = \int_0^{2\pi} \frac{1}{2} (\min(R, r_{max}))^2 d\alpha \quad (17)$$

$$r_{\max} = \frac{D_m * \cos\left(\frac{\pi}{2} - \theta(\alpha)\right)}{2 * \sin\left(\frac{\frac{\pi}{2} P_{\text{sel}}}{2\theta(\alpha) r_{\text{image}}}\right)}$$

where  $D_m$  is the mean diameter of the target tree  $i$  three lowest sections matched (see full description of the matching process in Sánchez-González *et al.* 2016) and the  $\theta(\alpha)$  is the zenith angle of the viewing direction at each azimuthal direction for the the third lowest section estimated from all the matched trees using cubic splines (Sánchez-González *et al.* 2016).

The effect of occlusions should be corrected using the information contained in the sample of apparent (i.e. not occluded) trees. To estimate the actual nonshaded sampling area, the theoretical sampling area  $A_i$  (Equation 17) is multiplied by the probability of detection  $P_i$  of each apparent tree  $i$ .  $N$  is then computed as:

$$N = \sum_{i=1}^n 10\,000 / (P_i * A_i) \quad (18)$$

If  $S_0$  is the nonshaded area, the probability of detecting tree 0 in a sampling plot of radius  $r_{\max}$ , considering the potential shadowing of all other apparent trees is determined as:

$$P_0 = S_0 / \pi r_{\max}^2 \quad (19)$$

The term shadowing in this case refers to nondetection during the matching process. Matching fails to detect or identify a tree when the stem is partially or completely missed in any of the two stereo-images. In contrast, the method developed for application to TLS data by Seidel and Ammer (2014) estimates the shadowed area for a single scan.

In order to calculate  $S_0$ , let  $d_{01}$  and  $d_{02}$  be the horizontal distances from the left and right cameras to tree 0 (Figure 5a) and analogously  $d_{i1}$  and  $d_{i2}$  the horizontal distances from the left and right cameras to tree  $i$ , ( $i = 1 \dots n$ ,  $n$  being the number of apparent trees).  $S_0$  can be computed as the integral of the circumference length, from  $d_{01} = 0$  to the maximum sampling

radius  $r_{\max}$  (remember  $r_{\max}$  depends on the tree size) multiplied by the probability of no occlusion at  $d_{01}$ :

$$S_0 = \int_0^{r_{\max}} d_{01} * 2\pi * P(d_{01}) dd_{01} \quad (20)$$

For each distance  $d_{01}$ , the probability of no occlusion  $P(d_{01})$  is the product of no occlusion probability in the left image  $P(S_{01})$  and no occlusion probability in the right image, conditional on being visible in the left image  $P(S_{02} | S_{01})$ :

$$P(d_{01}) = P(S_{01}) * P(S_{02} | S_{01})$$

$$P(S_{01}) = S_{01} / 2\pi \quad (21)$$

$$P(S_{02} | S_{01}) = S_{02} / S_{01}$$

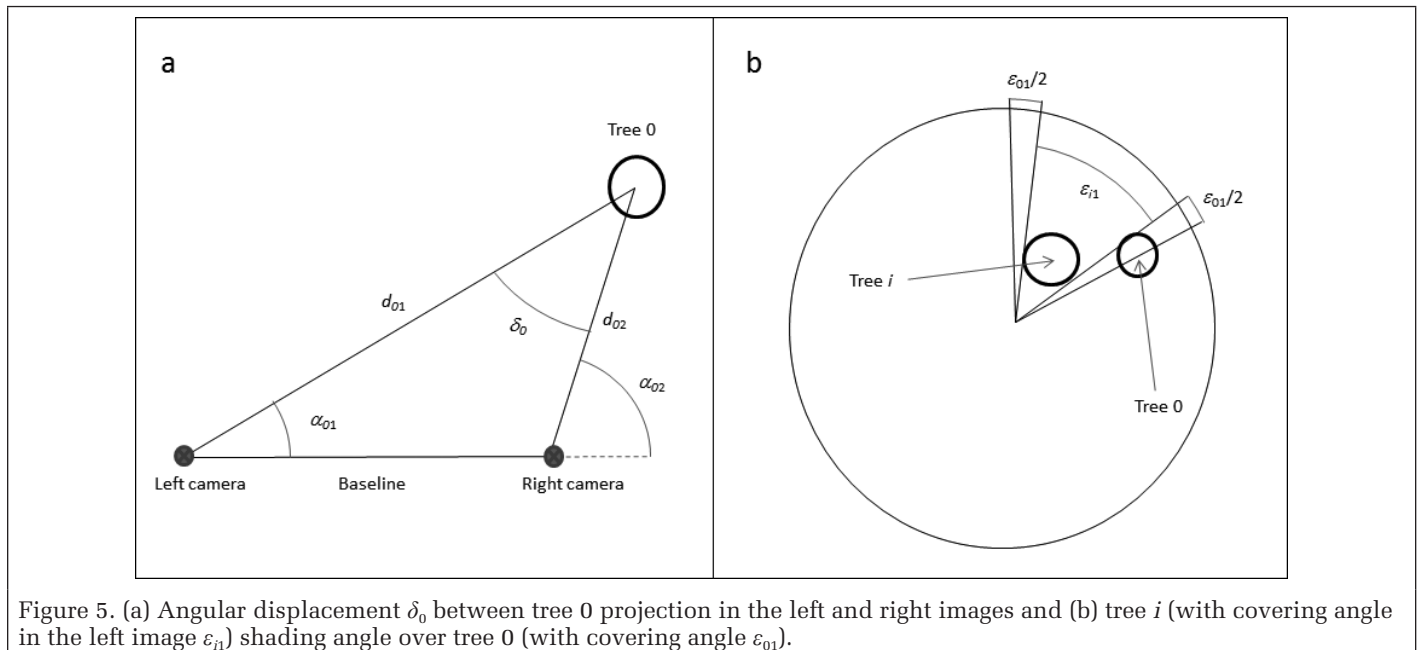
where  $S_{01}$  is the angle where there is no occlusion in the left image and  $S_{02}$  is the angle where there is no occlusion in the right image conditional on being visible in the left image. In order to calculate  $S_{01}$  and  $S_{02}$ , let  $\varepsilon_{01}$  and  $\varepsilon_{02}$  be the angle span covered by tree 0 in the left and right images respectively (Figure 5b)—and analogously  $\varepsilon_{i1}$  and  $\varepsilon_{i2}$  for tree  $i$ .  $S_{01}$  equals a complete sampling round  $2\pi$  minus the sum of occlusion angles in the left image  $o_{i01}$  produced by all shading trees  $i$  closer to the device (Equation 22, where  $I(d_{01} < d_{i1})$  equals 1 if  $d_{01} < d_{i1}$  and 0 in any other case).

$$S_{01} = 2\pi - \sum(o_{i01} * I(d_{01} < d_{i1})) \quad (22)$$

Likewise,  $S_{02}$  can be computed as the difference of the visible angle in the left image  $S_{01}$  minus the sum of occlusion angles  $o_{i02}$  of trees located closer to the device:

$$S_{02} = S_{01} - \sum(o_{i02} * I(d_{02} < d_{i2})) \quad (23)$$

Tree 0 occlusion angle produced by tree  $i$  ( $o_{i01}$ ) is the angle at which tree 0 is totally or partially shaded by tree  $i$ , calculated as a sum of covering angles:



$$o_{i01} = \varepsilon_{i1} + \varepsilon_{01} \quad (24)$$

The occlusion angle  $o_{i02}$  conditional on no occlusion in the left image require that the projection of tree 0 in the right image be conditioned by it being visible in the left image. Moreover, in order to estimate the integral in Equation 20,  $o_{i01}$  and  $o_{i02}$ , and henceforth  $\varepsilon_{01}$  and  $\varepsilon_{02}$ , should be expressed as a function of  $d_{01}$ . Thus, let  $\alpha_{01}$  and  $\alpha_{02}$  be the azimuthal angles formed by the visual line from the left and right cameras to tree 0 with the camera baseline (Figure 5a) and  $\alpha_{i1}$  and  $\alpha_{i2}$  the analogous angles for tree  $i$ .  $\varepsilon_{01}$  depends on the diameter and distance to the device of tree 0, which in turn depends on the horizontal distance and the terrain slope in the direction towards tree 0 (Equation 25),  $\sigma_{\max}$  being the maximum slope in the plot and  $\alpha_{\sigma_{\max}}$  the direction upslope.

$$\varepsilon_{01} = 2 \cdot \operatorname{asin} \left( \frac{\operatorname{DBH}_0}{2d_{01} / \cos(\operatorname{atan}(\tan(\sigma_{\max}) \cos(\alpha_{01} - \alpha_{\sigma_{\max}})))} \right) \quad (25)$$

Analogously, the covering angle of tree 0 in the right image is:

$$\varepsilon_{02} = 2 \cdot \operatorname{asin} \left( \frac{\operatorname{DBH}_0}{2d_{02} / \cos(\operatorname{atan}(\tan(\sigma_{\max}) \cos(\alpha_{02} - \alpha_{\sigma_{\max}})))} \right) \quad (26)$$

If  $\delta_0$  is the angular displacement between the projection of tree 0 in the left and right images (Figure 5a) then:

$$\alpha_{02} = \alpha_{01} + \delta_0 \quad (27)$$

The displacement between tree 0 projected in the left and right images can be expressed by Equation 21 (Rodríguez-García *et al.* 2014 and Figure 5a). For convenience, we refer  $d_{02}$  to  $d_{01}$ :

$$\delta_0 = \operatorname{asin} \left( \operatorname{baseline} \frac{\sin(\alpha_{01})}{d_{02}} \right) \quad (28)$$

$$d_{02} = \sqrt{\operatorname{baseline}^2 + d_{01}^2 - 2 \cdot \operatorname{baseline} \cdot d_{01} \cos(\alpha_{01})}$$

In order to calculate  $o_{i02}$ , we should define  $\alpha_{i01\min}$ ,  $\alpha_{i01\max}$  as the enclosing angles of  $o_{i01}$ . As Figure 5b shows,  $\alpha_{i01\min}$  and  $\alpha_{i01\max}$  can be expressed as:

$$\alpha_{i01\min} = \alpha_{i1} - \frac{o_{i01}}{2} \quad \alpha_{i01\max} = \alpha_{i1} + \frac{o_{i01}}{2} \quad (29)$$

Analogously,  $\alpha_{i02\min}$ ,  $\alpha_{i02\max}$  are the enclosing angles of the nonconditioned occlusion angle in the right image and can be expressed as:

$$\alpha_{i02\min} = \alpha_{i2} - \frac{(\varepsilon_{i2} + \varepsilon_{02})}{2} \quad \alpha_{i02\max} = \alpha_{i2} + \frac{(\varepsilon_{i2} + \varepsilon_{02})}{2} \quad (30)$$

To calculate the occlusion angle in the right image conditional on being visible in the left image, we must subtract the azimuth angles in the right image corresponding to occluded angles in the left image. Depending on the distance from the tree to the device, the projection angle in the right image is displaced along the epipolar line. Thus, the projection of tree 0 in the right image conditional on no occlusion in the left image should be in the range between  $\alpha_{i01\max} + \delta_{0\max}$  and  $\alpha_{i01\min} + \delta_{0\min}$ . Three cases can be distinguished (Figure 6) to calculate  $o_{i02}$ , depending on the angular displacement of trees  $i$  and 0:

Case 1.  $\alpha_{i02\min} > \alpha_{i01\max} + \delta_{0\max}$

In this case the angle shaded by tree  $i$  in the right image lies completely within the range of tree 0 projection in the right image conditional on no occlusion in the left image. Therefore, in the right image, the occlusion angle conditional on no occlusion in the left image coincides with the shaded angle:

$$o_{i02} = \alpha_{i02\max} - \alpha_{i02\min} \quad (31)$$

Case 2.  $\alpha_{i02\min} > \alpha_{i01\max} + \delta_{0\max}$  and  $\alpha_{i02\min} > \alpha_{i01\min} + \delta_{0\min}$

In this case the angle shaded by tree  $i$  in the right image lies partially within the range of tree 0 projection in the right image conditional on no occlusion in the left image, and the angular displacement of tree  $i$  (from left to right image) is greater than the angular displacement of tree 0. The occlusion

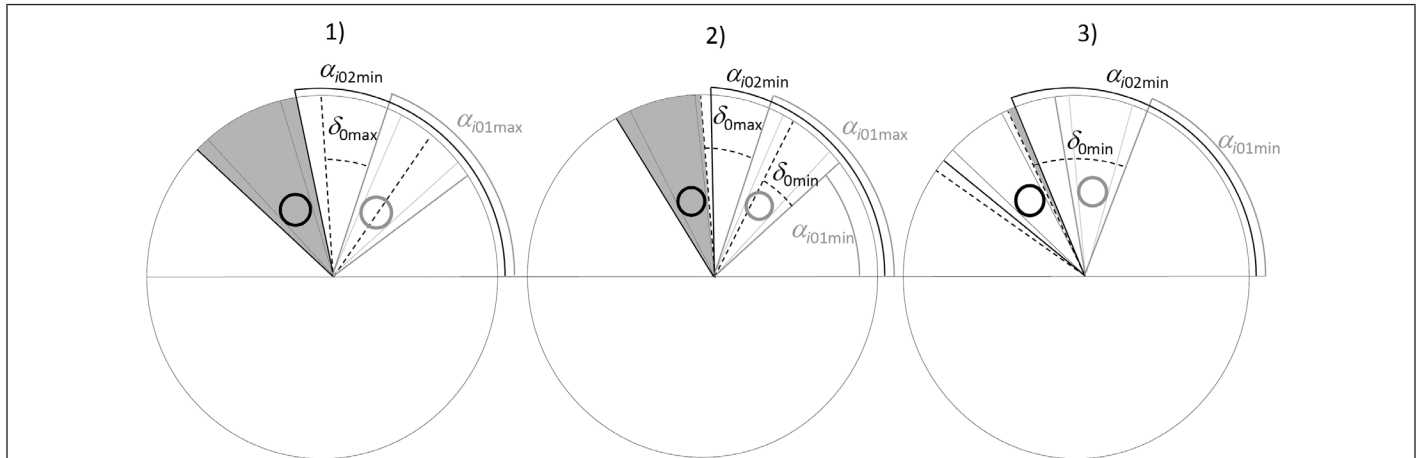


Figure 6. Geometric relationships between tree 0 projected on the right image conditional on being visible in the left image, and the shaded angle by tree  $i$  in the right image in the case 1), case 2), and case 3); grey lines correspond to the occlusion angle in the left image; continuous black lines correspond to the occlusion angle in the right image; discontinuous black lines correspond to maximum and minimum displacement of tree 0 projection from right to left image when tree 0 is occluded by tree  $i$  in the left image. The grey area corresponds to the conditional occluded angle in the right image ( $o_{i02}$ ).

angle in the right image conditional on no occlusion in the left image coincides with the intersection of the total shaded angle and the range in the right image corresponding to being visible in the left image:

$$o_{i02} = \alpha_{i02\max} - (\alpha_{i01\max} + \delta_{0\max}) \quad (32)$$

Table 1. Bias (ME) and Pearson coefficient ( $r$ ) of the relationship between measured and estimated number of trees per ha ( $N$ ) in plots of 8 m, 9.8 m, and 15 m radius  $R$ .

	$R = 8 \text{ m}$		$R = 9.8 \text{ m}$		$R = 15 \text{ m}^*$	
	ME (%)	$r$	ME (%)	$r$	ME (%)	$r$
ForeStereo sample without correction	-42	0.54	-52	0.50	-77	0.40
Relaskop sampling + Poisson attenuation model	-35	0.52	-46	0.49	-69	0.53
Distance-sampling (Hazard-Rate)	16	0.54	31	0.50	26	0.40
Distance-sampling (Hazard-Rate + covariate)	11	0.60	22	0.60	<b>12</b>	<b>0.58</b>
Distance-sampling (Half-Normal + covariate)	33	<b>0.62</b>	53	<b>0.62</b>	49	<b>0.59</b>
HPC	<b>-6</b>	0.61	<b>-10</b>	0.59	-33	0.56

\*ForeStereo estimates with 15 m maximum distance are compared with the values calculated with the 9.8 m radius field plot.

Case 3.  $\alpha_{i02\min} < \alpha_{i01\min} + \delta_{0\min}$

In this case the angle shaded by tree  $i$  in the right image lies partially in the range of tree 0 projection in the right image conditional on no occlusion in the left image. Also, the angular displacement of tree  $i$  (from left to right image) is smaller than the angular displacement of tree 0. The occlusion angle in the right image conditional on no occlusion in the left image coincides with the intersection of the angle shaded and the range in the right image corresponding to being visible in the left image:

$$o_{i02} = \alpha_{i01\min} + \delta_{0\min} - \alpha_{i02\min} \quad (33)$$

We calculated  $\alpha_{i02\max}$  and  $\alpha_{i02\min}$  for both  $\alpha_{01} = \alpha_{i01\max}$  and for  $\alpha_{01} = \alpha_{i01\min}$ , obtaining the maximum and minimum (not necessarily in that order) values for  $o_{i02}$ . The final  $o_{i02}$  is the average of  $o_{i02}$  calculated for  $\alpha_{i01\max}$  and for  $\alpha_{i01\min}$ .

## Results

### Number of Trees

As expected,  $N$  was largely underestimated with the ForeStereo sample of matched trees when not corrected for instrument bias and occlusion effect; the bias increased with the maximum sampling distance and the mean error ranged from 42% to 77% (Table 1). The underestimation of  $N$  was more relevant in plots of higher density (Figure 7)—those occupied by smaller trees. The Relaskop-based sampling with Poisson

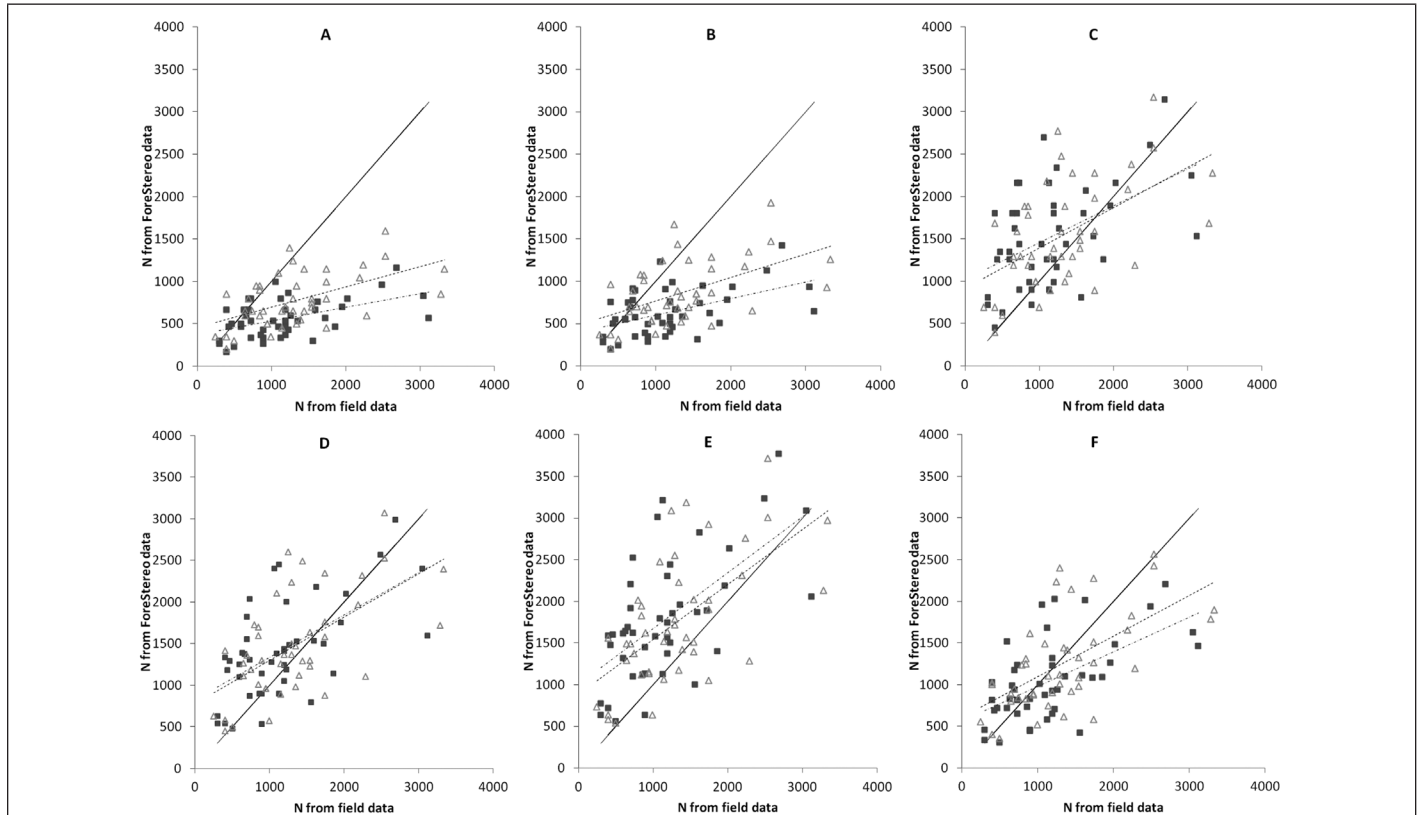


Figure 7. Number of trees per ha ( $N$ ) estimates from ForeStereo vs  $N$  estimated from field measurements and regression line of linear models in plots of 8 m (empty triangles and dashed line) and 9.8 m radius (filled squares and dash-dot line). A: uncorrected, B: Relaskop-based sampling and Poisson attenuation model, C: distance-sampling Hazard-Rate function, D: distance sampling with Hazard-Rate function and DBH as covariate, E: distance sampling with Half-Normal function and DBH as covariate, F: hemispherical photogrammetric correction.

attenuation model for correction of occlusions reduced the estimation bias slightly, to between 35%–69%. Among the distance-sampling options the Hazard-Rate function performed better than the Half-Normal function in terms of bias, although the latter showed higher values of correlation with field data. Although the distance-sampling method tends to overestimate  $N$ , this overestimation is more notable with the Half-Normal function. The Half-Normal model does not accurately fit the distribution of distances: the  $r^*g(r, \theta)$  function should be proportional to the frequency histogram by distance bins, however, the curve (scaled to make the integral of the curve between 0 and  $R$  equal to the number of detected trees) is over the detected frequencies at short as well as large distances and below the detected frequencies for intermediate distances (Figure 8). As most detected trees are located at intermediate distances (3–5 m), the underestimation of the sampling probability for these distances results in an overestimation of  $N$ . HPC estimates had the lowest bias for 8 m and 9.8 m sampling distances (-6% and -10%, respectively), but tended

to underestimate  $N$  when the distance sampled increased to 15 m (bias of -33%). To help disentangle the effect of instrument bias and occlusion effect corrections, Figure 9 compares the distribution of sampling areas of all detected trees in the 15 m plots in the cases of instrument bias correction alone and instrument bias combined with the occlusion corrections for the Relaskop-based sampling with Poisson attenuation model and for the HPC. The first method bases the instrument bias correction on DBH, whereas HPC employs the diameters detected during image segmentation, which are usually over 1.30 m height and are smaller than the DBH, resulting in a greater reduction in sampling area for most trees (Figure 9). Moreover, the Poisson attenuation model mainly depends on plot density, providing a similar reduction in sampling area for all trees in the plot, whereas the occlusion correction proposed by HPC varies for each tree depending on the size and position of all other trees within the plot.

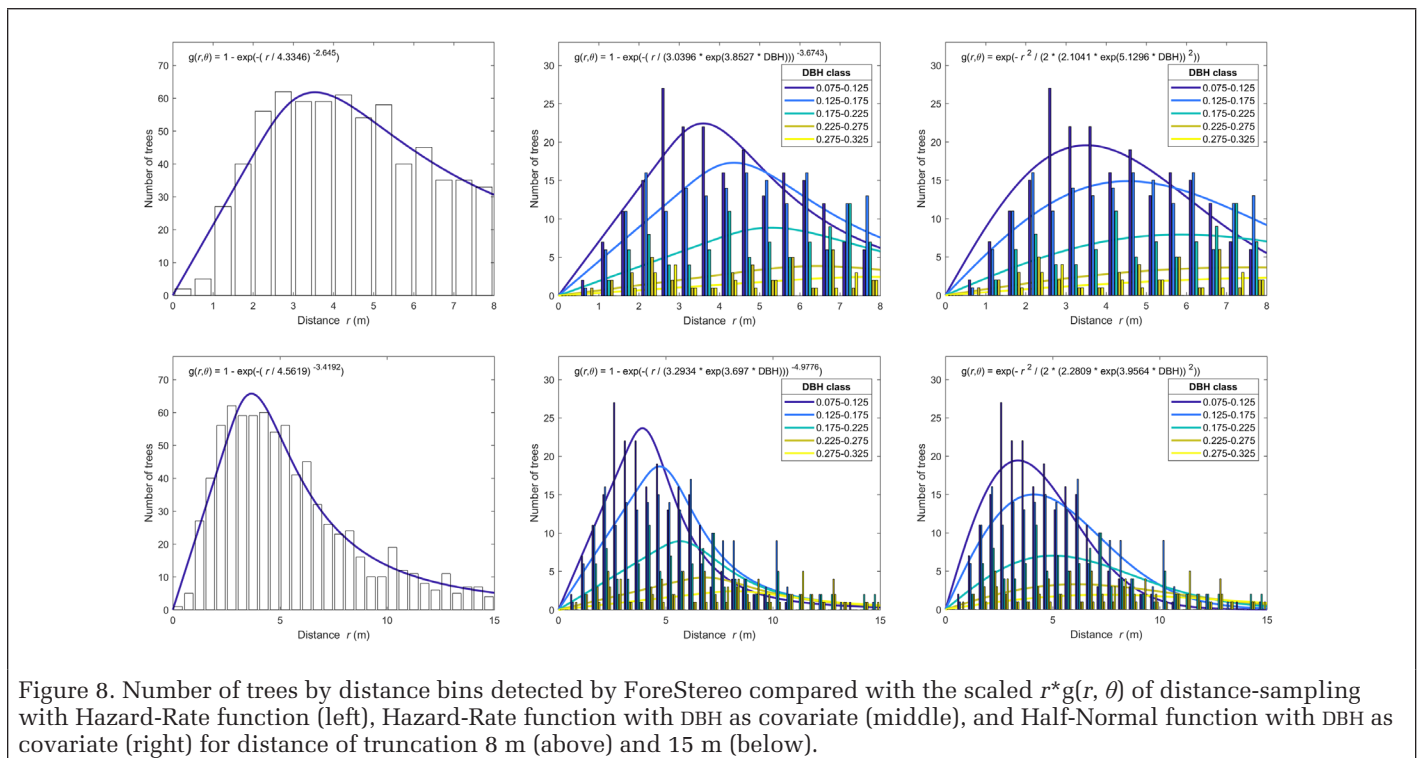


Figure 8. Number of trees by distance bins detected by ForeStereo compared with the scaled  $r^*g(r, \theta)$  of distance-sampling with Hazard-Rate function (left), Hazard-Rate function with DBH as covariate (middle), and Half-Normal function with DBH as covariate (right) for distance of truncation 8 m (above) and 15 m (below).

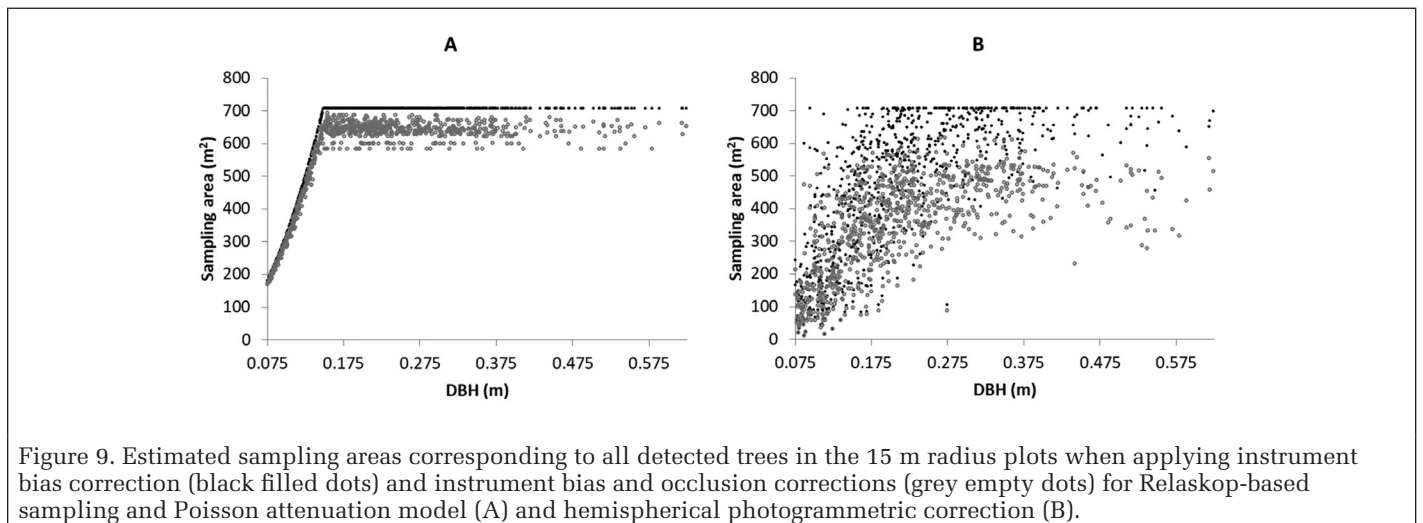


Figure 9. Estimated sampling areas corresponding to all detected trees in the 15 m radius plots when applying instrument bias correction (black filled dots) and instrument bias and occlusion corrections (grey empty dots) for Relaskop-based sampling and Poisson attenuation model (A) and hemispherical photogrammetric correction (B).

### Diameter Distribution

The distributions of DBH derived from field data and from ForeStereo estimates are compared in Figure 10. The histograms derived from ForeStereo estimates without correction and those corrected using Relaskop-based estimation combined with the Poisson attenuation model are similar; tending to underestimate the number of trees by diameter class, especially for the smaller diameters (0.075 m–0.125 m class) and in larger plots. The majority of approaches correcting instrument bias and tree occlusions improved the noncorrected estimates and had lower quadratic-form distances than the field measured distribution (Table 2). The distance-sampling method using Hazard-Rate function without covariate underestimates the smallest diameter class (0.075 m) and overestimates classes over 0.125 m. As observed in Figure 8, the globally adjusted distance distribution function  $g(r, \theta)$  for the Hazard Rate model without covariate is influenced by the distance distribution of the smaller classes, which are not detected at long distances. This may be the reason for the overestimation of the detection probability of larger trees at greater distances, leading to an over-correction for these trees. This problem is solved when DBH is included as covariate. The distance-sampling with Half-Normal function overestimates the number of trees with DBH < 0.275 m as a consequence of the underestimation of the detection probability for these diameter classes, shown as a flattening of the  $r^*g(r, \theta)$  curve (Figure 8). When DBH is included as covariate, the distance-sampling with Hazard-Rate function results in a diameter distribution with greater similarity to the diameter distribution measured in the field—as assessed by the quadratic form distance—when the maximum sampling distance is 9.8 or 15 m (Table 2).

The DBH distribution obtained with HPC showed the closest agreement with field data measured in 8 m plots and the overall minimum quadratic form distance (Table 2 and Figure 10). When the distance was increased to 15m HPC underestimated the density of most DBH classes (Figure 10, right).

### Basal Area

BA was underestimated in the majority of plots when no correction was applied to the sample of detected trees (Figure 11). The degree of underestimation is greater in dense plots with high values of BA and for large maximum sampling distances. Relaskop-based estimations with the Poisson attenuation correction reduced the estimate bias from 35% to 28% (Table 3). Distance-sampling using the Hazard-Rate function without covariate and with Half-Normal function with

Table 2. Quadratic form distance between the DBH histograms derived from the field data and the DBH histograms derived from ForeStereo data in plots of 8 m, 9.8 m, and 15 m radius  $R$ .

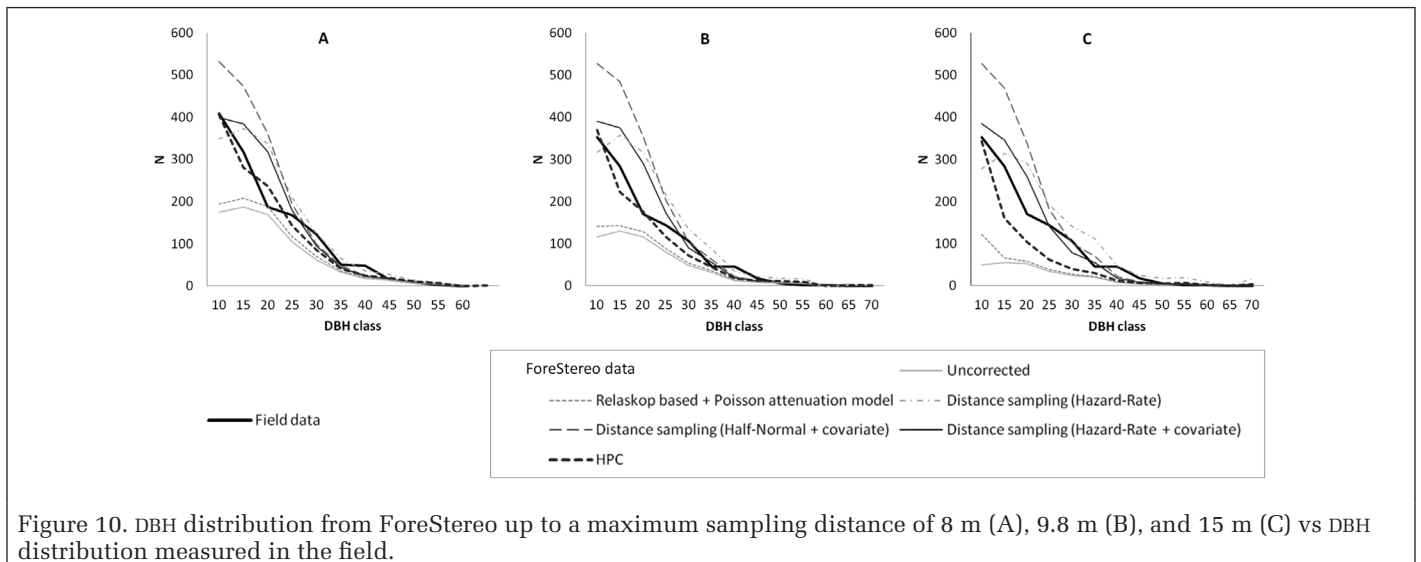
	$R = 8 \text{ m}$	$R = 9.8 \text{ m}$	$R = 15 \text{ m}$
ForeStereo sample without correction	501.84	561.57	854.03
Relaskop sampling + Poisson attenuation model	425.53	497.09	762.19
Distance-sampling with Hazard-Rate function	209.07	319.80	273.75
Distance-sampling with Hazard-Rate function + covariate	78.50	<b>78.96</b>	<b>139.26</b>
Distance-sampling with Half-Normal function+ covariate	424.35	583.97	543.91
HPC	<b>72.65</b>	117.22	373.75

Table 3. Bias (ME) and Pearson coefficient ( $r$ ) between measured and estimated basal area ( $\text{m}^2/\text{ha}$ ) in plots of 8 m, 9.8 m, and 15 m radius  $R$ .

	$R = 8 \text{ m}$		$R = 9.8 \text{ m}$		$R = 15 \text{ m}^*$	
	ME (%)	$r$	ME (%)	$r$	ME (%)	$r$
ForeStereo sample without correction	-35	0.78	-42	0.67	-66	0.48
Relaskop sampling + Poisson attenuation model	-28	0.79	-36	0.68	-61	0.51
Distance-sampling (Hazard-Rate)	29	0.78	57	0.66	92	0.47
Distance-sampling (Hazard-Rate + covariate)	4	0.82	13	0.71	5	0.59
Distance-sampling (Half-Normal + covariate)	16	0.82	36	0.71	35	0.59
HPC	-8	0.83	-11	0.78	-35	0.60

\*ForeStereo estimates with 15 m maximum distance are compared with the values calculated with the 9.8 m radius field plot.

covariate resulted in a notable overestimation of BA. However, this method showed better results in terms of bias when the detection function used was the Hazard-Rate with covariate (4%–11%). The HPC method with 8 m plots slightly underestimated BA (-8%) but showed the highest Pearson correlation



coefficient between BA estimated from ForeStereo data and field measurements (0.83).

## Discussion and Conclusions

Estimation of forest stand variables from sample data captured using ForeStereo requires precise knowledge of the sources of error associated with sampling schemes, image processing, and estimation methods. This work analyzed the performance of different methods for estimating sampling probability. Working with a single point sampling design the probability of sampling a tree depends on two factors: the relationship between the distance range of detection and the tree size, and the probability of being occluded by another tree. In addition, in order to attain unbiased estimations, the locations of the plot centres should be selected randomly or on a regular grid, but not prevailing open locations within the plot. The displacement of the device to a distance of 0.5 m from the nearest tree is necessary as the variability of textures within the stem associated with the macro-acquisition of images hampers stem segmentation. Due to the wide field of view of the fish eye lens, the size of the features projected decreases rapidly at 0.5 m and the occlusion effect is reduced substantially. However, this displacement is small when compared with the tree spacing and should not cause a noticeable bias. The relationship between the distance range of detection and the tree size is defined by the image resolution and by the algorithms used in the segmentation process. The probability of occlusion has to be inferred from the actual distribution of the apparent trees. Employing ForeStereo data from a forest

inventory, we tested and compared three approaches for estimating the sampling probability and calculating plot level variables: Relaskop-based sampling and correction of occlusions with Poisson attenuation model, distance-sampling based correction for instrument bias and occlusions, and the proposed HPC, which combines the segmentation based correction for instrument bias method (Sanchez-González *et al.* 2016) and a new correction of occlusions effect calculating the shadowed area, based on the Seidel and Ammer (2014) method. The three approaches incorporate some kind of correction for instrument bias and occlusion of trees, and all three led to an improvement in the raw estimates; reducing the estimate bias and increasing the correlation with ground truth data.

Each method for estimating sampling probability is supported by different assumptions, and the suitability of one or other method depends on the forest structure and on the characteristics of the PS technology employed. For example, the approach consisting of Relaskop-based sampling and correction of occlusions with Poisson attenuation model (Strahler *et al.* 2008) depends on the DBH of the apparent trees and on the basal area factor selected and assumes a Poisson distribution of tree distances from the sensor. For an accurate determination of the effective tree diameter  $D_e$ , this method may require calibration (e.g. with traditionally measured plots). Ducey *et al.* (2014) and Astrup *et al.* (2014) proposed a distance-sampling based approach relying on the actual distribution of the apparent tree distances. Under this approach, the assumptions are implicit in the model selected for probability of detection (e.g. Half-Normal or Hazard-Rate functions). Employing

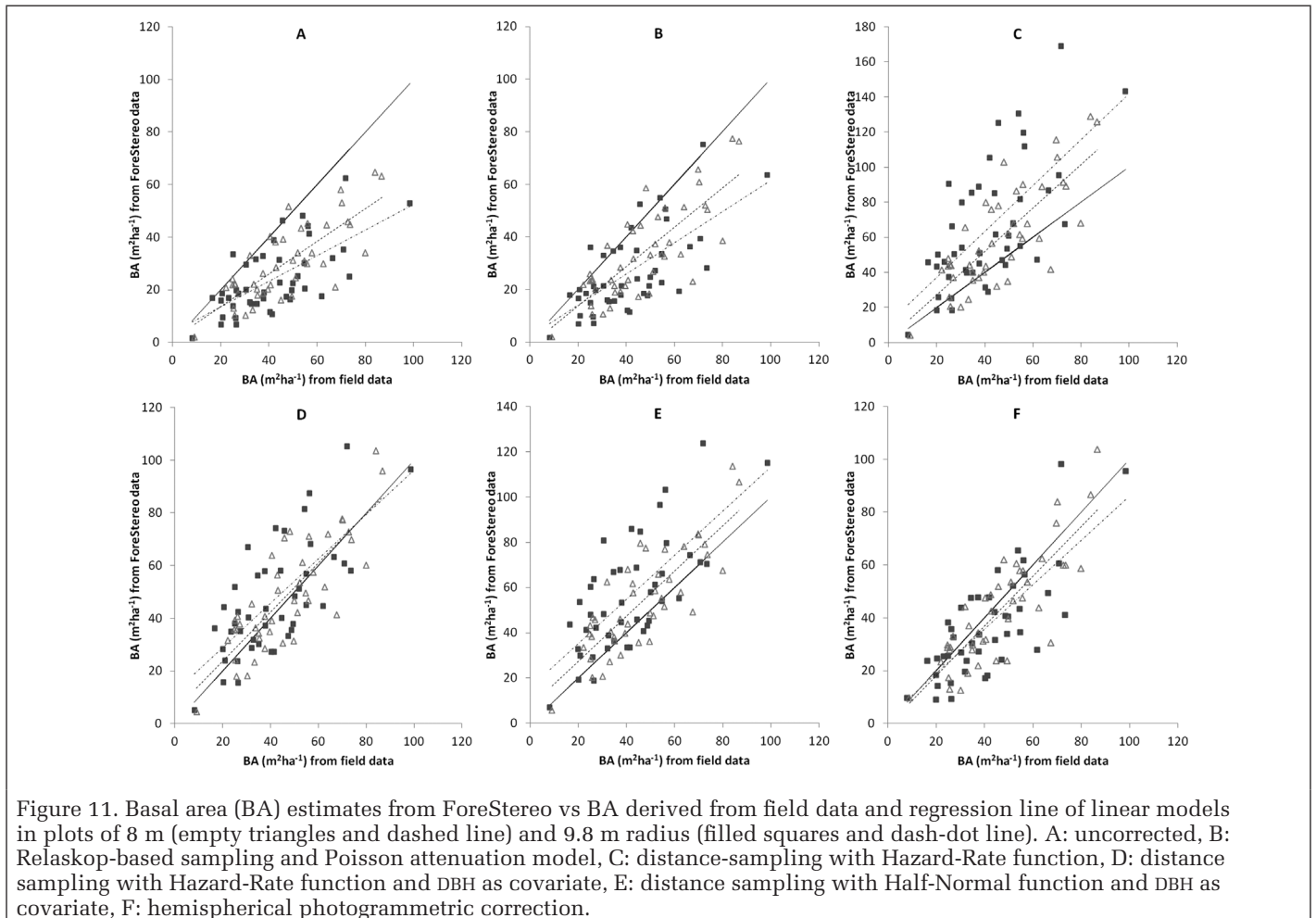


Figure 11. Basal area (BA) estimates from ForeStereo vs BA derived from field data and regression line of linear models in plots of 8 m (empty triangles and dashed line) and 9.8 m radius (filled squares and dash-dot line). A: uncorrected, B: Relaskop-based sampling and Poisson attenuation model, C: distance-sampling with Hazard-Rate function, D: distance sampling with Hazard-Rate function and DBH as covariate, E: distance sampling with Half-Normal function and DBH as covariate, F: hemispherical photogrammetric correction.

actual distances makes this approach more adaptable than the attenuation model to the forest stand conditions that affect the detection of trees (e.g. presence of under-canopy vegetation). However, the parameterization of the detection function is based on the distances actually measured in all plots within a stand or strata, so this method would seem to be more appropriate for homogeneous stands. Unlike applications described in Ducey *et al.* (2014) and Astrup *et al.* (2014), where the inclusion of covariates in the models did not significantly improve the estimates, we achieved the better performance

## Appendix 1



Figure A1. Example of instrument bias: The stem section marked with a red arrow cannot be detected due to instrument bias because the pixel size is of similar magnitude to the stem projection width.

by incorporating DBH as covariate in the detection probability. Sánchez-González *et al.* (2016) proposed an approach for estimating sampling probability which combines an instrument bias correction based on the minimum window size allowed by the process of image segmentation and an occlusion effect correction adapted to ForeStereo from that of Seidel and Ammer (2014) using TLS data. The hemispherical photogrammetric correction described here combines the instrument bias correction proposed by Sánchez-González *et al.* (2016) with an improved correction of the occlusion effect. This method integrates the probability of no occlusion for the entire sampling range calculated from the size and position of apparent trees. Seidel and Ammer (2014) worked with circular plots of 2 m radius in dense poplar plantations and obtained correlations of 0.9 between BA estimates from data captured with TLS and ground truth data; the estimate bias was reduced by 1.4% (from -9.8% to -8.4%) after correction. The HPC approach reduced the bias of BA estimates in plots of 8 m radius from -35% to -8% in structurally diverse forests (i.e. with irregular distribution of tree sizes). Notwithstanding the differences in stand structure and between TLS data and stereo-hemispherical photos, the more significant improvement in our analysis may be related to the integration of the instrument bias correction and to an improved estimation of the area occluded. In the estimation of the occlusion probability with stereo-hemispherical photos, partial blockage hinders tree matching; therefore, the occlusion angle is the sum of the coverage angles of the occluded and shading trees (Ducey *et al.* 2014).

Correspondence between the projections of a tree in both stereo images captured with ForeStereo is necessary in order to detect the tree. The probability of detection has therefore to be computed as a product of the probability of no occlusion in the left image, by the probability of no occlusion in the right image conditional on being visible in the left. This need for this correspondence may explain the underestimation of BA and N in our analyses with the Poisson attenuation model correction of occlusions. The distance-sampling based approach relies on the distance distribution of apparent trees and, in contrast, is not affected by the correspondence issue. Single scan sampling with TLS typically overestimates the mean DBH, since the occlusion probability is greater for smaller trees (Strahler *et al.* 2008; Lovell *et al.* 2011; Yao *et al.* 2011; Seidel and Ammer 2014). We estimated the occlusion probability as an integral over the range of detection for each tree, and the relation between the covering angles of the target



Figure A2. Example of occlusion: The tree marked with an arrow in the right image is occluded by tree marked with a triangle in the left image.

and shading trees is recalculated for each distance, providing a reduced bias in the estimation of the number of trees of smaller DBH classes.

The Relaskop-based method for correction of instrument bias combined with the Poisson attenuation model for correction of occlusions has proved to substantially reduce bias in  $N$  (Strahler *et al.* 2008) and  $BA$  (Strahler *et al.* 2008; Lovell *et al.* 2011) estimated with single scan TLS data. Likewise, Yao *et al.* (2011) reported correlations of 0.902 and 0.656 with field data when estimating  $N$  and  $BA$  with the Poisson attenuation model for correction of occlusions without the Relaskop sampling. However, in our analysis using ForeStereo data this method yields biased results when compared with HPC estimates. In contrast to TLS, where tree detection is better at the lower part of the stem, stem sections viewed under an inclination angle over the crown of more distant trees—seen against the sky—are most accurately detected in the hemispherical images. The Relaskop-based method selects trees depending on DBH, whereas the method based on image segmentation considers the diameter at the height corresponding to the inclination angle of view, making the latter preferable for the RGB photos acquired using ForeStereo. However, the Relaskop-based and Poisson attenuation model methods performance may be improved through the adjustment of BAF and  $D_E$ .

The results described in this work demonstrate the effectiveness of ForeStereo as a PS technology for field sampling in operational forest inventories. Cost analyses are beyond the scope of this study, but the performance capacity shown by ForeStereo in field surveys for this study—a team of two people surveyed 16 sampling points located on a systematic grid of  $400 \times 400$  m, covering 256 ha per day on average—enables increased sampling and cost optimization of the forest inventory field stage. Two stage sampling design, combining PS technologies and spatially explicit remotely sensed data, may improve the accuracy of inference estimations in forest inventories (Brosofske *et al.* 2014). Precise and unbiased estimators for plot level variables are still to be developed. The approaches tested in this work can be used to deal with bias, our results pointing to the distance-sampling using DBH as covariate and the HPC method proposed here as suitable approaches with ForeStereo data. Other sources of error affecting ForeStereo estimates—light conditions, stand density or species on image segmentation, or the limited accuracy of distance estimations in the proximity of the base line—are beyond the scope of this study and should be the subject of future research. As an alternative, remote sensing and PS data may be integrated during data processing; Korpela *et al.* (2007) combined photogrammetry and field triangulation for complete mapping of the stand, whereas Liang *et al.* (2016) suggested the use of TLS for retrieval of individual tree attributes and airborne remote sensing data to extend the estimation of tree attributes to all trees within the stand, which renders the estimation of stand-level summary statistics from TLS data unnecessary. Whichever approach is chosen, the next step is to implement these methods in user-friendly software packages—such as the ForeStereo software presented in Sánchez-González *et al.* (2016), which has been used for this study—so that these methods can be made available for foresters and stakeholders.

## Acknowledgments

The authors wish to thank Roberto Vallejo and the National Forest Inventory team of the Spanish Ministry of Agriculture, Fisheries, Food and Environment and Mancomunidad Forestal Ansó-Fago for their support with field data. This research has been funded by the National Parks Autonomous Agency of the Spanish Ministry of Agriculture, Fisheries, Food and

Environment through the project 979S/2010 of National Parks and the Spanish Ministry of Economy and Competitiveness through the project AGL2016-76769-C2-1-R.

## References

- Astrup, R., M. J. Ducey, A. Granhus, T. Ritter and Lüpke. 2014. Approaches for estimating stand-level volume using terrestrial laser scanning in a single-scan mode. *Canadian Journal of Forest Research* 44:666–676. doi: <http://dx.doi.org/10.1139/cjfr-2013-0535>.
- Bitterlich, W. 1947. Die Winkelzählmessung. *Allgemeine Forst- und Holzwirtschaftliche Zeitung* 58:94
- Bottalico, F., G. Chirici, R. Giannini, S. Mele, M. Mura, M. Puxeddu, R. E. McRoberts, R. Valbuena and D. Travaglini. 2017. Modeling Mediterranean forest structure using airborne laser scanning data. *International Journal of Applied Earth Observation* 57:145–153.
- Bouvier, M., S. Durrieu, R. A. Fournier and J.-P. Renaud. 2015. Generalizing predictive models of forest inventory attributes using an area-based approach with airborne LiDAR data. *Remote Sensing of Environment* 156:322–334.
- Brosofske, K. D. R. E. Froese, M. J. Falkowski and A. Banskota. 2014. A review of methods for mapping and prediction of inventory attributes for operational forest management. *Forest Science* 60:733–756. doi: <https://doi.org/10.5849/forsci.12-134>.
- Brunner, A. and B. Gizachew. 2014. Rapid detection of stand density tree positions and tree diameter with 2D terrestrial laser scanner. *European Journal of Forest Research* 133:819–831. doi: 10.1007/s10342-014-0799-1.
- Buckland, S. T., D. R. Anderson, K. P. Burnham, J. L. Laake, D. L. Borchers and L. Thomas. 2001. Introduction to distance-sampling: Estimating abundance of biological populations. Oxford, U.K.: Oxford University Press.
- Clark, N. A., R. H. Wynne, D. L. Schmoltdt and M. F. Winn. 2000. An assessment of the utility of a non-metric digital camera for measuring standing trees. *Computers and Electronics in Agriculture* 28:151–169. doi: 10.1016/S0168-1699(00)00125-3.
- Clark, R. G. 2016. Statistical efficiency in distance-sampling. *PLoS ONE* 11:e0149298. doi: 10.1371/journal.pone.0149298.
- Côté, J.-F., R. A. Fournier, G. W. Frazer and K. O. Niemann. 2012. A fine-scale architectural model of trees to enhance LiDAR-derived measurements of forest canopy structure. *Agricultural and Forest Meteorology* 166/167:72–85.
- Dassot, M., T. Constant and M. Fournier 2011. The use of terrestrial LIDAR technology in forest science: Application fields benefits and challenges. *Annals of Forest Science* 68:959–974.
- Ducey, M. J. and R. Astrup. 2014. Adjusting for nondetection in forest inventories derived from terrestrial laser scanning. *Canadian Journal of Remote Sensing* 39:410–425. doi: <http://pubs.casi.ca/doi/abs/10.5589/m13-048>.
- Forsman, M., N. Börlin and J. Holmgren. 2012. Estimation of tree stem attributes using terrestrial photogrammetry. Pages 261–265 of the *International Archives of the Photogrammetry Remote Sensing and Spatial Information Sciences, XXII ISPRS Congress*, held in Melbourne, Australia. .
- Garestier, F., P. Dubois-Fernández and I. Champion. 2008. Forest height inversion using high resolution P-band Pol-InSAR data. *IEEE Transactions on Geoscience and Remote Sensing* 46:3544–3559.
- Gea-Izquierdo, G., F. Montes, R. Gavilán, I. Cañellas and A. Rubio. 2015. Is this the end? Dynamics of a relict stand from pervasively deforested ancient Iberian pine forests. *European Journal of Forest Research* 134:525–536. doi: 10.1007/s10342-015-0869-z.
- Gómez, C., M. A. Wulder, F. Montes and J. A. Delgado. 2011. Forest structural diversity characterization in Mediterranean pines of central Spain with QuickBird-2 imagery and canonical correlation analysis. *Canadian Journal of Remote Sensing* 37:628–642. doi:10.5589/m12-005.

- Gómez, C. and D. Green. 2017. Small unmanned airborne systems to support oil and gas pipeline monitoring and mapping. *Arabian Journal of Geoscience* 10:202.
- Hafner, J., H. S. Sawhney, W. Equitz, M. Flickner and W. Niblack. 1995. Efficient color histogram indexing for Quadratic Form Distance functions. *IEEE Transactions on Pattern Analysis and Machine Intelligence* 17:729–736.
- Hauglin, M., T. Gobakken, R. Astrup, L. Ene and E. Næsset. 2014. Estimating single-tree crown biomass of Norway spruce by airborne laser scanning: A comparison of methods with and without the use of terrestrial laser scanning to obtain the ground reference data. *Forests* 5:384–403.
- Herrera, P. J., G. Pajares, M. Guijarro, J. J. Ruz and J. M. Cruz. 2011. A stereovision matching strategy for images captured with fish-eye lenses in forest environments. *Sensors* 11:1756–1783.
- Herrera, P. J., G. Pajares, M. Guijarro, J. J. Ruz, J. M. Cruz and F. Montes. 2009. A featured-based strategy for stereovision matching in sensors with fish-eye lenses for forest environments. *Sensors* 9:9468–9492.
- Hilker, T., M. A. Wulder and N. C. Coops. 2008. Update of forest inventory data with lidar and high spatial resolution satellite imagery. *Canadian Journal of Remote Sensing* 34:5–12.
- Holmgren J., Å. Persson and U. Söderman. 2008. Species identification of individual trees by combining high resolution LiDAR data with multi-spectral images. *International Journal of Remote Sensing* 29:1537–1552.
- Korpela, I., T. Tuomola and E. Välimäki. 2007. Mapping forest plots: An efficient method combining photogrammetry and field triangulation. *Silva Fennica* 41:457–469.
- Leberl, F., A. Irschara, T. Pock, P. Meixner, M. Gruber, S. Scholz and A. Wiechert. 2010. Point clouds: LiDAR versus three dimensional vision. *Photogrammetric Engineering and Remote Sensing* 76:1123–1134.
- Liang, X., V. Kankare, J. Hyypä, Y. Wang, A. Kukko, H. Haggrén, X. Yu, H. Kaartinen, A. Jaakkola, F. Guan, M. Holopainen and M. Vastaranta. 2016. Terrestrial laser scanning in forest inventories. *ISPRS Journal of Photogrammetry and Remote Sensing* 115:63–77. doi: <http://dx.doi.org/10.1016/j.isprsjprs.2016.01.006>.
- Lindberg, E., J. Holmgren, K. Olofsson and H. Olsson. 2012. Estimation of stem attributes using a combination of terrestrial and airborne laser scanning. *European Journal of Forest Research* 131 (6):1917–1931.
- Lovell, J. L., D. L. B. Jupp, D. S. Culvenor and N. C. Coops. 2003. Using airborne and ground-based ranging lidar to measure canopy structure in Australian forests. *Canadian Journal of Remote Sensing* 29:607–622. doi: 10.5589/m03-026.
- Lovell, J., D. B. L. Jupp, G. Newnham and D. Culvenor. 2011. Measuring tree stem diameters using intensity profiles from ground-based scanning Lidar from a fixed viewpoint. *ISPRS Journal of Photogrammetry and Remote Sensing* 66:46–55. doi: 10.1016/j.isprsjprs.2010.08.006.
- Magnussen, S., E. Næsset and T. Gobakken. 2013. Prediction of tree size distributions and inventory variables from cumulants of canopy height distributions. *Forestry* 86:583–595.
- Maltamo, M., H. O. Ørka, O. M. Bollandssås, T. Gobakken and E. Næsset. 2015. Using pre-classification to improve the accuracy of species-specific forest attribute estimates from airborne laser scanner data and aerial images. *Scandinavian Journal of Forest Research* 30:336–345.
- Manfreda, S., M. F. McCabe, P. E. Miller, R. Lucas, V. Pajuelo-Madrigal, G. Mallinis, E. Ben-Dor, D. Helman, L. Estes, G. Ciruolo, J. Müllerová, F. Tauro, M. I. de Lima, J. L. M. P. de Lima, A. Maltese, F. Frances, K. Cylor, M. Kohv, M. Perks, G. Ruiz-Pérez, Z. Su, G. Vico and B. Toth. 2018. On the use of unmanned aerial systems for environmental monitoring. *Remote Sensing* 10:641.
- Mandallaz, D. and R. Ye. 1999. Forest inventory with optimal two-phase two-stage sampling schemes based on the anticipated variance. *Canadian Journal of Forest Research* 29:1691–1708.
- Marino, E., F. Montes, J. L. Tomé, J. A. Navarro and C. Hernando. 2018. Vertical forest structure analysis for wildfire prevention: Comparing airborne laser scanning data and stereoscopic hemispherical images. *International Journal of Applied Earth Observation and Geoinformation* 73:438–449.
- Marques, F. F. C. and S. T. Buckland. 2003. Incorporating covariates into standard line transect analyses. *Biometrics* 59:924–935. doi: 10.1111/j.0006-341X.2003.00107.x.
- Matasci, G., T. Hermosilla, M. A. Wulder, J. C. White, N. C. Coops, J. W. Hobart, D. Bolton, P. Tompalski and C. W. Bater. 2018. Three decades of forest structural dynamics over Canada's forested ecosystems using Landsat time-series and Lidar plots. *Remote Sensing of Environment* 216:697–714.
- Miller, D. L. and L. Thomas. 2015. Mixture models for distance detection functions. *PLoS ONE* 10:e0118726. doi: 10.1371/journal.pone0118726.
- Montes, F., A. Ledo, A. Rubio, P. Pita and I. Cañellas. 2009. Use of stereoscopic hemispherical images for forest inventories. In *90th anniversary of the Forestry Faculty in Prague, Forest Wildlife and Wood Sciences for Society Development*, held in Prague, Czech Republic, 16–18 April 2009. Edited by R., Z., E. and M. Prague, Czech Republic: Czech University of Life Sciences. ISBN: 978-80-213-2019-2.
- Morsdorf, F., B. Kotz, E. Meier, K. I. Itten and B. Allgower. 2006. Estimation of LAI and fractional cover from small footprint airborne laser scanning data based on gap fraction. *Remote Sensing of Environment* 104: 50–61.
- Næsset, E. 2002. Predicting forest stand characteristics with airborne scanning laser using a practical two-stage procedure and field data. *Remote Sensing of Environment* 80:88–99.
- Næsset, E. and T. Gobakken. 2008. Estimation of above- and belowground biomass across regions of the boreal forest zone using airborne laser. *Remote Sensing of Environment* 112:3079–3090. doi:10.1016/j.rse.2008.03.004.
- Newnham, G. J., J. D. Armston, K. Calders, M. I. Disney, J. L. Lovell, C. B. Schaaf, A. H. Strahler and F. M. Danson. 2015. Terrestrial laser scanning for plot-scale forest measurement. *Current Forestry Reports* 1:239–251. doi:10.1007/s40725-015-0025-5.
- Pimont, F., J-L. Dupuy, E. Rigolot, V. Prat and A. Piboule. 2015. Estimating leaf bulk density distribution in a tree canopy using terrestrial LiDAR and a straightforward calibration procedure. *Remote Sensing* 7:7995–8018.
- Pueschel, P., H. Buddenbaum and J. Hill. 2012. An efficient approach to standardizing the processing of hemispherical images for the estimation of forest structural attributes. *Agricultural and Forest Meteorology* 160:1–13.
- Puttonen, E., J. Suomalainen, T. Hakala, E. Räikkönen, H. Kaartinen, S. Kaasalainen and P. Litkey. 2010. Tree species classification from fused active hyperspectral reflectance and LIDAR measurements. *Forest Ecology and Management* 10:1843–1852.
- Qi, W., Lee, S. Hancock, S. Luthcke, H. Tang, J. Armston and R. Dubayah. 2019. Improved forest height estimation by fusion of simulated GEDI Lidar data and TanDEM-X InSAR data. *Remote Sensing of Environment* 221:621–634.
- Raumonen, P., M. Kaasalainen, M. Åkerblom, S. Kaasalainen, H. Kaartinen, M. Vastaranta, M. Holopainen, M. Disney and P. Lewis. 2013. Fast automatic precision tree models from terrestrial laser scanner data. *Remote Sensing* 5:491–520.
- Ringdahl, O., P. Hohnloser, T. Hellström, J. Holmgren and O. Lindroos. 2013. Enhanced algorithms for estimating tree trunk diameter using 2D laser scanner. *Remote Sensing* 5:4839–4856. doi: 10.3390/rs5104839.
- Rodríguez-García, C., F. Montes, F. Ruiz, I. Cañellas and P. Pita. 2014. Stem mapping and estimating standing volume from stereoscopic hemispherical images. *European Journal of Forest Research* 133:895–904.
- Rubio-Cuadrado, A., J. J. Camarero, M. del Río, M. Sánchez-González, R. Ruiz-Peinado, A. Bravo-Oviedo, L. Gil and F. Montes. 2018a. Drought modifies tree competitiveness in an oak-beech temperate forest. *Forest Ecology and Management* 429:7–17. doi: 10.1016/j.foreco.2018.06.035.

- Rubio-Cuadrado, A., J. Camarero, R. Aspizua, M. Sánchez-González, L. Gil and F. Montes. 2018b. Abiotic factors modulate post-drought growth resilience of Scots pine plantations and rear-edge Scots pine and oak forests. *Dendrochronologia*. doi: 10.1016/j.dendro.2018.08.001.
- Sánchez-González, M., M. Cabrera, P. J. Herrera, R. Vallejo, I. Cañellas and F. Montes. 2016. Basal area and diameter distribution estimation using stereoscopic hemispherical images. *Photogrammetric Engineering and Remote Sensing (PE&RS)* 82:605–616. doi: 10.14358/PERS.82.8.605.
- Sangüesa-Barreda, G., J. Camarero, J. Oliva, F. Montes and A. Gazol. 2015. Past logging drought and pathogens interact and contribute to forest dieback. *Agricultural and Forest Meteorology* 208:85–9. doi: 10.1016/j.agrformet.2015.04.011.
- Santoro, M. and O. Cartus. 2018. Research pathways of forest above-ground biomass estimation based on SAR backscatter and interferometric SAR observations. *Remote Sensing* 10:608.
- Seidel, D., S. Fleck and C. Leuschner. 2012. Analyzing forest canopies with ground-based laser scanning: A comparison with hemispherical photography. *Agricultural and Forest Meteorology* 154–155:1–8.
- Seidel, D. and C. Ammer. 2014. Efficient measurements of basal area in short rotation forests based on terrestrial laser scanning under special consideration of shadowing. *IForest—Biogeosciences and Forestry* 7:227–232.
- St-Onge, B., Audet and J. Bégin. 2015. Characterizing the height structure and composition of a boreal forest using an individual tree crown approach applied to photogrammetric point clouds. *Forests* 6:3899–3922.
- Strahler, A.H., D. B. L. Jupp, C. E. Woodcock, C. B. Schaaf, T. Yao, F. Zhao, X. Yang, J. Lovell, D. Culvenor, G. Newnham, W. Ni-Meister and W. Boykin-Morris. 2008. Retrieval of forest structural parameters using a ground-based Lidar instrument (Echidna®). *Canadian Journal of Remote Sensing* 34(S2):S426–S440.
- Tebaldini, S. and F. Rocca. 2012. Multibaseline polarimetric SAR tomography of a boreal forest at P- and L-bands. *IEEE Transactions on Geoscience and Remote Sensing* 50:232–246.
- Tomppo, E., H. Olsson, G. Stahl, M. Nilsson, O. Hagner and M. Katila. 2008. Combining national forest inventory field plots and remote sensing data for forest databases. *Remote Sensing of Environment* 112:1982–1999. doi: 10.1016/j.rse.2007.03.032.
- Tuominen, S., R. Näsi, E. Honkavaara, A. Balazs, T. Hakala, N. Viljanen, I. Pölönen, H. Saari and H. Ojanen. 2018. Assessment of classifiers and remote sensing features of hyperspectral imagery and stereo-photogrammetric point clouds for recognition of tree species in a forest area of high species diversity. *Remote Sensing* 10:714.
- Valbuena, R., M. Maltamo, S. Martín-Fernández, P. Packalen, C. Pascual and G.-J. Nabuurs. 2013. Patterns of covariance between airborne laser scanning metrics and Lorenz curve descriptors of tree size inequality. *Canadian Journal of Remote Sensing* 39:18–31.
- Varjo, J., H. Henttonen, J. Lappi, J. Heikkonen and J. Juujärvi. 2006. Digital horizontal tree measurements for forest inventory. *Working Papers of the Finnish Forest Research Institute* 40, Finnish Forest Research Institute Helsinki. ISSN 1795-150X.
- Vauhkonen, J., L. Mehtätalo and P. Packalén. 2011. Combining tree height samples by airborne laser scanning and stand management records to estimate plot volume in Eucalyptus plantations. *Canadian Journal of Forest Research* 41:1649–1658.
- White, J. C., M. A. Wulder, M. Vastaranta, N. C. Coops, D. Pitt and M. Woods. 2013. The utility of image-based point clouds for forest inventory: A comparison with airborne laser scanning. *Forests* 4:518–536.
- White, J. C., N. C. Coops, M. A. Wulder, M. Vastaranta, T. Hilker and P. Tompalski. 2016. Remote sensing technologies for enhancing forest inventories: A review. *Canadian Journal of Remote Sensing* 42(5):619–641. doi: 10.1080/07038992.2016.1207484.
- White, J. C., M. A. Wulder, T. Hermosilla, N. C. Coops and G. W. Hobart. 2017. A nationwide characterization of 25 years of forest disturbance and recovery for Canada using Landsat time series. *Remote Sensing of Environment* 194:303–321.
- Wulder, M. A., N. C. Coops, A. T. Hudak, F. Morsdorf, R. Nelson, G. Newnham and M. Vastaranta. 2013. Status and prospects for LiDAR remote sensing of forested ecosystems. *Canadian Journal of Remote Sensing* 39:1–5.
- Yang, X., A. H. Strahler, C. B. Schaaf, D. L. B. Jupp, T. Yao, F. Zhao, Z. Wang, D. S. Culvenor, G. J. Newnham, J. L. Lovell, R. O. Dubayah, C. E. Woodcock and W. Ni-Meister. 2013. Three-dimensional forest reconstruction and structural parameter retrievals using a terrestrial full-waveform lidar instrument (Echidna®). *Remote Sensing of Environment* 135:36–51. doi: 10.1016/j.rse.2013.03.020.
- Yao, T., X. Yang, F. Zhao, Z. Wang, Q. Zhang, D. B. L. Jupp, J. Lovell, D. Culvenor, G. Newnham, W. Ni-Meister, C. B. Schaaf, C. E. Woodcock, J. Wang, X. Li and A. H. Strahler. 2011. Measuring forest structure and biomass in New England forest stands using Echidna ground-based Lidar. *Remote Sensing of Environment* 115:2965–2974.
- Zhao, Y., Y. Zeng, Z. Zheng, W. Dong, D. Zhao, B. Wu and Q. Zhao. 2018. Forest species diversity mapping using airborne LiDAR and hyperspectral data in a subtropical forest in China. *Remote Sensing of Environment* 213:104–114.

# A Novel Method for Separating Woody and Herbaceous Time Series

Qiang Zhou, Shuguang Liu, and Michael J Hill

## Abstract

Mapping the spatial distribution of woody and herbaceous vegetation in high temporal resolution in savannas would be beneficial for modeling interrelationships between trees and grasses, and monitoring fuel loads and biomass for livestock. In this study, we developed a frequency decomposition method to separate woody and herbaceous vegetation components using Normalized Difference Vegetation Index (NDVI) time series. The results were validated using fractional cover data derived from high-resolution images. The validation revealed a close relationship between our decomposed NDVI and corresponding fractional cover ( $R^2 = 0.55$  and  $0.64$  for woody and herbaceous components, respectively). We examined the spatial and temporal patterns of the decomposed NDVI, where woody and herbaceous NDVI showed different responses to precipitation. The methods proposed in this study can be used to separate the woody and herbaceous NDVI time series as an alternative approach for monitoring woody and herbaceous vegetation interrelationships related to climatic drivers.

## Introduction

Savannas provide essential ecosystem services to environments and societies, including supporting the subsistence economy, climate regulation, biodiversity, water balance, and hydrodynamics (Seghieri *et al.* 1995; Guerschman *et al.* 2009). On the other hand, savannas are very dynamic ecosystems under the influences of various forces, including climate variability and change, fire, herbivory, and land use change (Verbesselt *et al.* 2006; Verbesselt *et al.* 2007; Coetsee *et al.* 2010; Sankaran *et al.* 2005; Bucini and Hanan 2007; Staver *et al.* 2011; Gessner *et al.* 2013). The mosaics of woody canopy and herbaceous cover of savannas form a distinct vegetation structure and, separately and together, they provide various essential functions to the ecosystem (e.g., carbon sequestration, wildfire ignition, and biodiversity conservation) to human livelihoods (e.g., grazing, fuelwood, and agriculture) (Gessner *et al.* 2013). Thus, mapping the spatial and temporal changes of the relative abundance and phenology of the woody and herbaceous components in highly dynamic savannas is critical for further understanding the impacts of climate change, land use, and disturbances on ecosystem structures

Qiang Zhou and Michael J Hill are with the Department of Earth System Science and Policy, University of North Dakota, 4149 University Avenue, Grand Forks, ND, 58202.

Shuguang Liu is with the National Engineering Laboratory of Forest Ecology and Applied Technology in South China, and Faculty of Life Science and Technology, Central South University of Forestry and Technology, Changsha 410004, Hunan, China.

Michael J Hill is also with the School of the Environment, Flinders University, Bedford Park, SA, 5042, Australia.

Qiang Zhou is also with the U.S. Geological Survey Earth Resources Observation and Science (EROS) Center, 47914 252nd Street, Sioux Falls, SD 57198.

and services including wildlife habitats, productivity, and biogeochemical cycles (Kahiu and Hanan 2018). In addition, understanding the dynamics of these structural variables provides the basis for effective management decisions over extensive and heterogeneous savanna regions (Knoop and Walker 1985; Bucini and Hanan 2007; Sankaran *et al.* 2008).

Separating the woody and herbaceous components over large areas remains a challenge due to the similarity of the seasonal variation between the two components. Remote sensing technology has been the primary tool to investigate phenological dynamics of evergreen (or semideciduous) woody and seasonal herbaceous components (Lu *et al.* 2003; Donohue *et al.* 2009; Helman *et al.* 2015; Zhou *et al.* 2016). Various approaches have been proposed to decompose time series of satellite-derived vegetation signals. For example, Lu *et al.* (2003) separated 10-day evergreen woody and seasonal herbaceous time series in Australia using the Normalized Difference Vegetation Index (NDVI) from the Advanced Very High-Resolution Radiometer (AVHRR) dataset, by applying empirical relationships between evergreen woody and herbaceous seasonal variations. Helman *et al.* (2015) used the dry season NDVI to extract the evergreen woody component and then used the wet season NDVI to estimate the seasonal herbaceous component from the Moderate Resolution Imaging Spectroradiometer (MODIS). Both studies used a constant NDVI to reduce the soil background influence. However, these methods cannot distinguish between woody deciduous and seasonal herbaceous vegetation components. Woody vegetation with varying degrees of deciduousness is prevalent in southern African savannas such as the Mopane woodlands and Kalahai Acacia-Baikiaea woodlands. Moreover, the diverse species of woody vegetation exhibit wide variation in intra-seasonal phenology and canopy morphology and density, which makes the separation from the herbaceous signal more challenging.

A range of techniques have been applied to extract vegetation phenology dynamics from remote sensing time series. Seasonal and Trend decomposition using Loess (STL) (seasonal decomposition of time series by LOcally wEighted Scatterplot Smoothing (LOESS)) was used to separate seasonal component from multi-year trends based on the LOESS methods (Cleveland *et al.* 1990). The harmonic analysis of NDVI time series (Mentoni *et al.* 1993) was used to smooth data (Jun *et al.* 2004), correlate responses with climatic variables (Lhermitte *et al.* 2008; Roerink *et al.* 2003; Bradley *et al.* 2011), extract vegetation phenology information (Leinenkugel *et al.* 2013), and classify vegetation types with distinct phenology (Jakubauskas *et al.* 2002; Yui *et al.* 2004; Geerken *et al.* 2005). In the harmonic analysis, the first two harmonics were used mostly in vegetation phenology studies: The amplitude of the first harmonic was associated with the dominance of annual vegetation species, the amplitude of the second harmonic indicated the

Photogrammetric Engineering & Remote Sensing  
Vol. 85, No. 7, July 2019, pp. 509–520.  
0099-1112/19/509–520

© 2019 American Society for Photogrammetry  
and Remote Sensing  
doi: 10.14358/PERS.85.7.509

mixture of woody and herbaceous vegetation, and the phase of the harmonic suggested the timing of leaf-on (Moody and Johnson 2001). Although harmonics have been used to extract and classify phenology information, to our knowledge, they have not been used to separate phenological dynamics of woody and herbaceous vegetation components in African savannas.

This paper aims to (1) develop a new approach based on harmonic analysis to separate the deciduous woody and herbaceous phenological dynamics in savanna area, and (2) apply the method to map the spatial and temporal changes of vegetation components in southern Africa. Deciduous woody and herbaceous covers have different timings of green-up and senescence in southern Africa (Archibald and Scholes 2007). For example, woody vegetation flushes its leaves right before the rainy season, while herbaceous vegetation does not grow leaves until the rainy season starts (Higgins *et al.* 2011). The phenological difference leads to distinct seasonal NDVI characteristics for woody and herbaceous covers, which can be captured by frequency components in the harmonic analysis. Our science questions are: (1) Can the new approach developed in this study be used to characterize the compositional phenology changes of savanna (using southern African savanna as a case study)? (2) What are the spatial and temporal dynamics of the phenology patterns of the woody and herbaceous components in southern African savanna? (3) How does climatic variation drive the phenological patterns?

## Study Area

The study area covers portions of Angola, Zambia, Zimbabwe, Namibia, and Botswana of southern Africa, lying between 10°52'23"S and 21°44'44"S and between 15°59'24"E and 26°58'52"E. The area covers approximately 1 450 000 km<sup>2</sup> with a mean minimum and maximum temperature range from 9°C to 27°C, and annual precipitation from 1500 to 291 mm (Hijmans *et al.* 2005). From north to south, the vegetation shifts from woodlands and open deciduous forests to arid shrubland (Cowling *et al.* 2004). Three types of woody canopy are found in the study area: 1) Miombo is covered by a dense canopy that is mostly broad leaf evergreen but with a short partially deciduous period (Fuller 1999; Chidumayo 2002; Richer 2008; Vancutsem *et al.* 2009); 2) Mopane is mostly covered by broad leaf deciduous, but more mixed in density (Fuller 1999; Veenendaal *et al.* 2008); and 3) Kalahari is mostly deciduous forest, varying from a heterogeneous mixture of open woodland savannas (Burkeo-Pterocarpetea) to shrublands (Acaciete, Strohbach and Petersen 2007; Gessner *et al.* 2009). The study area consists of eight ecoregions (Table 1) defined by the Terrestrial Ecoregions of the World (Figure 1) (Olson *et al.* 2001). Nonsavanna ecoregions (Etosha Pan halophytics, Western Zambebian grasslands, Zambebian Cryptosepalum dry forests, Zambebian flooded grasslands, and Zambebian halophytics) are excluded in this study. The land

use and grazing intensity across the study region is shown in Figure 2a. The map shows that the the drier grassy savanna types are grazed whilst the wetter denser woody savannas of the Miombo woodlands are largely ungrazed. The precipitation that drives growth across the study region exhibits a very strong latitudinal gradient declining markedly from north to south (Figure 2b).

## Material and Methods

The MODIS eight-day 500 m Bidirectional Reflectance Distribution Function (BRDF)-adjusted reflectance product (MCD43A4) (Schaaf *et al.* 2002, 2010) from January 2002 to December 2011 was acquired for the study area. The NDVI time series was derived from the red band (620–670 nm) and near-infrared band (841–876 nm). The MODIS observations often contain noise due to clouds, cloud shadows, and other artificial sources, which creates false high or low values in the NDVI time series (Lunetta *et al.* 2006; Shao *et al.* 2016). In this study, we detected the noise using the quality assurance layer within the MODIS reflectance product, which labeled it as “not good quality”. Additionally, we detected the noises using a moving window differencing filter, which calculated the difference between the current observation and the observation at the previous time step (Lu *et al.* 2003; Zhou *et al.* 2016; Hill *et al.* 2016). The detected noise was removed from the time series and replaced by applying the spline interpolation (Zhou *et al.* 2016). We chose the 500 m MODIS dataset because our research project included a separate study on separation of photosynthetic vegetation, nonphotosynthetic vegetation, and bare soil, which required short-wave infrared (SWIR) bands that were not available in the finer resolution 250 m dataset.

## Frequency Decomposition

We propose a frequency decomposition method to separate the seasonal time series variation of a mixed pixel into woody and herbaceous variation (Figure 3). Time series can be represented by a sequence of regular frequencies according to a standard Fourier transform (Bracewell 1965):

$$X_k = \sum_{n=0}^{N-1} x_n \cdot e^{-\frac{2\pi i}{N} kn} \quad k = 0, \dots, N-1 \quad (1)$$

where  $N$  is the total sample size (e.g.,  $N = 460$  for the eight-day composites from 2002 to 2011),  $k$  is the number of cycles.  $k/N$  is the frequency (e.g.,  $n = 10, 20, 30$  represents once a year, twice a year, and three times a year in this study),  $x_n$  is the  $n$ th value of time series, and  $X_k$  is a complex number that represents the amplitude and phase at the given frequency. In this study, we use a subset range of frequencies to represent the seasonal vegetation variation.

Table 1. Characteristics of African savanna ecoregions.

Ecoregion	Annual Rainfall (mm)	Tree Genus and Species	Grass Genus and Species
Angolan Miombo (ER1)	641–1472	<i>Brachystegia</i> ; <i>Isoberlinia</i> ;	<i>Loudetia</i> ; <i>Hyparrhenia</i> ;
Central Zambebian Miombo (ER2)	667–1503	<i>Julbernardia</i> spp.	<i>Tristachya</i> spp.
Southern Miombo (ER3)	605–832		
Zambebian & Mopane (ER4)	847–922	<i>Colophospermum mopane</i> ;	<i>Aristida</i> ; <i>Digitaria</i> ; <i>Erarostis</i> ;
Angolan Mopane (ER5)	310–730	<i>Combretum</i> ; <i>Acacia</i> ; <i>Kirkia</i> spp.	<i>Echinochloa</i> spp.
Southern Africa Bushveld (ER6)	336–844	<i>C. mopane</i> ; <i>Acacias</i> ;	<i>Hyparrhenia</i> spp.
Zambebian Baikiaea (ER7)	459–1027	<i>Terminalia</i> spp. <i>Burkea</i> spp.	<i>Sparse grasses</i>
Kalahari Acacia-Baikiaea (ER8)	298–594	<i>Lonchocarpus</i> ; <i>Terminalia</i> ; <i>Burkea</i> ;	<i>Aristida</i> ; <i>Eragrostis</i> ;
		<i>Combretum</i> ; <i>Grewia</i> ; <i>Acacia</i> ;	<i>Heteropogon</i> ;
		<i>Commiphora</i> spp.	<i>Digitaria</i> spp.

\*Data source: Vegetation species: Burgess *et al.* (2004); Hill *et al.* (2011). Rainfall: Hijmans *et al.* (2005).

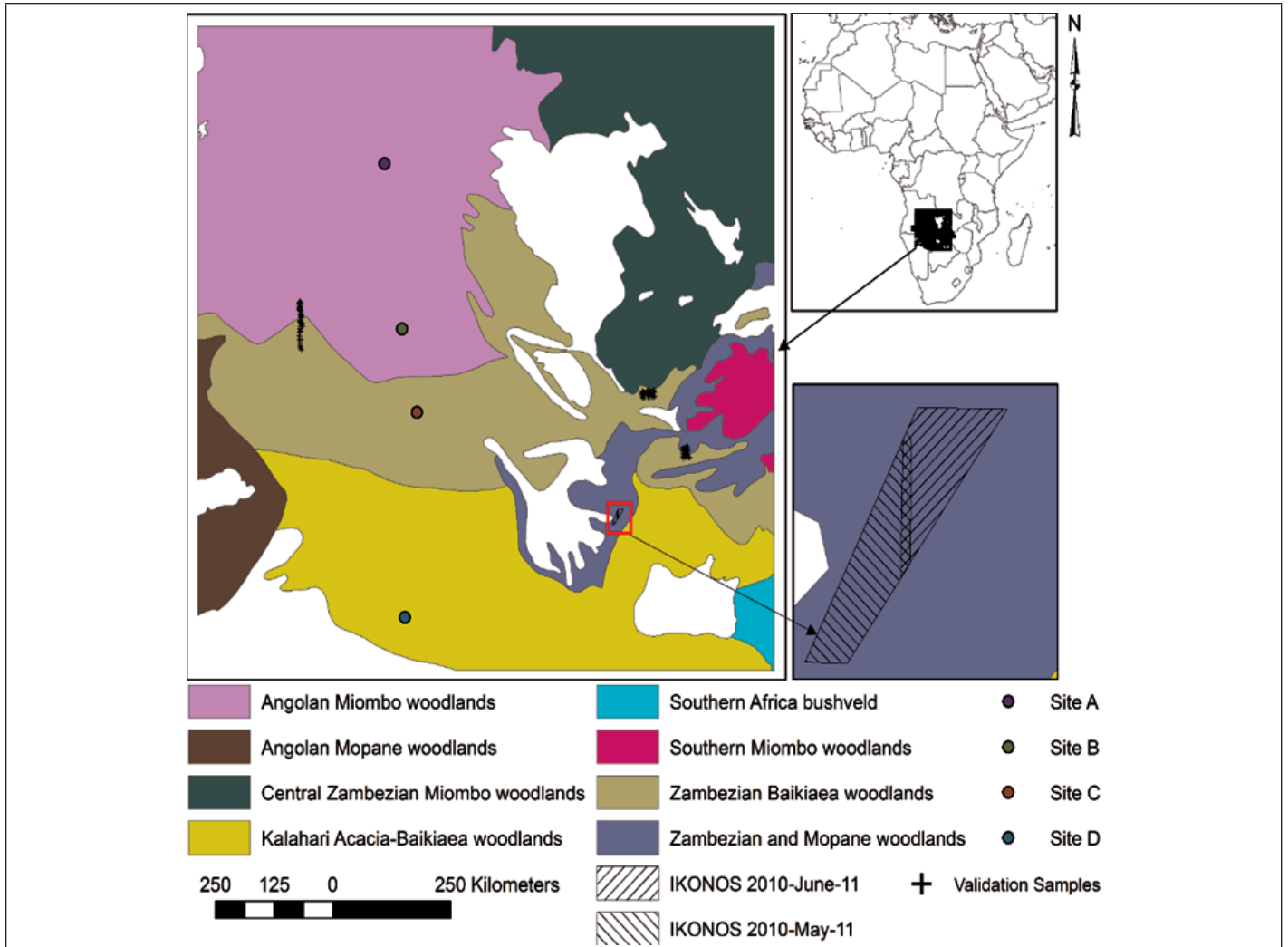


Figure 1. Southern African savanna ecosystems defined by Olson *et al.* (2001). Nonsavanna (white) ecoregions are masked out. The black crosses are validation sites based on Google Earth data. The zoom in panel shows the extents of two IKONOS images within the red box.

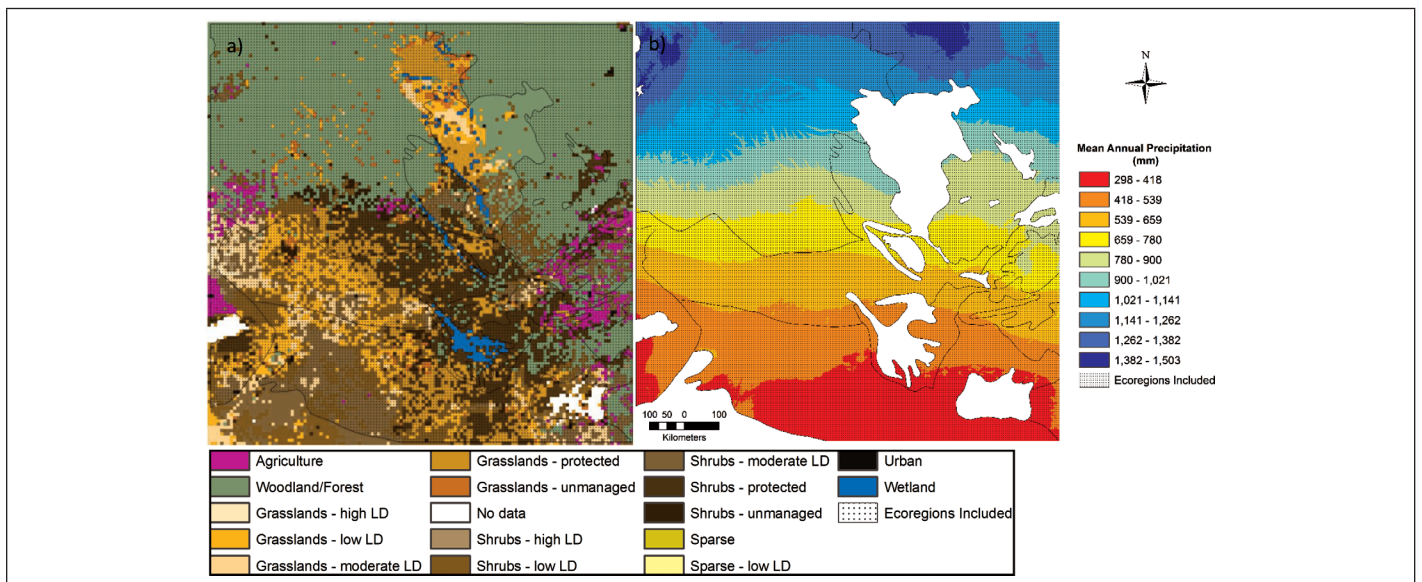


Figure 2. a) FAO Land Use characteristics including indications of livestock density (LD) (FAO/ISRIC 2003); and b) Mean annual precipitation (1950–2000) in the Africa savanna from WorldClim—Global Climate Data (Hijmans *et al.* 2005).

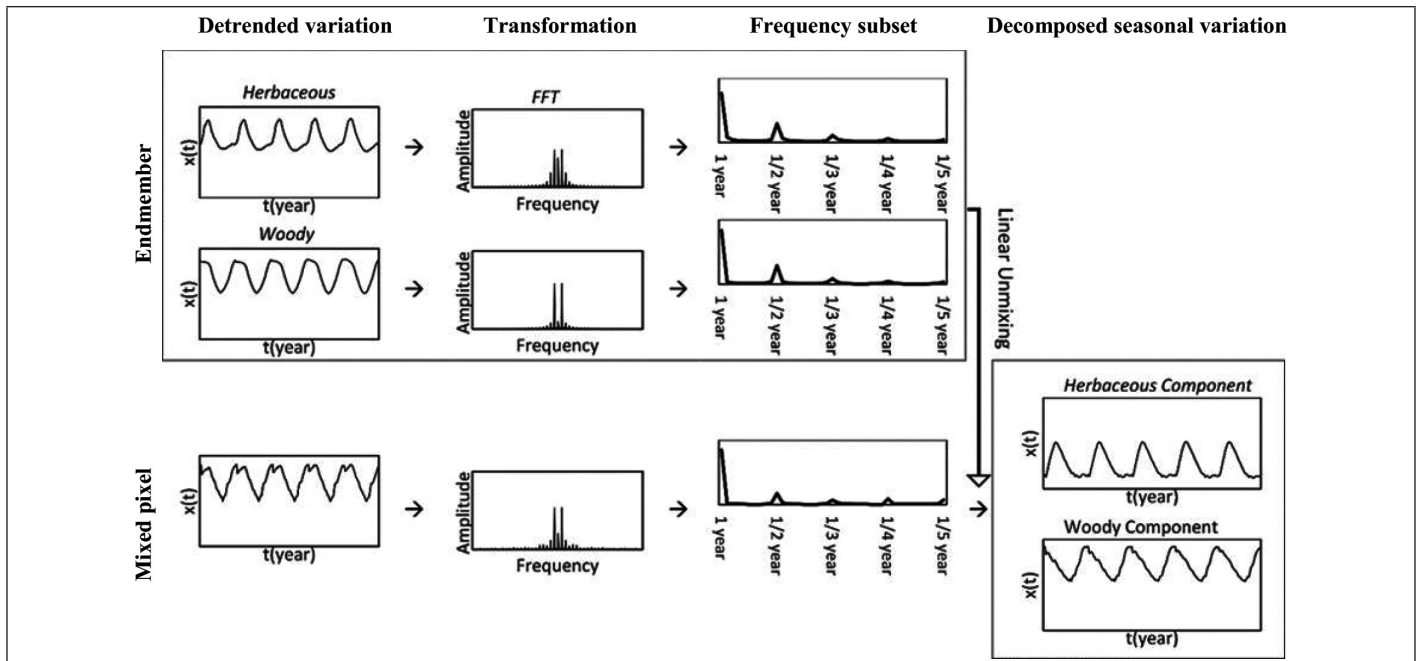


Figure 3. Schematic illustrating the approach for frequency decomposition. The detrended variation represents NDVI time series with multi-year trend removed. After Fourier transform, a frequency subset is used to represent the seasonal variation. The decomposed seasonal variation represents the estimated contribution of endmember components within the mixed pixel.

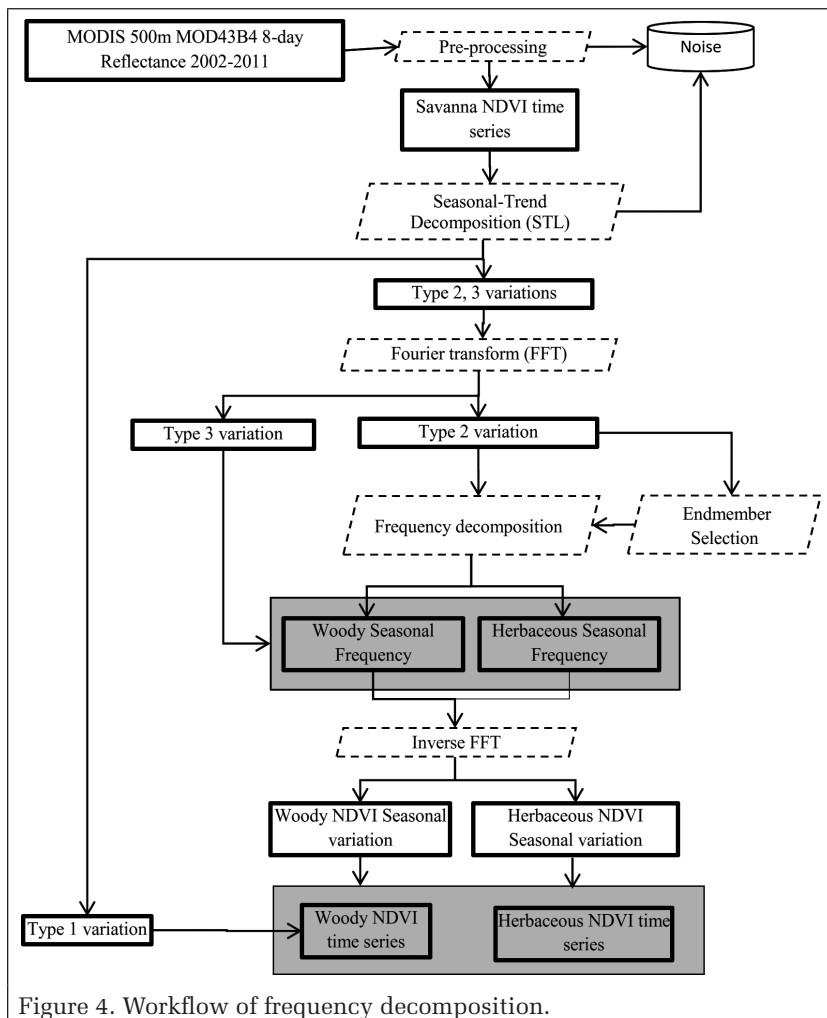


Figure 4. Workflow of frequency decomposition.

The frequency sequence of the mixed pixel can be decomposed into frequency sequences of endmembers (i.e., pure herbaceous and woody vegetation; selection method is described the section “Selection of Endmembers”) based on the linearity of the Fourier transform:

$$F(c_1V_1 + c_2V_2) = c_1F(V_1) + c_2F(V_2) \quad (2)$$

where  $V_1$  and  $V_2$  represent the time series of two endmembers, function  $F$  represents the Fourier transform, and  $c_1$  and  $c_2$  are complex numbers. The phases of  $c_1$  and  $c_2$  represent the temporal shift compared to the variables  $V_1$  and  $V_2$ , and the amplitude of  $c_1$  and  $c_2$  shows the amount of  $V_1$  and  $V_2$  in the mixed pixel time series.

The frequency decomposition intends to separate woody and herbaceous vegetation seasonal variation. However, we assume that the NDVI time series contains three types of variations. Type 1 is the baseline variation from semideciduous woody vegetation (typically when photosynthetically-active herbaceous vegetation is absent during dry seasons) and soil background information. Type 2 are the seasonal variations from both herbaceous and woody vegetation that are related to climate. Type 3 is the short-term variation from herbaceous and woody vegetation caused by local environment and weather variations. The type 3 variation can introduce uncertainties to the frequency decomposition, because the same woody and herbaceous combination may have different local environment and weather variations at various regions. Therefore, only type 2 is used to decompose the woody and herbaceous variation, while types 1 and 3 are integrated into the time series after the decomposition. Previous studies showed that the NDVI variation mostly comes from green woody and green herbaceous vegetation while the

soil background information is minor, and a constant low NDVI value was often used to represent the background information (Lu *et al.* 2003; Helman *et al.* 2015). Accordingly, we used a constant value of 0.1 to represent the background contribution based on another study in our study area (Hill *et al.* 2016). The constant value was subtracted from the type 1 variation. The detailed procedure of the frequency decomposition consists of five steps (Figure 4).

**Step 1: Retrieve type 1 variation.** The type 1 variation is retrieved from the NDVI time series using the statistical method STL (Cleveland *et al.* 1990). We also considered using the Fourier transform to retrieve type 1 variation and remove noise. But then we had to determine an arbitrary frequency threshold for noise and long-term variation, which could be controversial for this high temporal resolution dataset. One the other hand, STL is a popular method for decomposing time series, and outputs trend component and seasonal component. The trend component is equivalent to the type 1 variation that is added to the woody variation after the frequency decomposition. The seasonal component, however, contains both type 2 and 3 variations as defined in this study.

**Step 2: Separate type 2 and 3 variations.** The seasonal component from the STL is converted to a sequence of frequencies. By comparing the amplitude distribution of frequency

sequence (Figure 3), we assume that frequencies from 1–5 cycles per year have most of the seasonal component information and enough variation to determine the regression coefficients. So, we use frequencies from 1–5 cycles to represent type 2 variation and higher frequencies to represent type 3 variation. A multi-frequency combination of one cycle per year (red), two cycles per year (green), and three cycles per year (blue) is shown in Figure 5. The type 3 variation is restored after the decomposition at Step 4.

**Step 3: Build frequency decomposition model.** The coefficients  $c_1$  and  $c_2$  of woody and herbaceous components are estimated using the type 2 frequencies of mixed pixels based on Equation 2. Common to both regular linear endmember analysis and frequency decomposition is the likelihood of deriving negative fractions. In time series analysis, the derived unrealistic results show high NDVI in dry seasons and low NDVI in rainy seasons. Correspondingly, distinctive phase differences would occur at the annual frequency between the mixed pixel and the derived fractions. To avoid the occurrence of unrealistic fractions, an annual phase difference threshold between the original time series and the decomposed time series was used in this study. If the phase difference surpassed the threshold, the corresponding coefficient  $c_1$  or  $c_2$  was set to zero. After a systematic test using different time intervals, this study used a one-month difference as the threshold.

**Step 4: Restore type 3 variation.** The type 3 variation is assigned back to woody and herbaceous components based on the amplitudes of  $c_1$  and  $c_2$ :

$$F(V) = c_1 F_s(V_1) + \frac{abs(c_1)}{abs(c_1) + abs(c_2)} F_h(V) \quad (3)$$

where  $F_s(V_1)$  is the seasonal frequencies of the woody endmember, and  $c_1 F_s(V_1)$  is the derived seasonal frequencies of woody components.  $F_h(V)$  is the short-term signal from the mixed pixel, while  $F(V)$  is the derived full woody frequency sequence of the mixed pixel. The full herbaceous frequency sequence is assembled in the same way.

**Step 5: Construct separate time series for herbaceous and woody vegetation.** The full woody and herbaceous frequency sequences are transformed to NDVI time series of herbaceous and woody components. The type 1 variation is added to the woody time series. The final outputs are woody and herbaceous eight-day NDVI time series from 2002 to 2011.

### Selection of Endmembers

The seasonal frequencies (from step 2) are used to find pure woody and herbaceous pixels across the whole study area. Unsupervised classification is first applied to the seasonal frequencies dataset using the Iterative Self-Organizing Data Analysis Technique. The classification divides the dataset into 100 groups. Pure woody and herbaceous classes are then determined by comparing pixels within each class to the Google Earth images. A total number of 11 390 and 6616 relatively pure woody and herbaceous pixels, respectively, are selected. The endmembers were calculated by averaging woody or herbaceous time series from multiple pure pixels, which aimed to represent the general seasonal variation of various species

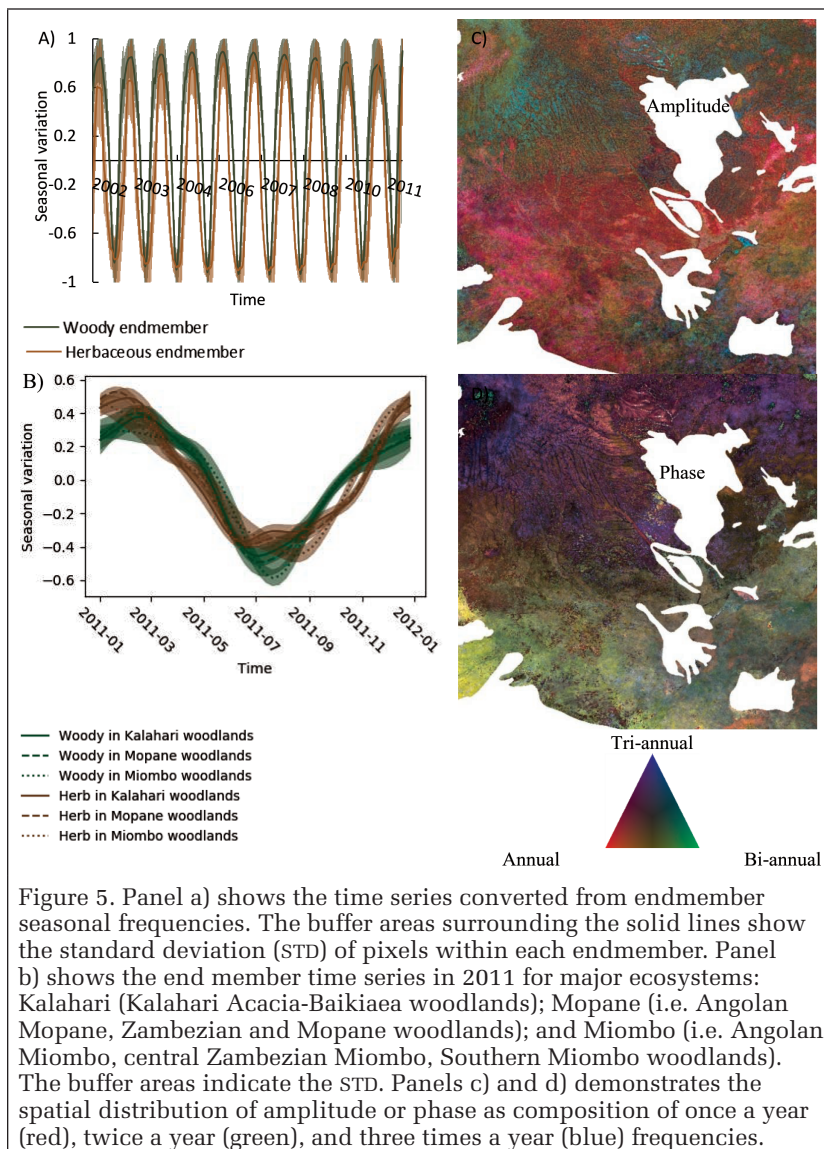


Figure 5. Panel a) shows the time series converted from endmember seasonal frequencies. The buffer areas surrounding the solid lines show the standard deviation (STD) of pixels within each endmember. Panel b) shows the end member time series in 2011 for major ecosystems: Kalahari (Kalahari Acacia-Baikiaea woodlands); Mopane (i.e. Angolan Mopane, Zambebian and Mopane woodlands); and Miombo (i.e. Angolan Miombo, central Zambebian Miombo, Southern Miombo woodlands). The buffer areas indicate the STD. Panels c) and d) demonstrates the spatial distribution of amplitude or phase as composition of once a year (red), twice a year (green), and three times a year (blue) frequencies.

across the study area (Figure 5a). The ecosystem-based end-member time series exhibits the spatial variation of the two endmembers. Although the woody or herbaceous vegetation have some variation across ecosystems, the two endmembers are still distinct from each other. In general, the woody endmember has steeper increase, starts earlier (in September), remains high longer (until May), and declines later than the herbaceous endmember (Figure 5b).

**Validation of the Derived Products**

Verifying the method using ground observations was not practical since measurements of woody and herbaceous canopy cover, leaf area index, or NDVI were not available at a suitable scale for comparison. However, we were able to validate the method using three approaches:

- Simulation of woody and herbaceous NDVI by adding variation to endmember time series;
- Comparisons of decomposed woody and herbaceous components with cover fractions derived from high resolution satellite imagery (Helman *et al.* 2015)
- Transect-based visual sampling of high resolution Google Earth images to create MODIS pixel scale estimates of woody and herbaceous cover and retrieval of supplementary point data derived from published studies for comparison.

**Simulated Data**

Data for validation were simulated by adding random values (range from -0.1 to 0.1) to each observation of the two endmember time series to simulate the two components of

a mixed time series. The mixed time series is calculated as sum of fractions of the two simulated components. We then decomposed the mixed time series based on the two endmembers using our method. The results from the decomposition were then compared to the simulated components.

**Cover Fractions from High Resolution Imagery**

High-resolution images including IKONOS and Google Earth data were used to generate the fractional cover dataset. Two IKONOS images acquired during the dry season (Figure 1) on 11 May and 11 June 2010 were available. The multispectral bands (4 m resolution) were fused with the panchromatic band (1 m resolution) to create pan-sharpened multispectral images. Each pan-sharpened image was previously clustered into 100 groups and further classified into photosynthetic vegetation (PV), nonphotosynthetic vegetation, bare soil, and other land cover classes (Hill *et al.* 2016). In this study, the cluster groups within the PV class were further separated into green woody and green herbaceous classes (Figure 6). Classification results were evaluated using manually selected woody and herbaceous patches from high-resolution images. The overall classification accuracy was 86.2% for the 11 May image and 92.6% for the 11 June image at 1 m resolution (Table 2). The classification images were converted to the fractional cover of green woody and herbaceous vegetation within the grids of the MODIS images. We then developed a regression tree model that correlates the decomposed NDVI with a subset of the fractional cover dataset. Regression tree models

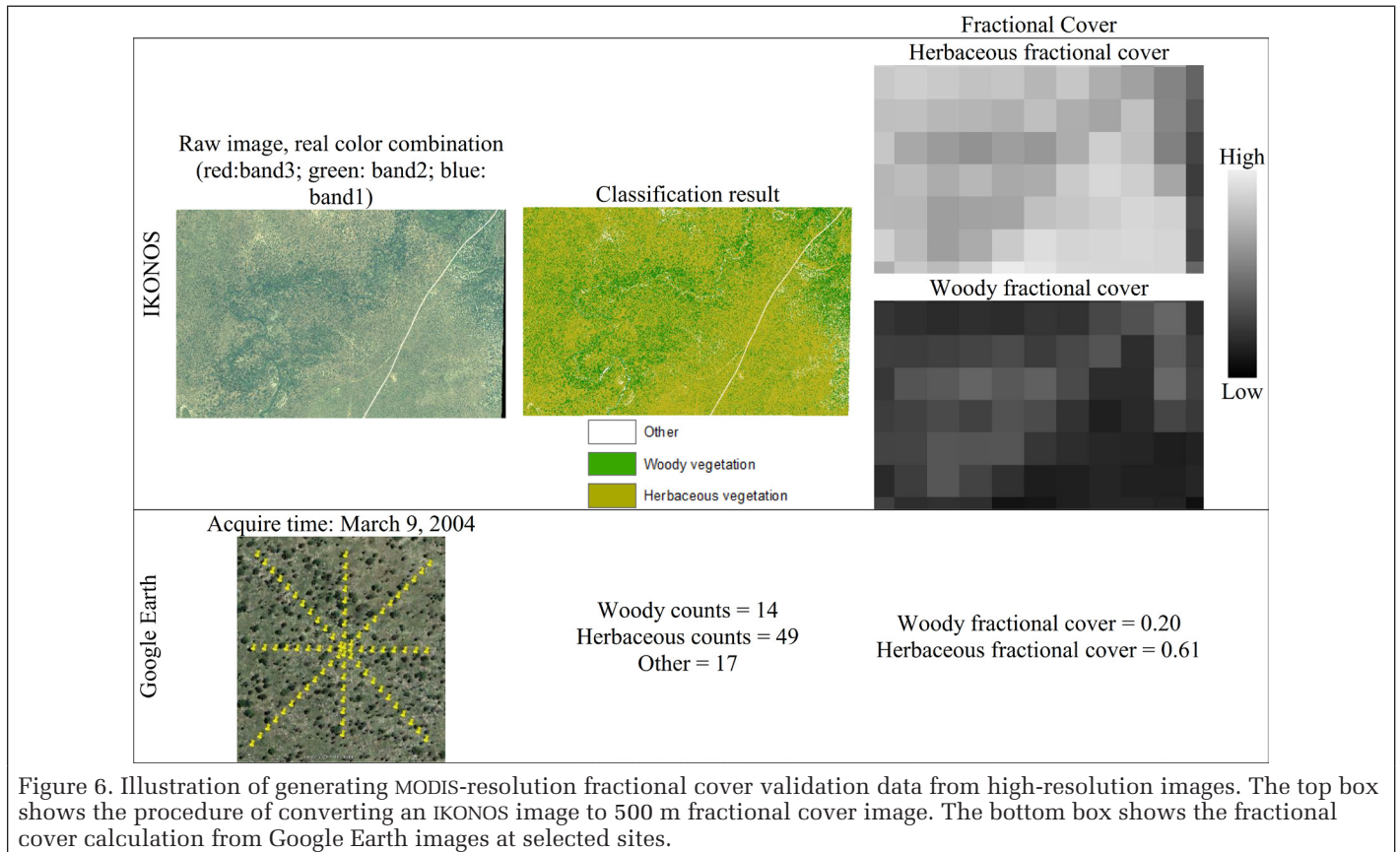


Figure 6. Illustration of generating MODIS-resolution fractional cover validation data from high-resolution images. The top box shows the procedure of converting an IKONOS image to 500 m fractional cover image. The bottom box shows the fractional cover calculation from Google Earth images at selected sites.

Table 2. IKONOS image classification accuracy.

Image Date	Class	Product Accuracy (%)	User Accuracy (%)	Overall Accuracy (%)	Kappa Coefficient
May 11	green woody vegetation	77.03	96.57	86.20	0.73
	Green herbaceous vegetation	96.83	78.43		
June 11	Green woody vegetation	87.82	97.68	92.62	0.85
	Green grass vegetation	97.76	88.22		

were developed using 75 randomly selected points from the fractional cover dataset using software R with default settings. The regression tree models were then validated against the remaining dataset (82 points).

#### Google Earth Visual Transects and Data from the Literature

Growing season images (i.e., 9 March 2004, 27 February 2010, and 23 April 2007) were acquired from Google Earth Pro are © 2017 DigitalGlobe. A total of 100 validation sites, each the size of a MODIS pixel, were also selected from Google Earth, and the fractional covers of herbaceous and woody vegetation within these points were estimated. The sites scattered across ecoregions (ER)1, ER4, and ER7, representing diverse vegetation cover ranging from dense woodland to grassland with a variety of species combinations. A total of 80 equally spaced sampling points along four transects (Figure 6) within the sampling site were used to count their corresponding cover types (i.e., woody, herbaceous, and others). Green woody and green herbaceous fractional covers within each site were calculated from these observations.

## Results

### NDVI Decomposition at Four Representative Sites

Figure 7 shows the decomposition results at four locations (Figure 1) representing four typical land cover types from the Food and Agriculture Organization (FAO) land use characteristics. Site A (forest) had a total NDVI varying between 0.4 and 0.8. Most of the NDVI came from woody component while herbaceous NDVI was less than 0.1. Site B (protected shrubland) had lower total NDVI with a faster decreasing rate in most years than site A. Both woody and herbaceous vegetation was prevalent on this site, and herbaceous NDVI achieved 0.17. Site C (shrubland with moderate livestock density) had the lowest total NDVI of the four sites and negligible woody vegetation. The woody NDVI remained low except in 2006 and 2007, and reached its maximum at the early growing season of 2007. Site D (open shrubland) was mostly covered by grass with sparse woody vegetation. Virtually all of the seasonal signal at this site was provided by the herbaceous component. The herbaceous NDVI achieved a maximum value of 0.4 and dominated the total NDVI seasonal variation. The decreasing fraction of woody NDVI and increasing fraction of herbaceous NDVI from Site A to Site D agreed with the gradients shown in FAO land use (Figure 2a) and Ecoregion characteristics (Figure 1) from forest to shrubland and grassland. Moreover, the woody time series exhibited an earlier increase and later decrease in NDVI than the herbaceous time series at all four sites.

### Spatial and Temporal Variation of Decomposed NDVI Signals

Figure 8 shows the monthly NDVI of the woody and herbaceous vegetation averaged for the period 2002–2011. Woody NDVI

exhibits an overall gradient decreasing from north to south, while herbaceous NDVI showed more heterogeneous distribution. The northern ecoregions (i.e. ER1 and ER2) showed high woody NDVI with strong seasonal variation (Figure 8) because of the dominant presence of semideciduous Miombo tree species which only drop leaves for a short period (Fuller 1999; Veenendaal *et al.* 2008). However, a close-up examination of variation in the Angolan Miombo Woodlands (red box) shows high herbaceous and low woody NDVI, corresponding to agriculture and urban areas in the Google Earth image. The

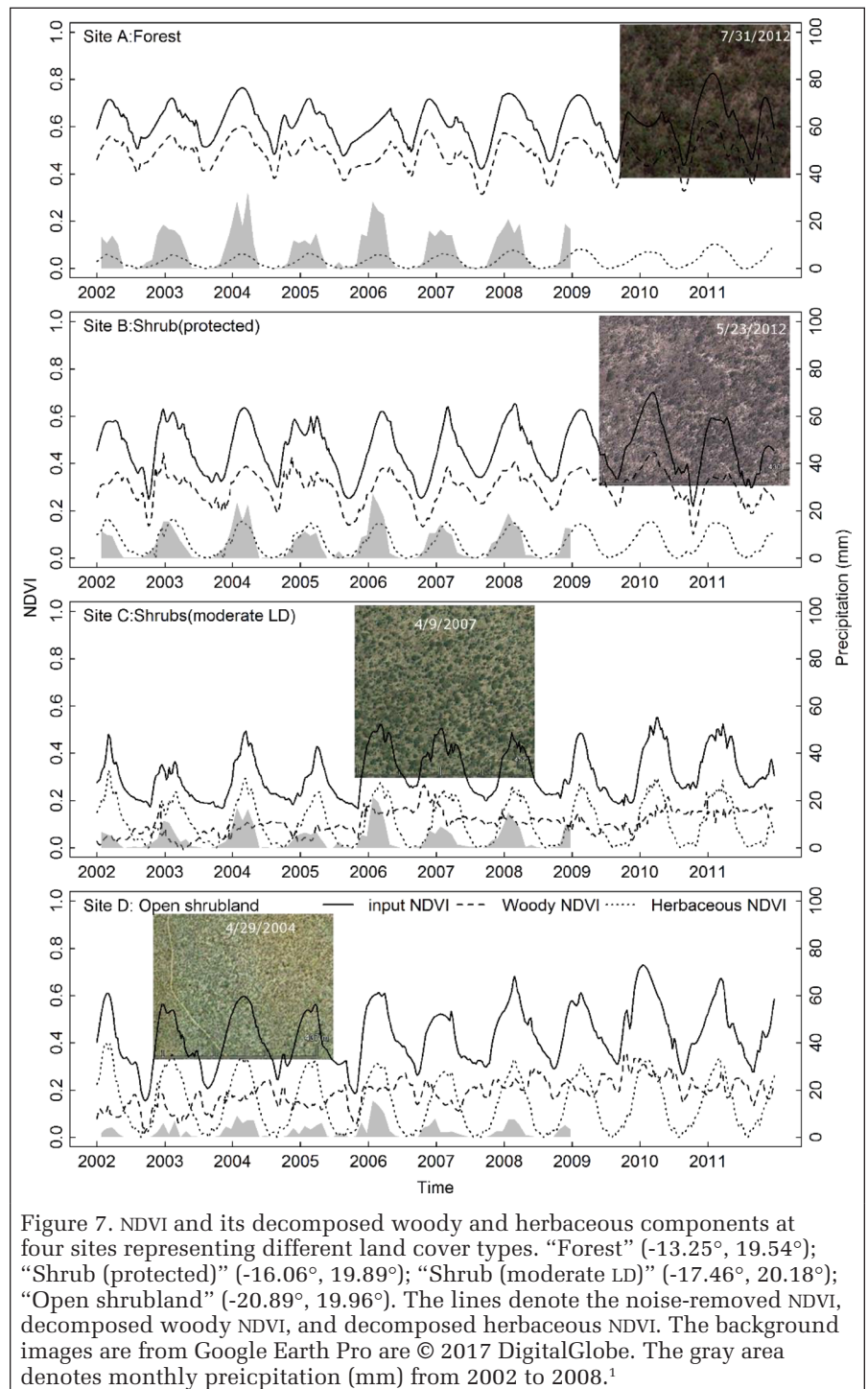


Figure 7. NDVI and its decomposed woody and herbaceous components at four sites representing different land cover types. “Forest” (-13.25°, 19.54°); “Shrub (protected)” (-16.06°, 19.89°); “Shrub (moderate LD)” (-17.46°, 20.18°); “Open shrubland” (-20.89°, 19.96°). The lines denote the noise-removed NDVI, decomposed woody NDVI, and decomposed herbaceous NDVI. The background images are from Google Earth Pro are © 2017 DigitalGlobe. The gray area denotes monthly precipitation (mm) from 2002 to 2008.<sup>1</sup>

1. Joint Institute for the Study of the Atmosphere and Ocean. [http://research.jisao.washington.edu/data\\_sets/ud/](http://research.jisao.washington.edu/data_sets/ud/)

central ecoregions (i.e., ER4 and ER7 ecoregions) showed the largest seasonal variations with woody NDVI reaching the highest value in January and the lowest in August. Those ecoregions also showed a transition from dominant woody to herbaceous NDVI from north to south. The southern ecoregions (i.e. ER3, ER5, and ER8) showed very low woody NDVI and low temporal variation, related to low woody cover driven by low precipitation. The ER8 showed decreasing herbaceous NDVI from north to south, and both woody and herbaceous NDVI were minor in the southern ER8. The maps showed very low NDVI between July and September (Figure 8), associated with senescence of the grasses, loss of leaves from tree species, and general decline in vegetation cover as a result of herbivory in the dry season.

### Validation of Woody and Herbaceous Components

Figure 9a shows the time series endmembers used in the simulation. Figure 9b and Figure 9c showed very strong linear relationships between the decomposed and simulated components ( $R^2 = 0.92$  and  $0.98$ , respectively).  $X_2$  was the dominant component in the mixed time series, and the estimated value matched well with the simulated value with the regression line overlapped with the 1-1 line.  $X_1$  contributed less to the mixed time series, and it was slightly underestimated based on the regression line. It noteworthy that the noise ( $\pm 0.1$ ) in  $X_1$  is relatively more significant than the noise in  $X_2$  based on the magnitude of the endmember time series. This comparison indicates that the method performs robustly in separating mixtures of distinct signals assuming these signals are representative of the actual vegetation on the ground.

The results of the fractional cover-based comparison are shown in Figures 6a and 6b). The herbaceous decomposed NDVI fractions showed a better correspondence with the corresponding image-based cover fraction than did the woody decomposed NDVI fraction ( $R^2 = 0.55$  for woody and  $R^2 = 0.64$  for herbaceous). There was a wide range of woody cover at high resolution for a given level of decomposed woody NDVI fraction. However, there was better correspondence between

the decomposed woody NDVI fraction and combined data from Google Earth visual transects and data acquired in previously published studies (Figure 10c).

### Discussion

This paper demonstrated a new method and the framework to separate the phenological dynamics of deciduous woody and herbaceous vegetation using frequency information. Traditional methods assumed that the evergreen woody phenological dynamics are negligible or the same (but small proportion) as herbaceous vegetation, which were reasonable for savannas with only evergreen woody (Lu *et al.* 2003; Helman *et al.* 2015). Comparing to traditional approaches, the approach has several advantages. First, it captures seasonal differences of deciduous woody and herbaceous vegetation and omits high frequency variation due to discrete events such as precipitation or disturbances (Figure 5). Second, it can fit not only the amplitude but also the phases of seasonal variation, which could reduce errors caused by the temporal shifts between the pure woody/herbaceous vegetation and the mixed vegetation. These attributes are important for improved monitoring temporal changes in savanna ecosystems and for further understanding their impact on productivity, wildfire, and biogeochemical cycles (Kahiu and Hanan 2018).

The approach is considered successful because of the consistent relationship between the simulated and decomposed components (Figure 9) and between the decomposed NDVI and fractional cover data (Figures 6a and 6b). The relatively poor correspondence between the decomposed woody NDVI and woody cover fraction from the high resolution images may be explained by specific heterogeneity in woody density and distribution at these image limited locations interacting with the 500 m pixel scale, since they could not be considered representative of the wide array of vegetation across the study region. The fractional cover data derived from high-resolution imagery covered various vegetation species in both the dry season and rainy season. The linear relationship between

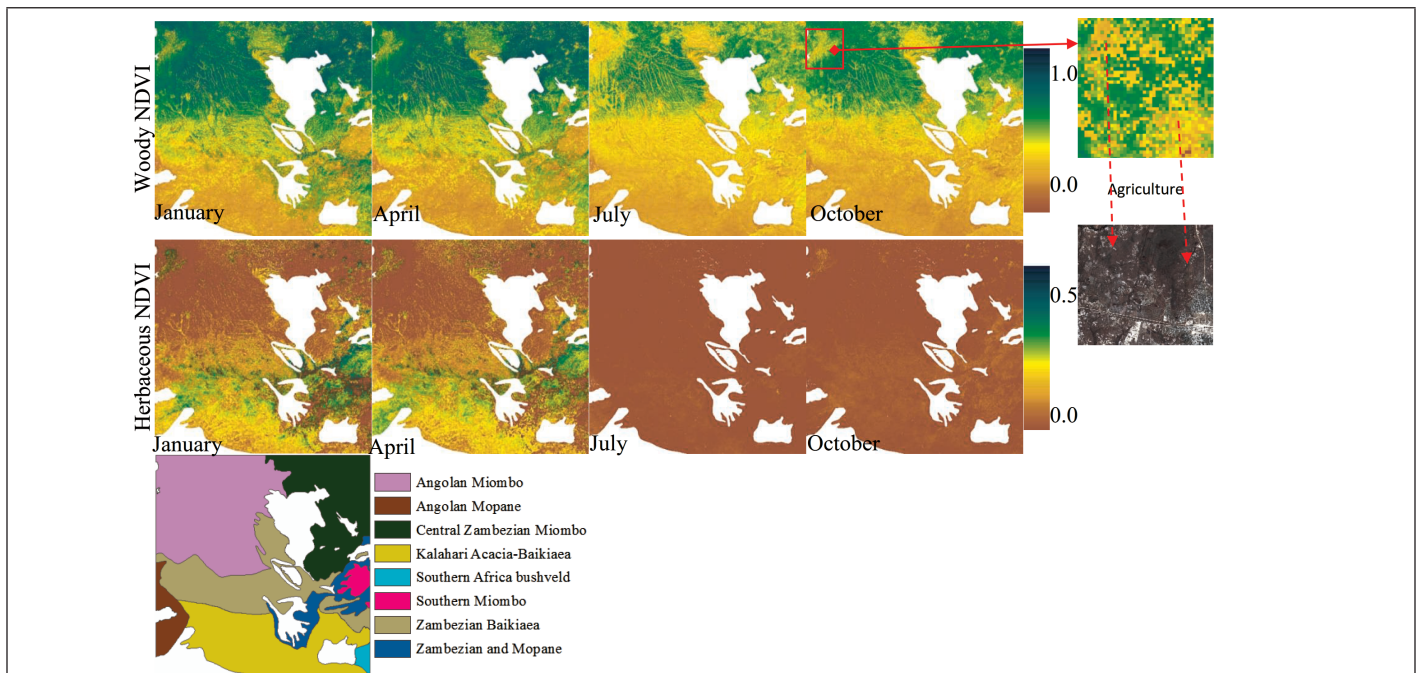


Figure 8. Estimates of monthly average woody and herbaceous NDVI (2002–2011). The color ramp from dark blue to orange indicates the NDVI value from high to low. A zoom in area (red box) shows agriculture and urban cover based on the Google Earth image. The bottom row exhibits the ecosystem boundary.

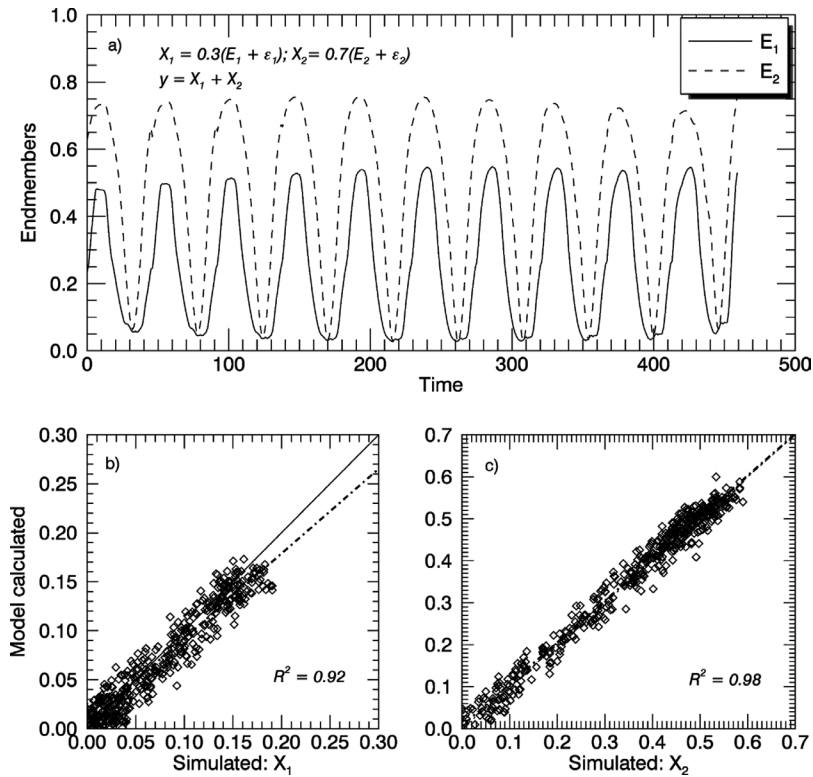


Figure 9. Validation of the decomposition method based on the simulated data. Plot a) shows time series of endmembers E1 and E2. X1 and X2 are the simulated components which are fractions of the two endmembers with noises (random values from -0.1 to 0.1). The simulated mixed pixel time series (y) is the sum of two components X1 and X2. The time series (y) is decomposed based on E1 and E2 and compared to X1 and X2, as shown in plots b) and c). The solid lines in b) and c) are 1-to-1 lines, and the dashed lines are regression results.

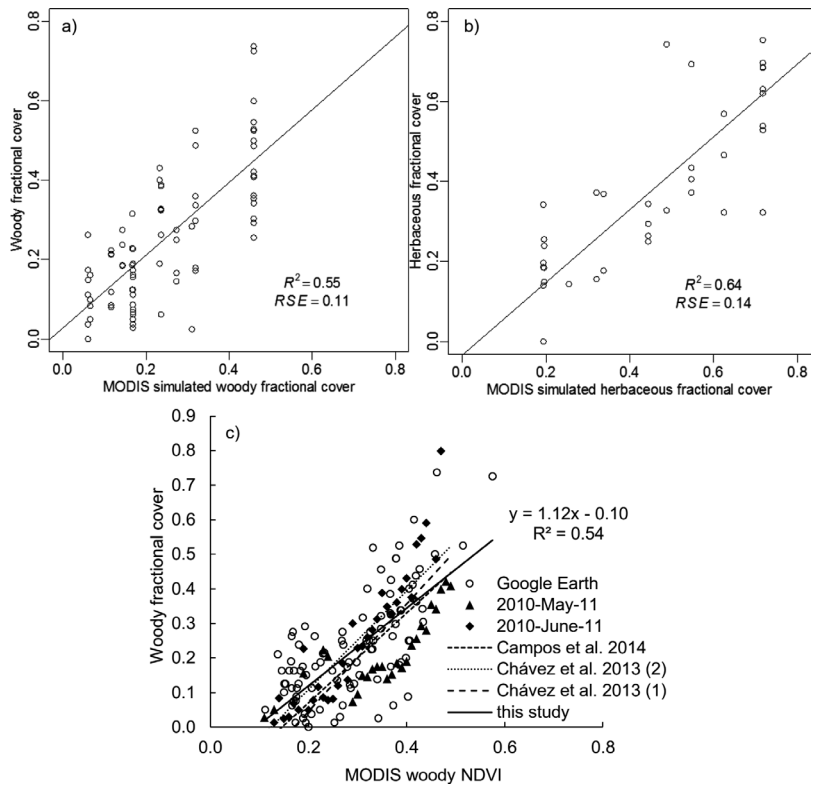


Figure 10. Comparison between the fractional covers derived from the frequency decomposition approach and cover measured from high-resolution images: (a) woody components comparison, (b) herbaceous components comparison. The regression line with  $R^2$ , and residual standard error are displayed. (c) Linear relationship between the woody NDVI and IKONOS and Google Earth derived fractional cover compared to previous studies.

woody NDVI and all fractional cover data from this study (Figure 10c) also agreed well with previous findings (Chávez *et al.* 2013; Campos *et al.* 2014). The ideal comparison would be a study that compared NDVI and fractional cover for woody and herbaceous vegetation separately. However, few studies had been conducted before. Chaves' (Chaves *et al.* 2013) work was the best match as it 1) focused on woody vegetation only and eliminated herbaceous influence; and 2) the study area was arid savanna and the woody vegetation was semideciduous, which matches our study. Campos's work (Campos *et al.* 2014) matches our study because their study site had a homogeneous land cover type. The similarity in the relationship between woody NDVI and its fractional cover signifies our decomposition of savanna NDVI into woody and herbaceous components are successful.

The frequency decomposition of woody and herbaceous NDVI at the MODIS scale showed agreement with previous vegetation phenology studies in the region (Monasterio and Sarmiento 1976; Williams *et al.* 1997; Zhang *et al.* 2005; Higgins *et al.* 2011). For example, the previous study suggested that in this region woody vegetation flushes leaves right before the rainy season, while herbaceous vegetation does not grow leaves until rainy season starts (Higgins *et al.* 2011). This study showed the woody NDVI started to increase in October and decrease in May while the similar variation of herbaceous NDVI appeared between November and April in the Zambezi and Mopane Woodlands where the rainfall period was between November and April.

The spatial and temporal patterns of precipitation strongly affect the composition and temporal and seasonal patterns of woody and herbaceous vegetation in the region. For example, our study showed high woody NDVI with small seasonal variation in the northern area where annual precipitation was higher than ~760 mm (Figure 2b and Figure 8), which indicated the domination of semideciduous woody vegetation. Previous studies also found that the mean annual precipitation constrained the woody cover distribution; precipitation was not a limiting factor above ~650 mm to 700 mm (Sankaran *et al.* 2005; Sankaran *et al.* 2008). The subtle herbaceous NDVI in high precipitation regions suggested that herbaceous vegetation was suppressed by woody vegetation (Guan *et al.* 2012). On the other hand, we found, in the very southern part of the study area, the woody seasonal variation was minor comparing to the multi-year trend (type 1 variation), though Google Earth images showed some sparse shrub vegetation (Figure 7). Possible reasons for the minor woody seasonal variation were the sensitivity of MODIS sensor at the 500 m scale and the changing sensor view angle throughout the year (Helman *et al.* 2015). This indicates an uncertainty of the woody NDVI at the open shrubland region.

There are, however, some limitations in this study. First, the endmembers selected might be mixed pixels because of the coarse resolution and the heterogeneous savanna cover. The pure woody pixels could be easily found as there is a large amount of dense forest at the ER1 and ER2. There is often scattered woody vegetation in grassland pixels, though the woody coverage is minor and has limited influence at the 500 m scale. This study is part of a project that aims to separate green woody, green herbaceous, dry vegetation, and bare soil using NDVI and SWIR bands. Thus the 500 m NDVI time series were used. However, a higher spatial resolution dataset is preferred for this method to reduce the mixed pixel issue. Second, this study separates the green woody and green herbaceous seasonal variation without explicit separation of the soil and dry vegetation (Hill *et al.* 2016). This is also the reason we decomposed NDVI instead of spectral bands, as NDVI mainly captures green vegetation dynamics and is insensitive to soil and dry vegetation. To further reduce the influence of

soil and dry vegetation, a solution from previous research (Lu *et al.* 2003; Helman *et al.*, 2015) was applied in this study. Third, the woody and herbaceous time series were separated using observations for a 10-year period without explicitly considering possible impacts of abrupt disturbances such as fire or land conversion. In this case, if both woody and herbaceous vegetation grew back after disturbances and retained the relative covers, the method can still decompose the two components. However, if the relative woody and herbaceous vegetation coverages were changed after disturbances, the method could have a bias. A practical solution in the future is first to break the time series into segments when abrupt changes occur using the Continuous Change Detection and Classification (Zhe *et al.* 2014) or the breaks for additive season and trend (BFAST) (Verbesselt *et al.* 2010) algorithms. The frequency decomposition approach proposed here could then be applied to each time series segment identified. In combination with the above change detection algorithms, the proposed approach has the potential to map woody and herbaceous phenology changes after disturbances such as fire or drought.

## Conclusions

This study presents a new method to decompose deciduous woody and herbaceous components from the MODIS NDVI time series using the following procedure:

1. Disintegrate the NDVI time series into woody vegetation only baseline and seasonal variation using the traditional STL procedure.
2. Decompose the seasonal variation into woody and herbaceous components using the new frequency decomposition method proposed in this study.
3. Represent the woody NDVI change by adding the NDVI baseline and the seasonal variation of woody components.

This approach was applied and tested in a savanna region in southern Africa. The woody and herbaceous fractional covers were validated against IKONOS and Google Earth images with  $R^2 = 0.55$  and  $0.64$ , respectively. The spatial patterns and interannual variability of fractional NDVI and cover showed obvious regional differences that were mainly determined by the amount and seasonality of precipitation as well as disturbances such as land conversion. Those phenological dynamics information would be helpful for understanding ecosystem changes, driving forces, and consequences (Knoop and Walker 1985; Bucini and Hanan 2007; Sankaran *et al.* 2008), and for further understanding their impact on productivity, wildfire, and biogeochemical cycles (Kahiu and Hanan 2018).

The frequency decomposition method has been, as a case study, successfully applied to derive compositional phenology changes from NDVI data in southern Africa. We do not see any hurdles that prevent this approach from being applied to savanna in other regions or to different types of indexes (EVI, Tasseled Cap transformation indexes) or remotely sensed time series (Landsat, Sentinel-2, MODIS). The Interactive Data Language (IDL) code developed for the frequency decomposition is available by contacting the author.

## Acknowledgments

IKONOS images were kindly provided by Dr. Kelley Crews from Department of Geography and Environment at the University of Texas Austin. The authors would also like to thank the editor and anonymous reviewers for their valuable comments on the improvement of the paper. This work was partially supported by a grant from NASA (grant number #NNX10AH20G).

## References

- Archibald, S. and R. Scholes. 2007. Leaf green-up in a semi-arid African savanna—Separating tree and grass responses to environmental cues. *Journal of Vegetation Science* 18(4):583–594.
- Bracewell, R. 1966. The Fourier transform and its applications. *American Journal of Physics* 34(8):712–712.
- Bradley, A. V., F. F. Gerard, N. Barbier, G. P. Weedon, L. O. Anderson, C. Huntingford and E. Arai. 2011. Relationships between phenology, radiation and precipitation in the Amazon region. *Global Change Biology* 17(6):2245–2260.
- Brandt, M., P. Hiernaux, T. Tagesson, A. Verger, K. Rasmussen, A. A. Diouf and R. Fensholt. 2016. Woody plant cover estimation in drylands from Earth Observation based seasonal metrics. *Remote Sensing of Environment* 172:28–38.
- Bucini, G. and N. P. Hanan. 2007. A continental scale analysis of tree cover in African savannas. *Global Ecology and Biogeography* 16(5):593–605.
- Burgess, N., J. A. Hales, E. Underwood, E. Dinerstein, D. Olson, I. Itoua and K. Newman. 2004. *Terrestrial Ecoregions of Africa and Madagascar: A Conservation Assessment*. Island Press.
- Campos, I., C. M. Neale, M.-L. López, C. Balbontín and A. Calera. 2014. Analyzing the effect of shadow on the relationship between ground cover and vegetation indices by using spectral mixture and radiative transfer models. *Journal of Applied Remote Sensing* 8(1):083562.
- Chávez, R. O., J. G. Clevers, M. Herold, E. Acevedo and M. Ortiz. 2013. Assessing water stress of desert tamarugo trees using in situ data and very high spatial resolution remote sensing. *Remote Sensing* 5(10):5064–5088.
- Chidumayo, E. 2002. Changes in miombo woodland structure under different land tenure and use systems in central Zambia. *Journal of Biogeography* 29(12):1619–1626.
- Cleveland, R. B., W. S. Cleveland and I. Terpenning. 1990. STL: A seasonal-trend decomposition procedure based on Loess. *Journal of Official Statistics* 6(1):3.
- Coetsee, C., W. J. Bond and E. C. February. 2010. Frequent fire affects soil nitrogen and carbon in an African savanna by changing woody cover. *Oecologia* 162(4): 1027–1034.
- Cowling, R. M., D. M. Richardson and S. M. Pierce. 2004. *Vegetation of Southern Africa*. Cambridge University Press.
- DiMiceli, C., M. Carroll, R. Sohlberg, C. Huang, M. Hansen and J. Townshend. 2011. Annual global automated MODIS vegetation continuous fields (MOD44B) at 250 m spatial resolution for data years beginning day 65, 2000–2010, collection 5 percent tree cover. College Park, Md.: University of Maryland.
- Donohue, R. J., T. McVICAR and M. L. Roderick. 2009. Climate related trends in Australian vegetation cover as inferred from satellite observations, 1981–2006. *Global Change Biology* 15(4):1025–1039.
- Dye, D. G., B. R. Middleton, J. M. Vogel, Z. Wu, and M. Velasco. 2016. Exploiting differential vegetation Phenology for satellite-based mapping of semiarid grass vegetation in the Southwestern United States and Northern Mexico. *Remote Sensing* 8(11):889.
- Friedl, M. A., D. Sulla-Menashe, B. Tan, A. Schneider, N. Ramankutty, A. Sibley and X. Huang. 2010. MODIS collection 5 global land cover: Algorithm refinements and characterization of new datasets. *Remote Sensing of Environment* 114(1):168–182.
- Fuller, D. O. 1999. Canopy phenology of some mopane and miombo woodlands in eastern Zambia. *Global Ecology and Biogeography* 8(3–4):199–209.
- Geerken, R., B. Zaitchik and J. P. Evans. 2005. Classifying rangeland vegetation type and coverage from NDVI time series using Fourier Filtered Cycle Similarity. *International Journal of Remote Sensing* 26(24):5535–5554.
- Gessner, U., D. Klein, C. Conrad, M. Schmidt and S. Dech. 2009. Towards an automated estimation of vegetation cover fractions on multiple scales: Examples of Eastern and Southern Africa. In *Proceedings of the 33rd International Symposium on Remote Sensing of Environment*.
- Gessner, U., M. Machwitz, C. Conrad and S. Dech. 2013. Estimating the fractional cover of growth forms and bare surface in savannas. A multi-resolution approach based on regression tree ensembles. *Remote Sensing of Environment* 129:90–102.
- Guan, K., E. Wood and K. Caylor. 2012. Multi-sensor derivation of regional vegetation fractional cover in Africa. *Remote Sensing of Environment* 124:653–665.
- Guerschman, J. P., M. J. Hill, L. J. Renzullo, D. J. Barrett, A. S. Marks and E. J. Botha. 2009. Estimating fractional cover of photosynthetic vegetation, non-photosynthetic vegetation and bare soil in the Australian tropical savanna region upscaling the EO-1 Hyperion and MODIS sensors. *Remote Sensing of Environment* 113(5):928–945.
- Hansen, M., R. DeFries, J. Townshend, L. Marufu and R. Sohlberg. 2002. Development of a MODIS tree cover validation data set for Western Province, Zambia. *Remote Sensing of Environment* 83(1–2):320–335.
- Helman, D., I. M. Lensky, N. Tessler and Y. Osem. 2015. A phenology-based method for monitoring woody and herbaceous vegetation in Mediterranean forests from NDVI time series. *Remote Sensing* 7(9):12314–12335.
- Higgins, S. I., M. D. Delgado Cartay, E. C. February and H. J. Combrink. 2011. Is there a temporal niche separation in the leaf phenology of savanna trees and grasses? *Journal of Biogeography* 38(11):2165–2175.
- Hijmans, R. J., S. E. Cameron, J. L. Parra, P. G. Jones and A. Jarvis. 2005. Very high resolution interpolated climate surfaces for global land areas. *International Journal of Climatology* 25(15):1965–1978.
- Hill, M. J. and N. P. Hanan. 2010. *Ecosystem Function in Savannas: Measurement and Modeling at Landscape to Global Scales*. CRC Press.
- Hill, M. J., Q. Zhou, Q. Sun, C. B. Schaaf, J. Southworth, N. B. Mishra and K. A. Crews. 2016. Dynamics of the relationship between NDVI and SWIR32 vegetation indices in southern Africa: Implications for retrieval of fractional cover from MODIS data. *International Journal of Remote Sensing* 37(6):1476–1503.
- Jakubauskas, M. E., D. R. Legates and J. H. Kastens. 2002. Crop identification using harmonic analysis of time-series AVHRR NDVI data. *Computers and Electronics in Agriculture* 37(1–3):127–139.
- Jun, W., S. Zhongbo and M. Yaoming. 2004. Reconstruction of a cloud-free vegetation index time series for the Tibetan Plateau. *Mountain Research and Development* 24(4):348–353.
- Kahiu, M. N. and N. P. Hanan. 2018. Estimation of woody and herbaceous leaf area index in sub saharan Africa using MODIS data. *Journal of Geophysical Research: Biogeosciences* 123(1):3–17.
- Knoop, W. and B. Walker. 1985. Interactions of woody and herbaceous vegetation in a southern African savanna. *The Journal of Ecology* 235–253.
- Leinenkugel, P., C. Kuenzer, N. Oppelt and S. Dech. 2013. Characterisation of land surface phenology and land cover based on moderate resolution satellite data in cloud prone areas—A novel product for the Mekong Basin. *Remote Sensing of Environment* 136:180–198.
- Lhermitte, S., J. Verbesselt, I. Jonckheere, K. Nackaerts, J. A. van Aardt, W. W. Verstraeten and P. Coppin. 2008. Hierarchical image segmentation based on similarity of NDVI time series. *Remote Sensing of Environment* 112(2):506–521.
- Lu, H., M. R. Raupach, T. R. McVicar and D. J. Barrett. 2003. Decomposition of vegetation cover into woody and herbaceous components using AVHRR NDVI time series. *Remote Sensing of Environment* 86(1):1–18.
- Lunetta, R. S., J. F. Knight, J. Ediriwickrema, J. G. Lyon and L. D. Worthy. 2006. Land-cover change detection using multi-temporal MODIS NDVI data. *Remote Sensing of Environment* 105(2):142–154.
- Menenti, M., S. Azzali, W. Verhoef and R. Van Swol. 1993. Mapping agroecological zones and time lag in vegetation growth by means of Fourier analysis of time series of NDVI images. *Advances in Space Research* 13(5):233–237.

- Monasterio, M. and G. Sarmiento. 1976. Phenological strategies of plant species in the tropical savanna and the semi-deciduous forest of the Venezuelan Llanos. *Journal of Biogeography* 3(4):325–355.
- Moody, A. and D. M. Johnson. 2001. Land-surface phenologies from AVHRR using the discrete Fourier transform. *Remote Sensing of Environment* 75(3):305–323.
- Olson, D. M., E. Dinerstein, E. D. Wikramanayake, N. D. Burgess, G. V. Powell, E. C. Underwood and J. C. Morrison. 2001. Terrestrial ecoregions of the world: A new map of life on Earth: A new global map of terrestrial ecoregions provides an innovative tool for conserving biodiversity. *BioScience* 51(11):933–938.
- Richer, R. 2008. Leaf phenology and carbon dynamics in six leguminous trees. *African Journal of Ecology* 46(1):88–95.
- Roerink, G. J., M. Menenti, W. Soepboer and Z. Su. 2003. Assessment of climate impact on vegetation dynamics by using remote sensing. *Physics and Chemistry of the Earth, Parts A/B/C* 28(1–3):103–109.
- Sankaran, M., N. P. Hanan, R. J. Scholes, J. Ratnam, D. J. Augustine, B. S. Cade and F. Ludwig. 2005. Determinants of woody cover in African savannas. *Nature* 438(7069):846.
- Sankaran, M., J. Ratnam and N. Hanan. 2008. Woody cover in African savannas: The role of resources, fire and herbivory. *Global Ecology and Biogeography* 17(2):236–245.
- Schaaf, C. B., F. Gao, A. H. Strahler, W. Lucht, X. Li, T. Tsang and J.-P. Muller. 2002. First operational BRDF, albedo nadir reflectance products from MODIS. *Remote Sensing of Environment* 83(1–2):135–148.
- Schaaf, C. B., J. Liu, F. Gao and A. H. Strahler. 2010. Aqua and Terra MODIS albedo and reflectance anisotropy products. *Land Remote Sensing and Global Environmental Change*, 549–561. Springer.
- Seghieri, J., C. Floret and R. Pontanier. 1995. Plant phenology in relation to water availability: Herbaceous and woody species in the savannas of northern Cameroon. *Journal of Tropical Ecology* 11(2):237–254.
- Shao, Y., R. S. Lunetta, B. Wheeler, J. S. Iames and J. B. Campbell. 2016. An evaluation of time-series smoothing algorithms for land-cover classifications using MODIS-NDVI multi-temporal data. *Remote Sensing of Environment* 174:258–265.
- Staver, A. C., S. Archibald and S. A. Levin. 2011. The global extent and determinants of savanna and forest as alternative biome states. *Science* 334(6053):230–232.
- Strobbach, B. J. and A. Petersen. 2007. Vegetation of the central Kavango woodlands in Namibia: An example from the Mile 46 Livestock Development Centre. *South African Journal of Botany* 73(3):391–401.
- Vancutsem, C., J.-F. Pekel, C. Evrard, F. Malaisse and P. Defourny. 2009. Mapping and characterizing the vegetation types of the Democratic Republic of Congo using SPOT VEGETATION time series. *International Journal of Applied Earth Observation and Geoinformation* 11(1):62–76.
- Veenendaal, E. M., K. B. Mantlana, N. W. Pammenter, P. Weber, P. Huntsman-Mapila and J. Lloyd. 2008. Growth form and seasonal variation in leaf gas exchange of *Colophospermum mopane* savanna trees in northwest Botswana. *Tree Physiology* 28(3):417–424.
- Verbesselt, J., R. Hyndman, A. Zeileis and D. Culvenor. 2010. Phenological change detection while accounting for abrupt and gradual trends in satellite image time series. *Remote Sensing of Environment* 114(12):2970–2980.
- Verbesselt, J., P. Jonsson, S. Lhermitte, J. Van Aardt and P. Coppin. 2006. Evaluating satellite and climate data-derived indices as fire risk indicators in savanna ecosystems. *IEEE Transactions on Geoscience and Remote Sensing* 44(6):1622–1632.
- Wagenseil, H. and C. Samimi. 2007. Woody vegetation cover in Namibian savannas: A modelling approach based on remote sensing (Die Gehölzdichte in den Savannen Namibias: Eine fernerkundungsgestützte Modellierung). *Erdkunde* 325–334.
- White, M., J. Shaw and R. Ramsey. 2005. Accuracy assessment of the vegetation continuous field tree cover product using 3954 ground plots in the south western USA. *International Journal of Remote Sensing* 26(12):2699–2704.
- Williams, R., B. Myers, W. Muller, G. Duff and D. Eamus. 1997. Leaf phenology of woody species in a north Australian tropical savanna. *Ecology* 78(8):2542–2558.
- Yui, X., D. Zhuang, H. Chen and X. Hou. 2004. Forest classification based on MODIS time series and vegetation phenology. Pages 2369–2372 in *Proceedings 2004 IEEE International Geoscience and Remote Sensing Symposium*, vol. 4.
- Zhang, X., M. A. Friedl, C. B. Schaaf, A. H. Strahler and Z. Liu. 2005. Monitoring the response of vegetation phenology to precipitation in Africa by coupling MODIS and TRMM instruments. *Journal of Geophysical Research: Atmospheres* 110(D12).
- Zhou, Q., M. Hill, Q. Sun and C. Schaaf. 2016. Retrieving understory dynamics in the Australian tropical savannah from time series decomposition and linear unmixing of MODIS data. *International Journal of Remote Sensing* 37(6):30.
- Zhu, Z. and C. E. Woodcock. 2014. Continuous change detection and classification of land cover using all available Landsat data. *Remote Sensing of Environment* 144:152–171.

# Examining the Effectiveness of Spectrally Transformed SMA in Urban Environments

Yingbin Deng and Changshan Wu

## Abstract

*Spectral transformation has been applied to address the spectral variability in spectral mixture analysis. However, there is not a study addressing the necessity and applicability of transformed models. This article, therefore, aims to answer two questions: whether significantly different results will be generated through applying a spectral transformation, and which spectral transformation performs better in urban environments. In particular, 26 spectrally transformed schemes were examined in three cities. Results of paired-sample *t* tests demonstrated that normalized spectral mixture analysis performed significantly better than the untransformed scheme in all three study areas. Derivative analysis, independent component analysis, and minimum noise fraction outperformed the untransformed scheme in one or two study areas but underperformed in others. Other schemes are unnecessary, as they have significantly lower accuracy compared to the untransformed scheme.*

## Introduction

Spectral mixture analysis (SMA) has been widely applied to estimate fractional land covers within each pixel of coarse-resolution remote sensing imagery. Spectral transformation, which converts the original spectra linearly or nonlinearly, is one of the widely applied approaches in SMA to address spectral-variability problems. It focuses on enhancing the spectral characteristics to reduce within-class variability and enhance between-classes variability. Spectral transformation has been employed in a large number of remote sensing applications. Wu (2004) proposed a normalized SMA (NSMA) to extract land use and land cover information in the city of Columbus, Ohio, United States. Results indicated that brightness variations were reduced and improved results could be achieved from the NSMA. Asner and Lobell (2000) applied a tie spectral transformation before estimating the fractions of vegetation and soil covers. They concluded that significant variations of soil moisture, canopy architecture, leaf and litter area index, and tissue optics could be compressed using the tied spectra. Zhang, Rivard, and Sanchez-Azofeifa (2004) summarized that second-order derivative spectral unmixing is promising for fraction estimation using hyperspectral data. Similar studies include the research of Tsai and Philpot (1998), Laba, Tsai, Ogurcak, Smith, and Richmond (2005), and Huguenin and Jones (1986). Further, Debba, Caranza, van der Meer, and Stein (2006) concluded that higher-order derivatives contribute more to remote sensing imagery with

higher signal-to-noise ratios. Li (2004) compared the discrete wavelet transform (DWT) with principal components analysis (PCA; Richards and Richards 1999; Chuvieco and Huete 2009) and found that DWT could bring more separability than PCA, leading to improvement of fractional estimations. Similar conclusions were achieved in the studies of Bruce, Koger, and Li (2002) and Zhang, Rivard, Sánchez-Azofeifa, and Castro-Esau (2006). Youngentob *et al.* (2011) examined the performance of continuum-removal (CR) analysis using hyperspectral data, and the results showed improvement in overall accuracy. Further, PCA (Pearson 1901; Byrne, Crapper and Mayo 1980; Richards and Richards 1999), the minimum noise fraction (MNF) transform (Green, Berman, Switzer and Craig 1988; Geladi, Isaksson, Lindqvist, Wold and Esbensen 1989; Boardman and Kruse 1994), tasseled cap (TC; Kauth and Thomas 1976; Jensen and Lulla 1987), and independent component analysis (ICA; Bayliss, Gualtieri and Cropm 1998; Chen and Zhang 1999; Hyvärinen and Oja 2000) are commonly employed for the land surface feature enhancement before applying SMA. Spectral characteristics of different land cover classes are highlighted in different output layers of these transformations. Many researchers have used these transformation techniques to assist in the selection of end members, reduce spectral within-class variability, and enhance between-classes variability. Further, different spatial filters, such as low-pass (LP; Green *et al.* 1988), high-pass (HP; Yu *et al.* 2006), Gaussian high-pass (GHP; Schowengerdt 2006), and Gaussian low-pass (GLP; Schowengerdt 2006), are commonly used to enhance the spectral characteristics' edges or to smooth remote sensing imagery (Xu *et al.* 2011).

Although many researchers have applied spectral-transformation techniques in remote sensing applications, there is still a lack of comprehensive and systematic studies to examine their effectiveness. In particular, researchers use different transformed schemes based on their own knowledge and expertise. The necessity of applying a transformed scheme has not been adequately discussed in the literature. In addition, because of the existence of spectral variability, the reliability of each transformed scheme is still unclear, and most researchers apply the transformed schemes in only one study area. It is unknown whether consistent results can be obtained other study areas. Therefore, this study aims to examine whether there is a significant difference in SMA results after applying spectral transformation and to find out which spectral-transformation approach generates consistently better results. The structure of this article is as follows: The next section introduces the background of SMA and spectral transformation techniques, followed by the experiments and the results in three study areas with Landsat Thematic Mapper data. The next section discusses the results and is followed by the conclusions of this study.

---

Yingbin Deng is with the Guangdong Open Laboratory of Geospatial Information Technology and Application, Lab of Guangdong for Utilization of Remote Sensing and Geographical Information System, Guangzhou Institute of Geography, Guangzhou, China; and the Department of Geography, University of Wisconsin-Milwaukee, Milwaukee, WI 53211.

Changshan Wu is with the School of Geology and Geomatics, Tianjin Chengjian University, Tianjin, China; and the Department of Geography, University of Wisconsin-Milwaukee, Milwaukee, WI 53211 (cswu@uwm.edu).

---

Photogrammetric Engineering & Remote Sensing  
Vol. 85, No. 7, July 2019, pp. 521–528.  
0099-1112/19/521–528

© 2019 American Society for Photogrammetry  
and Remote Sensing  
doi: 10.14358/PERS.85.7.521

## Background

### SMA

SMA assumes that more than one land cover class exists in a mixed pixel. The objective of SMA is to estimate the fraction of each end member within a mixed pixel. Generally, two

constraints—sum-to-one  $\sum_j f_j = 1$  and nonnegative ( $0 \leq f_j \leq 1$ )

—should be met in fully constrained SMA, which can be expressed as

$$R_k = \sum_j f_j R_{k,j} + \varepsilon_k, \quad (1)$$

where  $R_k$  is the spectral reflectance of a mixed pixel on band  $k$ ,  $f_j$  is the fraction of end member  $j$  within the pixel,  $R_{k,j}$  is the spectral reflectance of end member  $j$  on band  $k$ ,  $\varepsilon_k$  is the error of band  $k$ , and  $n$  is the number of end members.

Mean absolute error (MAE) is used to evaluate the performance of SMA. It calculates the absolute difference between the estimated fraction and the reference fraction of the corresponding land cover class:

$$MAE = \frac{\sum_{i=1}^m ABS(f_{e,i} - f_{r,i})}{m}, \quad (2)$$

where  $f_{e,i}$  and  $f_{r,i}$  are the estimated and reference fractions, respectively, of sample  $i$  and  $m$  is the number of samples.

### Spectral Transformations

Thirteen linear and 13 nonlinear transformed schemes were examined in this study, as well as the untransformed scheme. These schemes were selected because they are the most common in the literature. Many commercial software applications, such as ERDAS and ENVI, have embedded these models. Researchers can easily implement these transformed schemes in their applications.

#### Linear Spectral Transformations

Seven linear spectral transformations were examined (see Table 1): derivative analysis (DA; Tsai and Philpot 1998), PCA (Richards and Richards 1999), ICA (Hyvarinen 1999; Hyvärinen and Oja 2000), MNF (Green *et al.* 1988; Boardman and Kruse 1994), TC (Kauth and Thomas 1976), band normalization (BN), and DWT (Vetterli and Herley 1992; Strang and Nguyen 1996; Li 2002). Detailed descriptions of these methods follow.

DA is sensitive to curve shape instead of the scale of reflectance (Tsai and Philpot 1998). With this advantage, DAs, especially those of a higher order, are effective for eliminating background signals and illumination effects caused by cloud coverage, sun angle, and topography. Detailed calculation of first, second, and third DAs is given by Tsai and Philpot (1998).

The purpose of PCA (Richards and Richards 1999; Chuvioco and Huete 2009) is to create a new set of orthogonal axes which can maximize data variance. PCA compresses the original intercorrelated data into several uncorrelated variables, called principal components. The amount of variance decreases with increasing component number. Generally, the first three components in PCA contribute more than 90% of the variance in the original data set.

ICA is based on a non-Gaussian assumption of independent sources and applies higher-order statistics to extract the characteristics in non-Gaussian data sets (Hyvarinen 1999; Hyvärinen and Oja 2000). It commonly contains three steps: centering and whitening sample data with the mean, eigenvectors, and eigenvalues; conducting negentropy maximization with the whitened samples to estimate the ICA transform matrix; and transforming the original data using the independent components transform matrix.

MNF transformation, like PCA, separates noise and reduces data dimension (Green *et al.* 1988; Boardman and Kruse 1994). First, in the noise-whitening step, the noise covariance matrix of PCA is used to decorrelate and rescale the noise in the data. Second, a rotation based on the first step's outcome is implemented. Specific channel information can be maintained in MNF, since each component's weighting is contributed by all the original bands. Most of the variance can be explained with the first three components, while the remaining components are contributed mainly by noise (Boardman 1993).

Similarly, TC transformation orthogonally transforms the original data into a three-dimensional space (Kauth and Thomas 1976) of brightness, greenness, and wetness (Jensen and Lulla 1987). If the data set is *Landsat-7* Enhanced Thematic Plus with six spectral bands, results also contain three more outputs—the fourth, fifth, and sixth components. The first TC band relates to the overall brightness of the image, while the second output band corresponds to the degree of greenness. The third band indicates the wetness of the land surface. TC transformation was originally designed to maximize separation of the different growth statuses of vegetation.

BN reassigns the range of the pixel values in each band linearly. Contrasting information is well presented in the stretched output. BN has two steps: searching the maximum and minimum values in a band and calculating BN through normalization for each pixel:

$$BN_k = (R_k - R_{k,\min}) / (R_{k,\max} - R_{k,\min}), \quad (3)$$

where  $BN_k$  is the BN value in band  $k$ ,  $R_k$  is original spectral reflectance in band  $k$ , and  $R_{k,\max}$  and  $R_{k,\min}$  are the maximum and minimum values, respectively, of band  $k$ . Light materials will be displayed as lighter colors, while dark regions will appear in darker colors.

DWT can be implemented through a fast wavelet transform (Vetterli and Herley 1992; Strang and Nguyen 1996; Li 2002). The mother wavelet is represented by a set of HP and LP filters in the filter bank. In the beginning, the original image signal goes through the filter bank. The result of the HP filter is the *detail coefficients*, while the result of the LP filter is called

Table 1. Spectral transformations.

Transformation	Linearity	Reference
DA1–3	Linear	Tsai and Philpot 1998
PCA	Linear	Pearson 1901; Byrne <i>et al.</i> 1980; Richards and Richards 1999
ICA	Linear	Bayliss, Gualtieri and Cromp 1998; Chen and Zhang 1999; Hyvärinen and Oja 2000
MNF	Linear	Green, Berman, Switzer and Craig 1988; Boardman and Kruse 1994
TC	Linear	Kauth and Thomas 1976
BN	Linear	
DWT1–5	Linear	Vetterli and Herley 1992; Strang and Nguyen 1996; Li 2002
CR	Nonlinear	Kruse 1988
GHP, GLP, HP, LP	Nonlinear	Green, <i>et al.</i> 1988; Schowengerdt 2006; Yu <i>et al.</i> 2006
NSMA	Nonlinear	Wu 2004
Tie1–7	Nonlinear	Asner and Lobell 2000

BN: band normalization; CR: continuum removal; DA: derivative analysis; DWT: discrete wavelet transform; GHP: Gaussian high-pass; GLP: Gaussian low-pass; HP: high-pass; ICA: independent component analysis; LP: low-pass; MNF: minimum noise fraction; NSMA: normalized spectral mixture analysis; PCA: principal components analysis; TC: tasselled cap; Tie: tie spectral transformation.

the *approximation coefficients*. In the single-step DWT, the original signal goes through the filter once. The image can be well reconstructed by using the approximation coefficients and setting other coefficients to 0 (Li 2002). In this study, only the single-level decomposition was performed with different wavelets—bior1.1 (DWT1), coif1 (DWT2), db1 (DWT3), rbio1.1 (DWT4), and sym2 (DWT5).

### Nonlinear Spectral Transformation

In addition to linear spectral transformation methods, we examined four major nonlinear transformation techniques: CR (Kruse 1988), spatial filtering transformation (LP, HP, GLP, and GHP filters), NSMA (Wu 2004), and tie spectral transformation (Asner and Lobell 2000). These transformation methods are summarized in Table 1, and described in the following.

CR is a method of spectral reflectance normalization (see Kruse 1988). During CR, straight-line segments connect every peak of local spectra to construct a convex hull. The first and last peaks in the local spectra are set to 1 in the continuum removal data, while other data points in the original spectral curve are assigned as less than 1. This can enhance the absorption features from a spectral curve, eliminating slope effects, topography, illumination, and the grain-size effect.

Spatial filtering is another type of spectral transformation. Generally, it involves using a moving window to construct a filter. The center value of the original pixel is replaced by a mathematical computation with the pixel value and corresponding filter value (moving window value). The filter can be defined as HP or LP, which highlights the corresponding

frequency and suppresses the other type of frequency. That is, an HP filter is likely to highlight heterogeneous areas and compress the information of homogenous areas; conversely, an LP filter emphasizes smooth areas instead of rough. In this study, four filters were examined: LP, HP, GLP, and GHP.

NSMA was proposed by Wu (2004). With NSMA, reflectance is divided by the mean value of the corresponding pixel in all bands. Brightness can be eliminated or reduced through NSMA, improving the separability of urban land cover classes.

Finally, tie spectral transformation was introduced by Asner and Lobell (2000). They used the 2080-nm wave band as the tie point, then implemented the tie transformation through applying other bands minus the tie point. Results indicated that tie spectra could reduce the variation caused by soil moisture, leaf and litter area index, tissue optics, and canopy architecture. Only shortwave infrared were examined in that study. Therefore, it is still necessary to explore the potential tie points in visible and near-infrared wave bands in urban and suburban areas. Thus, in this study all bands were viewed as potential tie points and each tie transformation was calculated respectively.

## Experiments

### Study Areas and Data Sources

Three cities in the United States were examined in this study (Figure 1): Janesville, Wis., Asheville, N.C., and Columbus, Ohio. Janesville is on the western shore of Lake Michigan, within the humid continental climate. It has long nights in

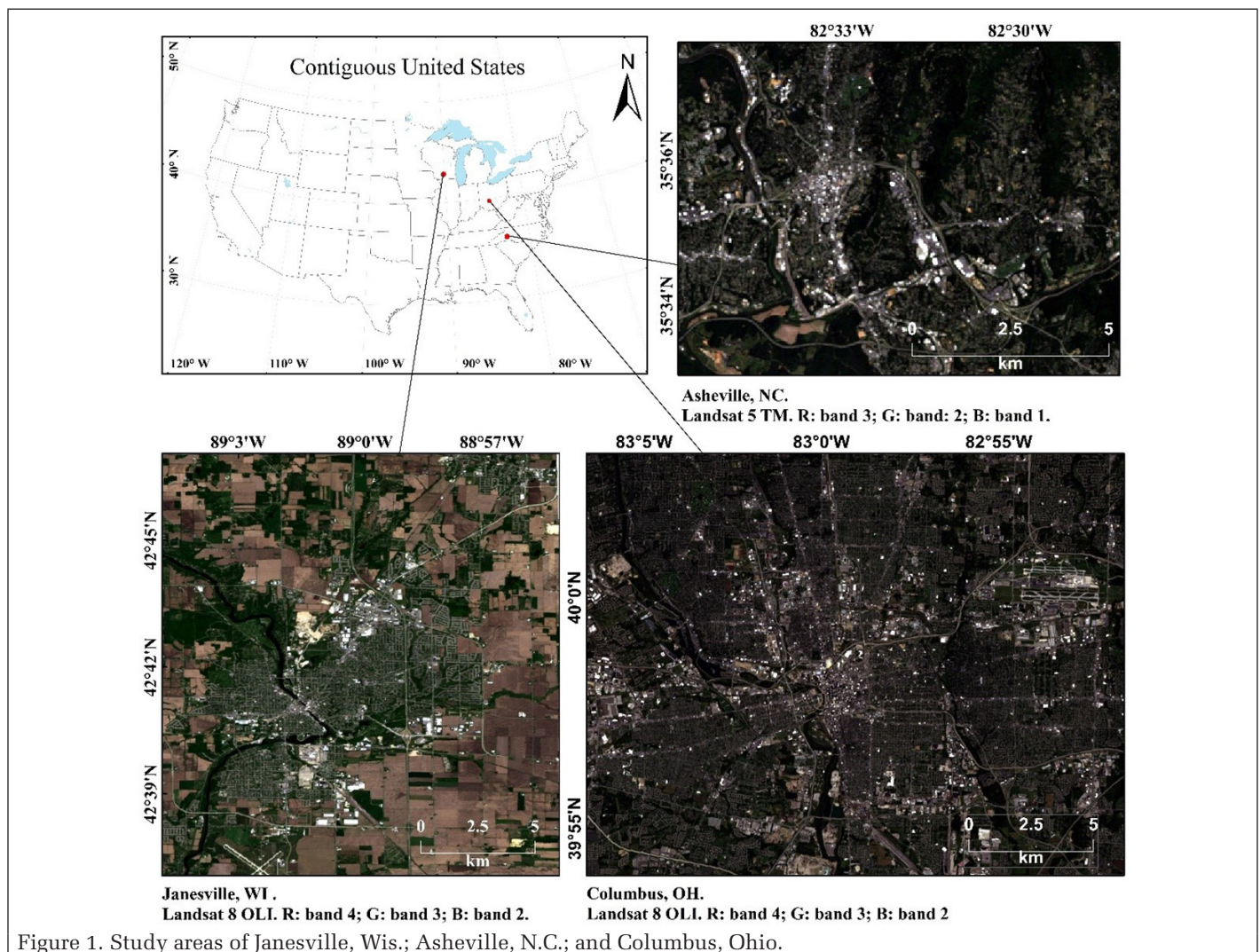


Figure 1. Study areas of Janesville, Wis.; Asheville, N.C.; and Columbus, Ohio.

the winter and cool temperatures in summer. Flat plain is its major landscape in Janesville. Asheville is the largest city in western North Carolina. It is in the Blue Ridge Mountains where two rivers, the Swannanoa and French Broad, merge together. It is in a humid subtropical climate area, which means it is cool in winter and not as hot as in summer as other eastern cities. Mountainous characteristics are significant in the Asheville area, and residential buildings are constructed based on its local terrain. Columbus, the largest city in Ohio, has relatively flat topography. Like Janesville, its climate is humid continental. Winter is cold and dry, while summer is hot and muggy. The three study areas are mainly occupied by commercial buildings, freeways, parking lots, residential houses, soil, and vegetation (tree and grass).

Two scenes of *Landsat-8* Operational Land Imager imagery (Janesville: June 3, 2014; Columbus: September 14, 2015) and a scene of *Landsat-5* Thematic Mapper imagery (Asheville: June 2, 2009) were used in this study. Image preprocessing was applied, such as radiometric calibration, atmospheric correction using Fast Line-of-sight Atmospheric Analysis of Hypercube with corresponding parameters, and reprojection to Universal Transverse Mercator (Janesville: Zone 16; Asheville and Columbus: Zone 17). Historical high spatial resolution images (Columbus: August 22, 2015; Janesville: June 12, 2014; Asheville: May 30, 2009) acquired on Google Earth were utilized to assess the mapping accuracy.

## Method

The main objective of this study was to test whether there is a significant difference after applying a spectral transformation and to figure out which scheme performs better. Thus, we repeatedly applied SMA on each transformed scheme 100 times using different spectra. Such repeated tests can reveal each transformed scheme's reliability. We then used paired-sample *t* tests to examine whether the differences were significant and to figure out which scheme performs better. Generally, the entire process comprises four steps: spectral transformation, sample selection, SMA and accuracy assessment, and paired-sample *t* test. First, each transformation scheme was applied on the original data to create the transformed images. Second, training samples were collected from the transformed images for the construction of a spectral library, and testing samples were selected from the original image and digitized in the corresponding areas of a high-resolution image for accuracy assessment. Third, SMA was applied on each transformed image and the MAE of each test was calculated. Finally, paired-sample *t* tests were applied on the MAE sets of untransformed and transformed schemes to test their differences.

### Spectral Transformation

Spectral transformations were applied to the original data set using the corresponding methods. In particular, DA1–3, PCA, ICA, MNF, TC, CR, GHP, GLP, HP, and LP were calculated directly from ENVI and its extension models. BN was computed using Equation 3 while NSMA was calculated using the method depicted in Wu (2004). DWT1–5 were calculated using MATLAB's *dwt2* function. Tie1–7 (Tie2–7 in Asheville) were created with the method described by Asner and Lobell (2000).

### Sample Selection

Training samples were collected from the transformed images. Four land cover classes were selected as training samples in this study: vegetation (V), high-albedo impervious surface area (ISAh), low-albedo impervious surface area (ISAL), and soil (S). They were collected from the transformed images with the assistance of high spatial resolution images to avoid incorrect pixels. We had 50 training samples of each class for each location, and each training-sample set was used for corresponding spectral-library construction.

Testing samples were collected from the original image to assess each scheme's performance. We selected 64, 60, and 50 testing samples, respectively, for Janesville, Asheville, and Columbus. Each testing sample is  $3 \times 3$  pixels ( $90 \times 90$  m) to avoid the geometric error impact acquired from reprojection and data acquisition. Fractions of impervious surface area within the testing samples were calculated through digitizing the corresponding area in high spatial resolution images.

### SMA and Accuracy Assessment

Fully constrained linear SMA was applied to transformed and untransformed data using the V-ISAH-ISAL-S end-member model. Each transformed scheme was tested 100 times using randomly selected spectra in the corresponding spectral library.

The performance of each transformed scheme was evaluated with MAE, which was calculated based on comparison between estimated and referenced ISA fractions. Estimated fractions of ISA were calculated by the sum of ISAh and ISAL fractions in the same pixel.

### Paired-Sample *t* Test

Paired-sample *t* tests were used to test whether there were significant differences in MAE between transformed and untransformed schemes. Unlike analysis of variance, paired-sample *t* tests compare the differences test by test, which is more reliable for indicating the performance of transformed schemes. Paired-sample *t* tests provide the variables of mean difference and their significant value. Mean difference is calculated by subtracting the MAE of transformed schemes from that of untransformed ones. Positive values mean the MAE of untransformed schemes is larger than that of transformed schemes, while negative values represent the opposite. Significant values indicate the significance of the test result. In addition, the number of improved tests and their improved percentages were counted to demonstrate their performance. The number of improved tests is calculated by counting the number of tests which have a lower MAE than untransformed schemes. The improved percentage is the average MAE of the improved test. In addition, box plots and statistical description were applied to illustrate the general performance of each scheme.

## Results

The detailed performances of transformed and untransformed schemes are illustrated with box plots and descriptive statistical analysis for the three study areas (Figures 2–4). A summary of the MAEs for the three study areas is as follows.

- Janesville area. The MAE of the original data is 0.11, which is less than those of most transformed schemes—except NSMA. NSMA has the lowest MAE, of 0.10. MAE values of PCA, TC, GLP, Tie4, and Tie5 are similar to that of the untransformed scheme (0.11). Transformed schemes of DA1–3, ICA, MNF, BN, Tie1–3, Tie6, Tie7, and DWT have slightly higher MAEs than the untransformed scheme, varying from 0.12 to 0.14. CR, GHP, and HP, have relatively higher MAEs: 0.20, 0.18, and 0.18, respectively.
- Asheville area. The MAE of the untransformed scheme is as same as in Janesville (0.11). DA1–3, MNF, and Tie3–7 have slightly lower MAEs compared to the untransformed scheme, with values around 0.10. GHP and HP have very high MAE values, of 0.21 both. Other schemes' MAEs are slightly higher than that of the untransformed scheme.
- Columbus area. The MAE of the untransformed scheme in Columbus is about 0.14, which is worse than in Janesville or Asheville. GHP and HP illustrate extreme high MAEs in this study area, at 0.25 both. DA1–2, ICA, MNF, CR, GLP, LP, NSMA, Tie3, Tie5, DWT1, and DWT5 have small MAEs, between 0.11 and 0.13. DA3, PCA, TC, Tie1, Tie2, Tie6, Tie7, and DWT2–4 have similar MAEs to the untransformed scheme.

Table 2 reports the results of the paired-sample  $t$  tests, the number of improved tests, and the average improved percentage. It reveals that only NSMA shows improvement, with MAEs lower than the untransformed scheme in all study areas (positive values in three study areas). Paired-sample  $t$  tests also illustrate that the differences between NSMA and the untransformed scheme are significant, as their  $p$  values are less than 0.05. Some schemes, such as DA1, DA2, MNF, GLP, and Tie3–5, have slightly lower MAEs compared to the untransformed scheme in two study areas but larger MAEs in another study area. However, a paired-samples  $t$  test cannot indicate a significant difference, since many of these transformed schemes have  $p$  values higher than 0.05. DA1–3, CR, Tie4, Tie6, and Tie7 have better performance in only one study area, and worse results in the other two. TC, BN, GHP, HP, Tie1, and DWT2–4 have lower accuracy, as the mean differences are negative in all three study areas. Further, significant differences between the untransformed scheme and TC, Tie1, and DWT2–4 cannot be obtained, since their  $p$  values are larger than 0.05.

In addition, we counted the number of improved tests as well as the average improved percentage for each scheme. Generally, transformed schemes (DA2, DA3, NSMA, Tie2, Tie4, Tie6, and Tie7) performed better in Asheville than in the other two study areas, as the number of improved tests is generally larger. NSMA performed better than the untransformed scheme in Janesville, Asheville, and Columbus, as 67%, 69%, and 62% of the tests (respectively) have lower MAEs than the untransformed scheme. The performance of CR is very unstable, with the number of improved tests varying greatly from 11 to 32 to 87 in Janesville, Asheville, and Columbus, respectively. In general, the improved percentages in each scheme are relatively high. Many of the transformed schemes improved about 30%.

## Discussion

Spectral variability, including between-classes and within-class variability, is widely present in remotely sensed imagery. Factors such as materials' spectral characteristics, geometry, and other

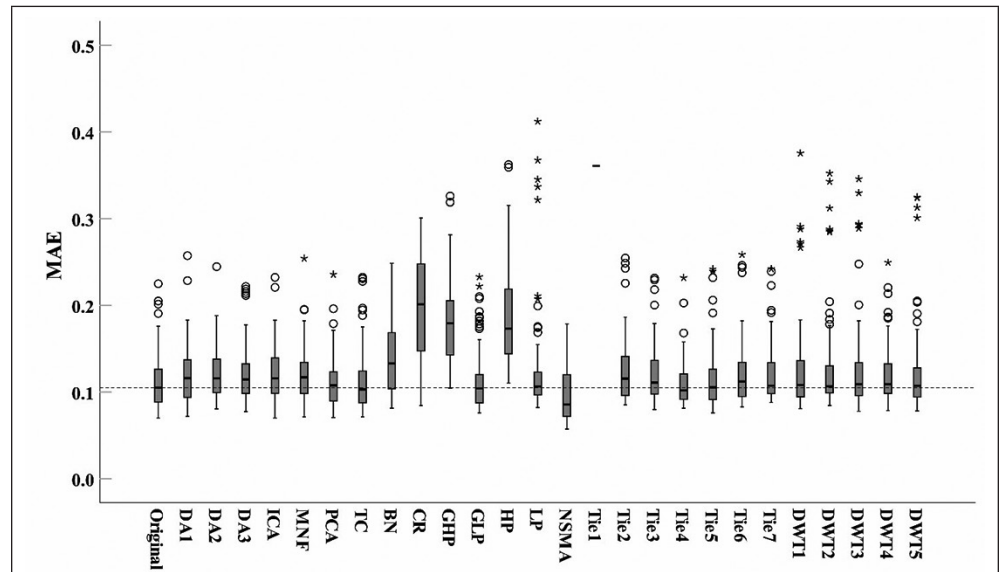


Figure 2. Box plot of mean absolute error in Janesville, Wis., United States.

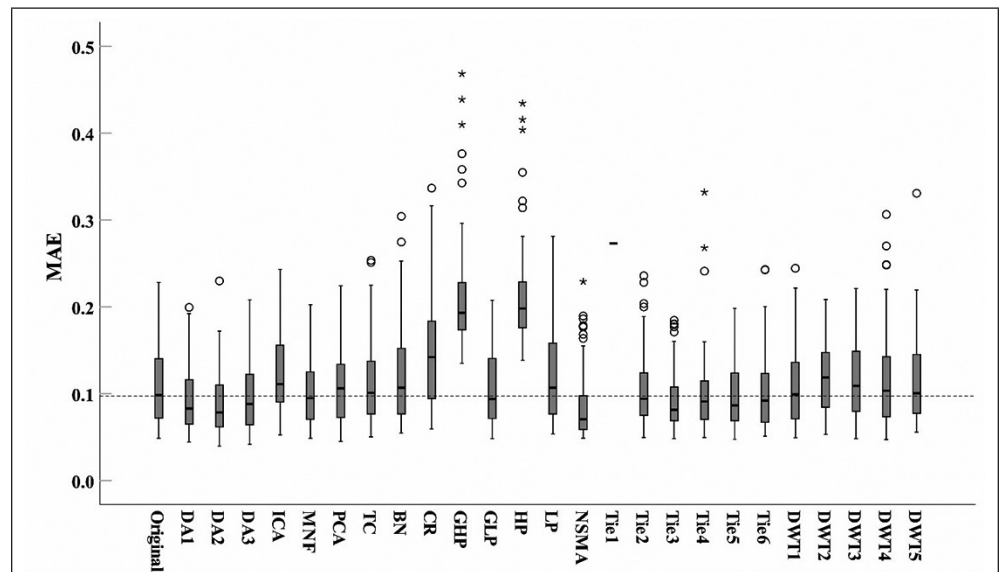


Figure 3. Box plot of mean absolute error in Asheville, N.C., United States.

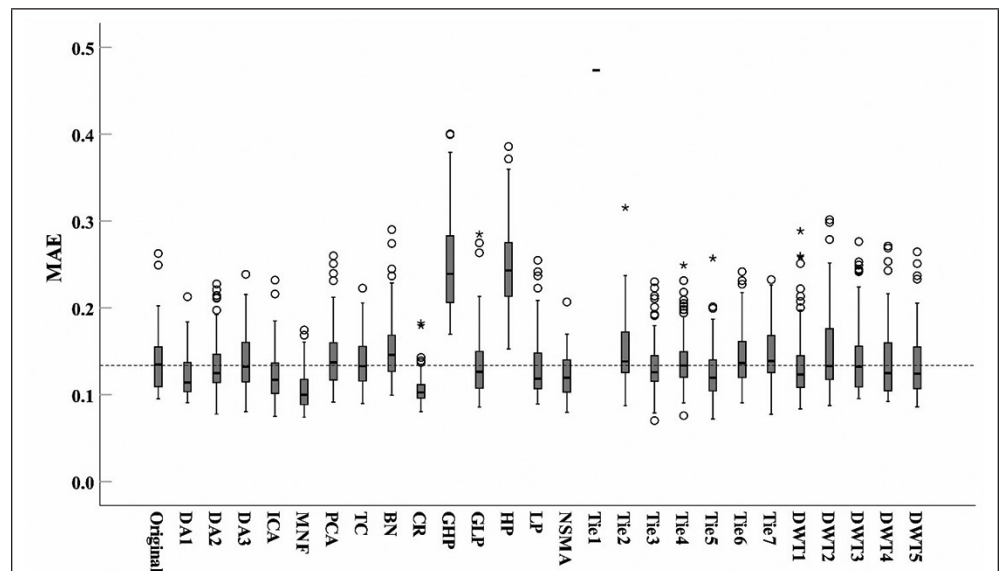


Figure 4. Box plot of mean absolute error in Columbus, Ohio, United States.

Table 2. Results of paired-sample *t* test and improved statistic.

Schemes	Paired-sample <i>t</i> test						Number of improved tests			Average improvement (%)		
	Mean difference			Sig. (two-tailed)								
	Jane.	Ashe.	Col.	Jane.	Ashe.	Col.	Jane.	Ashe.	Col.	Jane.	Ashe.	Col.
DA1	-0.008	<b>0.015</b>	<b>0.012</b>	0.054	<b>0.011</b>	<b>0.003</b>	38	<b>58</b>	<b>66</b>	28.0	47.3	23.8
DA2	-0.008	<b>0.020</b>	<i>0.002</i>	0.043	<b>0.001</b>	0.618	36	<b>67</b>	53	29.3	54.9	27.2
DA3	-0.009	0.012	-0.003	0.059	0.058	0.429	40	59	46	31.0	58.5	23.1
PCA	<i>0.001</i>	-0.001	-0.006	0.894	0.864	0.208	49	47	41	29.2	53.0	32.2
ICA	-0.009	-0.015	<b>0.014</b>	0.031	0.024	<b>0.002</b>	37	37	<b>59</b>	28.0	55.0	29.6
MNF	-0.009	<i>0.007</i>	<b>0.030</b>	0.069	0.219	<b>0.000</b>	45	52	<b>79</b>	28.4	43.2	35.3
TC	-0.001	-0.002	-0.001	0.908	0.763	0.890	52	49	49	28.6	46.5	21.5
BN	-0.028	-0.014	-0.016	0.000	0.050	0.002	25	44	40	26.0	44.6	22.8
CR	-0.087	-0.036	<b>0.030</b>	0.000	0.000	<b>0.000</b>	11	32	<b>87</b>	26.5	43.6	24.1
GHP	-0.069	-0.102	-0.113	0.000	0.000	0.000	11	6	2	21.7	15.6	48.6
GLP	-0.001	<i>0.001</i>	<i>0.002</i>	0.848	0.912	0.753	55	52	55	26.0	21.2	14.5
HP	-0.073	-0.103	-0.112	0.000	0.000	0.000	10	5	1	19.8	11.1	11.7
LP	-0.013	-0.013	<i>0.005</i>	0.061	0.100	0.318	46	46	59	25.6	24.8	13.5
NSMA	<b>0.015</b>	<b>0.022</b>	<b>0.014</b>	<b>0.001</b>	<b>0.000</b>	<b>0.001</b>	<b>67</b>	<b>69</b>	<b>62</b>	32.8	38.9	29.2
Tie1	-0.014		-0.009	0.003		0.081	37		47	23.6		21.6
Tie2	-0.012	<i>0.002</i>	-0.016	0.009	0.774	0.003	35	54	41	27.3	59.3	6.2
Tie3	-0.008	<i>0.005</i>	<i>0.001</i>	0.051	0.381	0.870	37	52	55	25.3	18.5	18.4
Tie4	<i>0.003</i>	<b>0.016</b>	-0.005	0.544	<b>0.002</b>	0.281	49	<b>58</b>	45	30.4	48.5	22.7
Tie5	-0.002	<i>0.011</i>	<i>0.010</i>	0.623	0.063	0.024	46	57	61	33.1	51.8	25.1
Tie6	-0.009	<b>0.012</b>	-0.008	0.054	<b>0.049</b>	0.093	39	<b>54</b>	46	27.6	57.5	24.9
Tie7	-0.009	<i>0.008</i>	-0.010	0.071	0.152	0.023	44	54	38	28.7	51.1	23.2
DWT1	-0.013	0.000	<i>0.002</i>	0.030	0.977	0.682	43	55	56	27.8	46.4	25.2
DWT2	-0.014	-0.010	-0.013	0.024	0.073	0.018	45	43	35	25.9	37.2	30.7
DWT3	-0.014	-0.007	-0.004	0.027	0.272	0.424	43	45	48	29.0	38.5	25.1
DWT4	-0.007	-0.007	-0.004	0.094	0.294	0.527	40	52	50	25.6	37.0	29.1
DWT5	-0.009	-0.008	<i>0.002</i>	0.133	0.232	0.711	43	44	57	30.3	40.0	23.2

Ashe.: Asheville; BN: band normalization; Col.: Columbus; CR: continuum removal; DA: derivative analysis; DWT: discrete wavelet transform; GHP: Gaussian high-pass; GLP: Gaussian low-pass; HP: high-pass; ICA: independent component analysis; Jane.: Janesville; LP: low-pass; MNF: minimum noise fraction; NSMA: normalized spectral mixture analysis; PCA: principal components analysis; Sig.: significance; TC: tasseled cap; Tie: tie spectral transformation.

Tie spectral transformation in Asheville (Landsat 5 Thematic Mapper) began with Tie2 in order to match the Tie2 of Janesville and Columbus (Landsat 8 Operational Land Imager). Italics indicate nonsignificant better performance compared to the untransformed scheme; bold indicates significantly better performance.

environmental elements make major contributions to this phenomenon (Portugal *et al.* 1997; Zhang *et al.* 2006). They cause significant confusion in image classifications. Efforts such as weighted SMA and spectral transformation are made by researchers to minimize within-class variability and maximize between-classes variability in order to acquire more accurate results.

Although many scholars have applied several spectral transformed schemes in their applications, there is not a comprehensive comparison between them. This study compared 26 spectral transformations in three different study areas. We repeated tests 100 times with different end-member spectra to reveal the reliability of each scheme. Janesville, Asheville, and Columbus are far from each other. Residential areas, commercial areas, soil, trees, and grass are the major land cover types in each of these areas. These regions can be viewed as typical urban and suburban environments in the United States. Therefore, it is meaningful to compare these three locations with the same end-member model, to test the reliability of each transformed scheme.

Spectral variability is widely present in remotely sensed imagery. Thus, research with different backgrounds may select different end members from images. Moreover,

end-member selection is a key step for successful SMA. Different end members may give different results. Therefore, evaluating a scheme's performance based on one-time end-member selection may not be appropriate. Thus, the significant-difference test was based on 100 repeated tests, which to a certain degree includes many potential spectra. In this case, the general reliability of each transformed scheme can be illustrated from these 100 repeated tests. Moreover, three study areas were tested in order to further prove each transformed scheme's reliability. Thus, the results of the significant-difference test can be reliable in this study.

#### Is There a Significant Difference After Applying a Transformed Scheme?

Results from paired-sample *t* tests demonstrated that a significant difference of MAE existed in many transformed schemes. On the one hand, some significant differences were positive, meaning that the MAEs were reduced. On the other hand, some significant differences were negative, meaning that the MAEs increased. Only NSMA had consistent positive differences in all three study areas, as the MAEs were reduced significantly. Other transformed schemes, such as DA1-3, ICA, and MNF, illustrated a positive significant difference in one or two study areas but a negative one in the remaining area(s). The rest of

the weighting schemes all had negative differences, since they all worsened the accuracy in all three study areas.

### Which Transformed Scheme Is Better?

Performance evaluation based on MAE indicated that only NSMA could perform better than the untransformed scheme in all three study areas. Other schemes illustrated unstable performance or weakened the accuracy.

DA can get rid of unnecessary signal components and highlight minor absorption features by using spectral smoothing and the feature-reduction method. However, it can also raise the possibility of ignoring essential spectral features (Youngtob *et al.* 2011). Different locations may have different essential spectral features. DA may miss different features in different study areas. Thus, the performance of DA varies from place to place. The results of this study illustrate unstable performance, since DA performed better only in some regions, while it was weaker in others. Additionally, DA1 and DA2 showed worse performances than in the results of Zhang *et al.* (2004). This may be attributed to different data sources, since that study applied hyperspectral data, which are different from the multispectral images we used in this study. Hyperspectral data, with more spectral information compared to multispectral imagery, may be effective for SMA. However, Zhang *et al.* did not provide a comparison with untransformed and transformed data, which makes it difficult to evaluate the improvement of derivative spectral unmixing.

We did not observe satisfactory performance for PCA, MNF, TC, or BN in this study. PCA evaluates the components based on eigenvalues, while MNF uses the signal-to-noise ratio to rank the importance of each component. The limitations of PCA and MNF may be attributed to many subtle material substances in Landsat images not being identified by second-order statistics (Wang and Chang 2006), which may provide confusion between classes. The last three bands of PCA, TC, and MNF contain little variance. This may reduce between-classes variance and increase within-class variance, adding more confusion during the fraction calculation. BN does not seem to be necessary in SMA, because of its poor performance in all three study areas.

ICA showed an opposite result from the study of Wang and Chang (2006): It did not perform better than the second-order statistics-based methods like PCA and MNF. That may be due to the theory of ICA that it conserves only crucial and critical information such as anomalies, end members, and small targets, instead of the variance preserved by PCA and MNF. However, there is not a clear pattern for ICA, PCA, and MNF, as the results indicate that their performance varied from place to place.

DWT performance conflicted with the results of Li (2004). The differences between this study and that one are due to the land cover types, data sources, wavelet types, and end-member model. Li used higher-level wavelet types (e.g., Db3, Sym3), while our study used on only lower-level wavelet transformation (e.g., db1, Sym2). Further, Li's land cover types were agricultural lands that contained soybean, large crabgrass, and soil, which was different from our study areas containing commercial areas, residential areas, vegetation, and so on. Moreover, Li's study used two- and three-end-member models, while we used a four-end-member model. Another limitation of Li's study is that the untransformed scheme was not tested, which limits knowledge of how DWT improved the SMA result. Paired-sample *t* tests in the current study demonstrated that lower-level DWT might not be effective for SMA, as it could not improve the accuracy.

CR's performance varied dramatically. Results for Columbus are similar to the results of Youngtob *et al.* (2011). However, results for Janesville and Asheville demonstrated opposite outcomes. Though CR produced a promising result

in estimating chemical concentrations in leaves by removing irrelevant background reflectance and emphasizing absorption features of interest, it did not show stable performance in this study. This may be due to the difference of spectral characteristics between leaves and impervious surfaces and the complexity of spectral reflectance in urban and residential areas. CR can enlarge band-depth differences, reducing the error in spectroscopic estimation of vegetation quality (Mutanga, Skidmore, Kumar and Ferwerda 2005). However, the variability in impervious surface area, of both high and low albedo, is larger than for vegetation, implying that CR may enlarge within-class variance as well. Some scholars state that CR might introduce more signal-to-noise interference, increasing the within-class variability of the same class (Carvalho and Guimaraes 2001), explaining why CR weakened the SMA results for Janesville and Asheville.

Spatial filters, especially HP and GHP, are not suitable for SMA, as they all reduced accuracy dramatically in all three study areas. GLP and LP still provided limited improvement in some areas; however, statistical tests could not achieve significance. Therefore, spatial filters may serve best as edge detection or image smoothing instead of SMA.

NSMA addressed the confusion between impervious surface areas and soil effectively. Between-classes variance between soil and impervious surface increased after application of NSMA. Moreover, the effect of shade can be removed by brightness normalization. Both aspects improve the accuracy of SMA. NSMA had similar performance in all three study areas, proving its stability in urban and suburban environments.

### Conclusions

This study examined the performance of 26 transformations in the Janesville, Asheville, and Columbus areas. Each scheme was tested 100 times with different spectra using the V-ISAh-ISAL-S end-member model. Differences between untransformed and transformed schemes were analyzed using paired-sample *t* tests. Several conclusions can be drawn. First, NSMA is the most reliable transformed scheme, since it showed consistent improvement in all three study areas. Second, some transformed schemes, such as DA1–3, ICA, and MNF, may need careful consideration, since they showed unstable performance in different study areas. Finally, the remaining transformed schemes cannot contribute to the accuracy improvement, since they worsen SMA results in all three study areas.

### Acknowledgments

The authors would like to thank the anonymous reviewers for their constructive comments. This work was supported in part by the GDAS Project of Science and Technology Development, China (2019GDASYL-0103004, 2016GDASRC-0211, 2018GDASCX-0403), Guangdong Innovative and Entrepreneurial Research Team Program (2016ZT06D336), the Research Growth Initiative of the Graduate School of the University of Wisconsin-Milwaukee, and the Natural Science Foundation of Hunan Province, China (2016WK2017).

### References

- Asner, G. P. and D. B. Lobell . 2000. A biogeophysical approach for automated SWIR unmixing of soils and vegetation. *Remote Sensing of Environment* 74 (1):99–112.
- Bayliss, J. D., J. A. Gualtieri and R. F. Cromp . 1998. Analyzing hyperspectral data with independent component analysis. *Proceedings of SPIE* 3240: 133–144.
- Boardman, J. 1993. Spectral angle mapping: A rapid measure of spectral similarity. AVIRIS.

- Boardman, J. W. and F. A. Kruse . 1994. Automated spectral analysis: A geological example using AVIRIS data, north Grapevine Mountains, Nevada. Pages 407–418 in *Proceedings of the Tenth Thematic Conference on Geologic Remote Sensing: Exploration, Environment, and Engineering*, Vol. 1, held in San Antonio, Texas. Edited by J. Editor. Ann Arbor, Mich.: Environmental Research Institute of Michigan.
- Bruce, L. M., C. H. Koger and J. Li. 2002. Dimensionality reduction of hyperspectral data using discrete wavelet transform feature extraction. *IEEE Transactions on Geoscience and Remote Sensing* 40 (10):2331–2338.
- Byrne, G. F., P. F. Crapper F. and K. K. Mayo K. 1980. Monitoring land-cover change by principal component analysis of multitemporal Landsat data. *Remote Sensing of Environment* 10 (3):175–184.
- Carvalho Jr, O. and R. Guimaraes. 2001. Employment of the multiple endmember spectral mixture analysis (MESMA) method in mineral analysis. Pages 73–80 in *Proceedings of the 10th annual JPL Airborne Earth Science Workshop*, Padadena, CA. JPL publication.
- Chen, C. H. and X. Zhang. 1999. Independent component analysis for remote sensing study. *Proceedings of SPIE* 3871: 150–159.
- Chuvieco, E. and A. Huete, A. 2009. *Fundamentals of Satellite Remote Sensing*. Boca Raton, Fla.: CRC Press.
- Debba, P., E. J. M. Carranza , F. D. van der Meer and A. Stein. 2006. Abundance estimation of spectrally similar minerals by using derivative spectra in simulated annealing. *IEEE Transactions on Geoscience and Remote Sensing* 44 (12):3649–3658.
- Geladi, P., H. Isaksson, L. Lindqvist, S. Wold and K. Esbensen. 1989. Principal component analysis of multivariate images. *Chemometrics and Intelligent Laboratory Systems* 5 (3):209–220.
- Green, A. A., M. Berman, P. Switzer and M. D. Craig . 1988. A transformation for ordering multispectral data in terms of image quality with implications for noise removal. *IEEE Transactions on Geoscience and Remote Sensing* 26 (1):65–74.
- Huguenin, R. L. and J. L. Jones L. 1986. Intelligent information extraction from reflectance spectra: Absorption band positions. *JGR Solid Earth* 91 (B9):9585–9598.
- Hyvarinen, A. 1999. Fast and robust fixed-point algorithms for independent component analysis. *IEEE Transactions on Neural Networks* 10 (3):626–634.
- Hyvärinen, A. and E. Oja. 2000. Independent component analysis: Algorithms and applications. *Neural Networks* 13 (4–5):411–430.
- Jensen, J. R. and K. Lulla. 1987. Introductory digital image processing: A remote sensing perspective. *Geocarto International* 2 (1):65.
- Kauth, R. J. and G. S. Thomas S. 1976. The tasselled cap—A graphic description of the spectral-temporal development of agricultural crops as seen by Landsat. *Proceedings of the LARS Symposia*, pp. 159.
- Kruse, F. A. 1988. Use of airborne imaging spectrometer data to map minerals associated with hydrothermally altered rocks in the northern Grapevine Mountains, Nevada, and California. *Remote Sensing of Environment* 24 (1):31–51.
- Laba, M., F. Tsai, D. Ogurcak, S. Smith and M. E. Richmond . 2005. Field determination of optimal dates for the discrimination of invasive wetland plant species using derivative spectral analysis. *Photogrammetric Engineering and Remote Sensing* 71 (5):603–611.
- Li, J. 2002. *Linear Unmixing of Hyperspectral Signals via Wavelet Feature Extraction*. PhD dissertation, Mississippi State University.
- Li, J. 2004. Wavelet-based feature extraction for improved endmember abundance estimation in linear unmixing of hyperspectral signals. *IEEE Transactions on Geoscience and Remote Sensing* 42 (3):644–649.
- Mutanga, O., A. K. Skidmore K., L. Kumar and J. Ferwerda. 2005. Estimating tropical pasture quality at canopy level using band depth analysis with continuum removal in the visible domain. *International Journal of Remote Sensing* 26 (6):1093–1108.
- Pearson, K. 1901. LIII. On lines and planes of closest fit to systems of points in space. *The London, Edinburgh, and Dublin Philosophical Magazine and Journal of Science* 2 (11):559–572.
- Portigal, F., R. Holasek, G. Mooradian, P. Owensby, M. Dicksion and M. Fene. 1997. Vegetation classification using red edge first derivative and green peak statistical moment indices with the Advanced Airborne Hyperspectral Imaging System (AAHIS). Pages PP–PP in *Proceedings of the Third International Airborne Remote Sensing Conference and Exhibition: Development, Integration, Applications & Operations*, held in Copenhagen, Denmark. Edited by J. Editor. Ann Arbor, Mich.: Environmental Research Institute of Michigan.
- Richards, J. A. and J. Richards. 1999. *Remote Sensing Digital Image Analysis*. Berlin: Springer.
- Schowengerdt, R. A. 2006. *Remote Sensing: Models and Methods for Image Processing*, 3rd ed. Burlington, Mass.: Academic Press.
- Strang, G. and T. Nguyen. 1996. *Wavelets and Filter Banks*. Wellesley, Mass.: Wellesley-Cambridge Press.
- Tsai, F. and W. Philpot. 1998. Derivative analysis of hyperspectral data. *Remote Sensing of Environment* 66 (1):41–51.
- Vetterli, M. and C. Herley. 1992. Wavelets and filter banks: Theory and design. *IEEE Transactions on Signal Processing* 40 (9):2207–2232.
- Wang, J. and C.-I. Chang. 2006. Independent component analysis-based dimensionality reduction with applications in hyperspectral image analysis. *IEEE Transactions on Geoscience and Remote Sensing* 44 (6):1586–1600.
- Wu, C. 2004. Normalized spectral mixture analysis for monitoring urban composition using ETM+ imagery. *Remote Sensing of Environment* 93 (4):480–492.
- Xu, S., Liu, J., Wang, Y., Han, L., & Zhang, Y. 2011. Straight line extraction via multi-scale hough transform based on pre-storage weight matrix. *Acta Geodaetica Et Cartographica Sinica* 32(23): 8315–8330.
- Youngentob, K. N., D. A. Roberts, A. A. Held, P. E. Dennison, X. Jia and D. B. Lindenmayer. 2011. Mapping two Eucalyptus subgenera using multiple endmember spectral mixture analysis and continuum-removed imaging spectrometry data. *Remote Sensing of Environment* 115 (5):1115–1128..
- Yu, Q., P. Gong, N. Clinton, G. Biging, M. Kelly and D. Schirokauer. 2006. Object-based detailed vegetation classification with airborne high spatial resolution remote sensing imagery. *Photogrammetric Engineering and Remote Sensing* 72 (7):799–811.
- Zhang, J., B. Rivard and A. Sanchez-Azofeifa. 2004. Derivative spectral unmixing of hyperspectral data applied to mixtures of lichen and rock. *IEEE Transactions on Geoscience and Remote Sensing* 42 (9):1934–1940.
- Zhang, J., B. Rivard, A. Sánchez-Azofeifa and K. Castro-Esau. 2006. Intra-and inter-class spectral variability of tropical tree species at La Selva, Costa Rica: Implications for species identification using HYDICE imagery. *Remote Sensing of Environment* 105 (2):129–141.

LEARN  
DO  
GIVE  
BELONG

**ASPRS Offers**

- » Cutting-edge conference programs
- » Professional development workshops
- » Accredited professional certifications
- » Scholarships and awards
- » Career advancing mentoring programs
- » *PE&RS*, the scientific journal of ASPRS

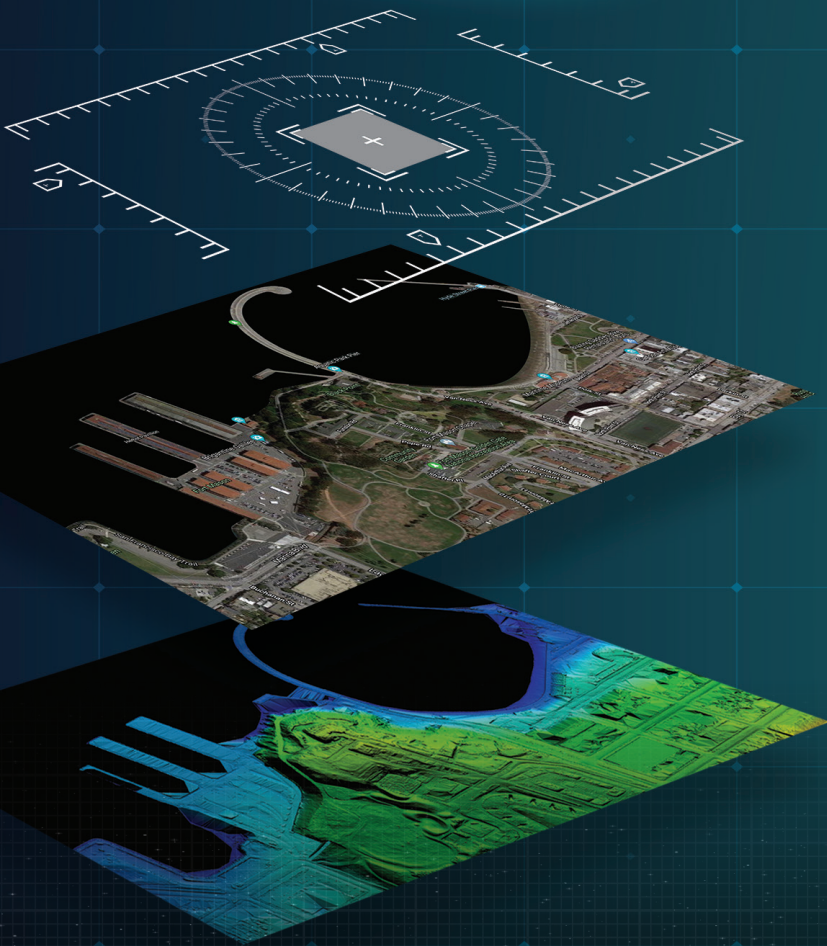
[asprs.org](http://asprs.org)

ASPRS

# AT GEOMNI, WE MAP FOR SUCCESS



When you have Geomni collect imagery and data for your next project you will be harnessing the power of one of the largest Geo-spatial companies in the United States. With 14 hubs nationally, we are local to your next planned job site. Helping you map for success is our mission. We achieve that goal by providing access to our extensive data library, and offering custom imaging flights, while our fleet provides the regional knowledge, resolution, accuracy, and timeliness to deliver the critical information precision mappers need, at a price point fit for your project budgets.



HAWAII

NORCAL

SOCAL

OREGON

IDAHO

HEADQUARTERS

ARIZONA

NEW MEXICO

COLORADO

TEXAS

KANSAS

INDIANA

FLORIDA

SOUTH CAROLINA

MARYLAND

MAINE



[WWW.GEOMNI.COM/PSM](http://WWW.GEOMNI.COM/PSM)